AFRL-PR-WP-TR-2005-2047

EXPERIMENTAL TESTING AND NUMERICAL MODELING OF SPRAY COOLING UNDER TERRESTRIAL GRAVITY CONDITIONS

Kerri M. Baysinger
Kirk L. Yerkes

Electrochemistry and Thermal Sciences Branch (AFRL/PRPS)
Power Division
Propulsion Directorate
Air Force Materiel Command, Air Force Research Laboratory
Wright-Patterson Air Force Base, OH 45433-7251

Scott K. Thomas

Wright State University

JANUARY 2005

Interim Report for 01 October 2003 – 31 December 2004

Approved for public release; distribution is unlimited.

STINFO INTERIM REPORT

PROPULSION DIRECTORATE
AIR FORCE MATERIEL COMMAND
AIR FORCE RESEARCH LABORATORY
WRIGHT-PATTERSON AIR FORCE BASE, OH 45433-7251

NOTICE

This technical report has been reviewed and is approved for publication.

/s/	/s/
KIRK L. YERKES	JOHN G. NAIRUS
Project Engineer	Chief
Electrochemistry & Thermal Sciences Branch	Electrochemistry & Thermal Sciences Branch

/s/
CYNTHIA A. OBRINGER
Deputy Chief
Power Division

REPORT DOCUMENTATION PAGE

Form Approved
OMB No. 0704-0188

1. REPORT DATE ***(DD-MM-YY)*** January 2005	**2. REPORT TYPE** Interim	**3. DATES COVERED *(From - To)*** 10/01/2003 – 12/31/2004

4. TITLE AND SUBTITLE

EXPERIMENTAL TESTING AND NUMERICAL MODELING OF SPRAY COOLING UNDER TERRESTRIAL GRAVITY CONDITIONS

5a. CONTRACT NUMBER
In-house

5b. GRANT NUMBER

5c. PROGRAM ELEMENT NUMBER
62203F

6. AUTHOR(S)

Kerri M. Baysinger and Kirk L. Yerkes (AFRL/PRPS)
Scott K. Thomas (Wright State University)

5d. PROJECT NUMBER
3145

5e. TASK NUMBER
20

5f. WORK UNIT NUMBER
C9

7. PERFORMING ORGANIZATION NAME(S) AND ADDRESS(ES)

Electrochemistry and Thermal Sciences Branch (AFRL/PRPS)
Power Division
Propulsion Directorate
Air Force Materiel Command, Air Force Research Laboratory
Wright-Patterson Air Force Base, OH 45433-7251

Wright State University

8. PERFORMING ORGANIZATION REPORT NUMBER

AFRL-PR-WP-TR-2005-2047

9. SPONSORING/MONITORING AGENCY NAME(S) AND ADDRESS(ES)

Propulsion Directorate
Air Force Research Laboratory
Air Force Materiel Command
Wright-Patterson AFB, OH 45433-7251

10. SPONSORING/MONITORING AGENCY ACRONYM(S)

AFRL/PRPS

11. SPONSORING/MONITORING AGENCY REPORT NUMBER(S)

AFRL-PR-WP-TR-2005-2047

12. DISTRIBUTION/AVAILABILITY STATEMENT

Approved for public release; distribution is unlimited.

13. SUPPLEMENTARY NOTES

14. ABSTRACT

Baseline tests were performed for a spray cooling system using subcooled fluid under terrestrial gravity conditions, and a steady state numerical model of the glass heater pedestal assembly was built using ANSYS finite element software. A parametric study was performed to study the effects of volumetric flow rate, heat transfer rate, and orientation with respect to gravity on the experimental system. The numerical model data was compared with the experimental data in order to determine the spray heat transfer coefficient along the top of the heated surface. For a volumetric flow range $4.0 \le \dot{V} \le 10.0$ gal/hr and a heat load range of $16.0 \le Q \le 50$ W, the estimated spray heat transfer coefficient was on the order of $10,000 \le h_1 \le 15,000$ W/(m2-K), regardless of heater orientation. In addition, the heat lost due to conduction in the upward-facing heater pedestal was estimated using both experimental and numerical results, and was found to be $1.0 \le \Delta Q \le 2.5\%$.

15. SUBJECT TERMS

16. SECURITY CLASSIFICATION OF:			**17. LIMITATION OF ABSTRACT:**	**18. NUMBER OF PAGES**	**19a. NAME OF RESPONSIBLE PERSON** (Monitor)
a. REPORT Unclassified	**b. ABSTRACT** Unclassified	**c. THIS PAGE** Unclassified	SAR	120	Kirk L. Yerkes **19b. TELEPHONE NUMBER** *(Include Area Code)* (937) 255-5721

Standard Form 298 (Rev. 8-98)
Prescribed by ANSI Std. Z39-18

TABLE OF CONTENTS

LIST OF FIGURES

NOMENCLATURE

B	Aspect ratio
c_p	Specific heat, J/(kg-K)
H	Height of the circular cylinder, m
H_p	Height of the glass heater pedestal assembly, m
h_1	Spray heat transfer coefficient at the top of the heater, W/(m^2-K)
h_2	Spray heat transfer coefficient along the side of the pedestal, W/(m^2-K)
h_c	Contact conductance, W/(m^2-K)
J_0, J_1	Bessel functions
k	Thermal conductivity, W/(m-K)
P	Pressure, N/m^2
P, S, R, Z, Γ	Intermediate functions in the circular cylinder problem
Q	Heat rate, W
Q_1	actual heat removed by spray, W
q_0''	Heat flux, W/m^2
q'''	Volumetric heat generation, W/m^3
R	Outer radius of the circular cylinder, m
R_p	Outer radius of the glass heater pedestal assembly
r	Radial coordinate, m
T	Temperature, K
$\bar{T}$	Average temperature, K
$T_{\mathrm{f},1}$	Local freestream temperature of liquid flowing over heater surface, K
$T_{\mathrm{f},2}$	Local freestream temperature of liquid flowing along pedestal wall, K
t	Time, s
$\dot{V}$	Volumetric flow rate, m^3/s
z	Axial coordinate, m
α	Thermal diffusivity, m^2/s
ΔQ	Percent of heat lost due to conduction in glass heater pedestal assembly
Δr	Element width, m
Δt	Timestep size, s
$\beta, \eta, \lambda, \tau$	Eigenvalues
ρ	Density, kg/m^3
θ	Azimuthal coordinate, radians

Subscripts

1	Region 1 of glass heater pedestal assembly (ITO heater)
2	Region 2 of glass heater pedestal assembly (substrate)

3	Region 3 of glass heater pedestal assembly (thin layer 1)
4	Region 4 of glass heater pedestal assembly (thin layer 2)
5	Region 5 of glass heater pedestal assembly (base)
bg	Borosilicate glass
cg	Corning glass
h	Properties at the heater
ITO	Indium/tin oxide heater
lf	Lower film
noz	Nozzle
s	Heater surface
sat	Saturation
uf	Upper film
w	Properties at the outer wall of the glass heater pedestal assembly
0, i	Initial
m, n, u	Index integers
*	dimensionless parameters

I. Introduction

As technology advances, thermal management challenges continue to increase in every area, from multi-million dollar war fighters to home computer systems. New technology is both more powerful and more compact. The by-product of higher power in a smaller package is that an immense amount of heat over a small area, also known as heat flux, must be dissipated to keep systems running safely. Mudawar (2000) identifies two heat flux ranges relative to the amount of heat dissipation. The high-flux range includes heat fluxes on the order of 10^2-10^3 W/cm^2 and the ultra-high-flux range includes requirements of 10^3-10^5 W/cm^2. Depending on the fluid and cooling method, heat transfer coefficients for removing this heat may range from 0.001 to 100 W/(cm^2-K). Single-phase, forced convection improves on natural convection by forcing a fluid over the heated surface, thus producing higher heat transfer coefficients. Boiling (i.e., phase change cooling) takes advantage of phase change of the liquid, using the latent heat of vaporization to further improve on the attainable heat transfer coefficients and increase the critical heat fluxes (CHF's) in cooling systems. Compounding the challenge is the issue of varying gravity, which is found in many aircraft and space-based applications. Every cooling scheme is affected in some way by gravity, or a lack thereof, and finding ways to deal with changes in gravity is vitally important to building effective thermal management systems for such platforms.

Predominant cooling fluids include air, water, and fluorochemical liquids. Air is the cheapest and most readily available cooling fluid, but has relatively poor thermal transport properties, so its use is limited to lower heat flux requirements. Water remains the most effective cooling fluid because of its superior thermal transport properties. However, electrical conductivity precludes its use in direct contact with electrical components and systems. Consequently, dielectric fluorochemical liquids, such as those produced by 3M, are necessary for use with current-carrying components, despite the fact that their thermal properties are inferior to those of water (Mudawar, 2000).

Phase change cooling can exist in several forms, or cooling schemes. Pool boiling may be used in thermosyphons, which passively cool by relying on buoyancy forces to circulate coolant. The device to be cooled is submerged in a dielectric coolant, which boils as the device dissipates heat, releasing vapor bubbles which are driven by buoyancy forces to the upper portion of the container. Here the vapor condenses and falls back into the coolant pool. Thermosyphon performance can be enhanced by several techniques, including surface enhancement, subcooling the fluid, and increasing coolant pressure. While thermosyphons are only one possibility, pool boiling in general relies on buoyancy to carry vapor bubbles from the heater surface. Thus, orientation has a significant effect on performance for any pool boiling system. In addition, gravity affects performance as well. One example of this is a thermosyphon relying on gravity to drain the condensate back to the fluid pool. Much research has been conducted in pool boiling (Kim et al., 2002; Kim, 2003; Straub, 2001), including the effects of microgravity. It has been observed that CHF is generally reduced in microgravity (Kim, 2003), due in part to the variations in bubble dynamics resulting from the lack of buoyancy forces (Straub, 2001).

Heat pipes, like thermosyphons, are passive cooling devices. A detailed description of heat pipes is given by Faghri (1995). A heat pipe consists of three primary sections: evaporator, condenser, and transport (adiabatic) section. The coolant begins in the evaporator, where it is exposed to the heat source via the pipe wall/wick structure, and evaporates, building pressure within the vapor. A pressure gradient drives the vapor through the transport section to the condenser. The condensation of the vapor releases the latent heat of vaporization to the ultimate heat sink. Capillary pressure then pumps the condensate through the wick structure back to the evaporator, where the cycle begins again. Heat pipes exist in many forms and have a wide range of applications. Micro heat pipes may be as small as 25 mm in length, whereas macro heat pipes may be as long as 100 m. Some may not contain an adiabatic section, but all have an evaporator and condenser. Much research has been performed on heat pipes with respect to the effects of acceleration. Kaya (2003) used a centrifuge table to produce elevated gravity conditions, and determined that the accelerating forces at high spin rates can cause a drying out of the wick, since the acceleration overcomes the pumping capacity of the wick. Gu et al. (2004) studied aluminum pulsating heat pipes (PHP) in microgravity. They determined that PHP's are capable of operating successfully in microgravity, and may be suitable for space-based applications using lower-power requirements.

Active cooling systems can alleviate some of the issues found in passive systems and improve on heat transfer characteristics. They are more suitable for high- and ultra-high-flux applications. Flow boiling sweeps bubbles off of heated surfaces, producing higher heat transfer rates and higher CHF levels (Kim, 2003). As in pool boiling, subcooling the liquid helps to increase CHF, but flow boiling has the added ability to vary flow velocity. Increasing flow velocity also helps to raise CHF, in addition to reducing the significant effects of flow orientation (Mudawar, 2000). It is not fully known how low gravity affects flow boiling, as power requirements and large transients have prevented much research in this area thus far.

Jet impingement cooling involves directing coolant from a circular or rectangular orifice onto a heated surface. Because of the impact momentum involved, it is considered an aggressive cooling scheme, and is not feasible in cases involving delicate devices or components. There are three primary formats for jet impingement: free jet impingement, where the liquid is introduced into a gaseous ambient, submerged jet impingement, where the jet is issued into liquid surroundings, and confined jet impingement, where the jet is confined exclusively between the orifice and heated surface. Subcooling, jet diameter, and jet velocity may all increase CHF in jet impingement, but jet velocity has a much larger effect than jet width (Mudawar, 2000). In studying jet impingement in zero gravity, Labus (1977) defined three flow regimes within inviscid flow for this cooling method: surface tension flow, transition flow, and inertial flow, where each regime was correlated to Weber number and the ratio of jet radius to disk radius.

Spray cooling has been used for many applications similar to those using jet impingement cooling, such as metal quenching. One major disadvantage of jet impingement cooling is the creation of large temperature gradients within the device due to the concentrated heat removal in the vicinity of the jet. Spray cooling breaks the coolant down into droplets, which individually impinge on the surface and provide a more uniform heat removal. Sprays may be atomized, where air (or some inert gas) is introduced to assist in the breakdown into droplets. Atomized sprays are not always practical, however, due to the difficulty of removing air from the dielectric cooling liquid. Pressure sprays simply supply high pressure liquid through an orifice, and do not use air to assist in the droplet formation (Mudawar, 2000).

Comparatively little research has been done in the area of spray cooling in microgravity. Choi and Yao (1987) studied heat transfer mechanisms of horizontally impacting sprays. They observed that, as the liquid mass flux increased, so did the heat transfer capability. Kato et al. (1994) used water and CFC-113 as test fluids in spray cooling systems and found that microgravity produced a reduction in CHF for CFC-113, but an increase in CHF for water. Yoshida et al. (2001) studied both copper block and thin-film ITO heaters on a microgravity platform, and found that gravity dependency varied with spray volume flux and the Weber number of fluid droplets for both water and FC-72.

This thesis is part of an ongoing joint effort between the Air Force Research Laboratory (AFRL) and the National Aeronautics and Space Administration (NASA) to study spray cooling for applications in both reduced- and elevated-gravity conditions. Previous research (Kato, 1994; Yoshida, 2001) indicates spray cooling is useful to effectively deal with waste heat generated in space-based platforms, such as the International Space Station or shuttle orbiter, as well as the military war fighter, where in-flight maneuvers can produce both high- and reduced-gravity conditions for transient periods.

The long-range goals of the experiment include macrothermophysics, microthermophysics, and fluid management. Macro-scale studies include the effect of microgravity on the critical heat flux (CHF) and on heat transfer, in particular the convective heat transfer coefficient due to the spray. Micro-scale studies include film dynamics, such as the effects of both reduced- and elevated-gravity conditions on the liquid film formation, surface nucleation and vapor bubble formation, and droplet rebound effects (or lack thereof). Where Kato (1994) and Yoshida (2001) studied the effects of microgravity on a single-nozzle system, and Lin and Ponnappan (2003) built a closed-loop, continuous-flow system for use in terrestrial gravity, the present experiment aims to combine these efforts, studying a continuous-flow, closed-loop spray cooling system in micro- and elevated-gravity conditions. In addition, it is desired in the long-term to integrate a multi-nozzle array into the system.

The objective of this thesis is to present experimental and numerical data acquired for a spray cooling system using subcooled liquid in a terrestrial gravity environment, building on the initial design and testing of the system, as discussed in Baysinger et al. (2004). Baseline tests were done in preparation for experiments to be conducted aboard the NASA KC-135 reduced gravity aircraft. A steady state numerical model was built and tested using ANSYS finite element software, and a parametric study was performed to determine effects of volumetric flow rate, heat transfer rate, and orientation with respect to gravity on the heat transfer within the spray cooling system. The numerical model was compared to the experimental data, and was used to determine the heat transfer coefficient due to the spray and to predict the heat transfer due to conduction within the glass heater pedestal assembly.

II. Experimental Design and Testing

The objective of the experiment was to determine the heat transfer coefficient due to spray cooling on the top surface of a glass heater pedestal assembly. An ITO heater layer was spray deposited onto the top surface of the glass, which was used to provide ohmic heating. Thermocouples were embedded into several layers of the glass to provide temperatures within the pedestal. These temperatures were then used in conjunction with the numerical model, described in the Numerical Modeling section of this thesis, to determine the heat transfer coefficient of the spray. While this thesis focuses on the baseline results of the experiment in Earth's gravitational field, eventually the experiment will be repeated aboard the NASA KC-135 reduced gravity aircraft. Microgravity, lunar gravity, Martian gravity and high-gravity (approximately 1.8 g) conditions will be produced by following a parabolic flight trajectory. Each flight will consist of about 40 parabolas, split into sequences of 10 parabolas, with a turn after each set of 10. The experimental series will be comprised of four flights, for a total of approximately 160 parabolas. Figure 1 shows a typical flight profile with turns before and after a series of parabolas. This figure also shows the variation in ambient cabin temperature which is consistent with the variation in aircraft altitude during maneuvering.

The experimental apparatus consisted of two primary components (Baysinger et al., 2003). The first component was a spray test chamber containing two glass heater pedestals, two spray nozzles, a primary condenser surface, and two sump configurations to collect the liquid and condensate. The second component was the flow loop system consisting of two flow loops: 1) an FC-72 loop to manage the working fluid and 2) a water loop to cool the spray test chamber. A photograph of the overall experimental apparatus is shown in Figure 2.

Figure 3 shows the spray test chamber, which was a cylinder having interior dimensions 20.2 cm (7.97 in) in diameter and 15.2 cm (6 in) in length. It was made of standard vacuum components to provide a leak-tight environment for the spray-cooling experiment. Key components included opposing nozzles to allow for simultaneous testing of different heater orientations with respect to gravity, a cooling shell surrounding the test chamber, and a wick structure surrounding the test area to collect and direct excess fluid and condensate.

Each glass heater pedestal assembly was cylindrical with a diameter of 0.016 m, and consisted of five layers, as shown in Figure 4 and Figure 5. The first layer was a thin-film, transparent, indium-tin oxide (ITO) heater, which was sputter-deposited onto the 0.5-mm-thick fused silica substrate (Corning AMLCD 1737 glass). This combination was chosen to match the coefficient of thermal expansion as closely as possible between the ITO layer and the glass layer to prevent delamination. The heater/substrate was mounted onto a 1-mm-thick wafer of ZN-7 Borosilicate glass using optical cement (Summers SK-9). This subassembly was then adhered to an identical 1-mm-thick wafer of Borosilicate glass, which was finally cemented to the main glass pedestal, which was also made of the ZN-7 glass. The purpose of the two intermediate layers was to allow for grooves to place thermocouples, as shown in Figure 6. The heater pedestal assembly, as fabricated, also allowed for an optical path for visual observation of the heater surface. A preliminary analysis was used to predict temperatures throughout the pedestal in order to determine the best placement for the thermocouples.

Various nozzles were evaluated using a two-axis phase Doppler anemometer (Dantec) to determine spray uniformity and droplet size distribution. Typical droplet velocity, volumetric flux, and mean droplet diameter distributions for the selected nozzles are shown in Figure 7, Figure 8, and Figure 9, respectively. The distance from the nozzle to the heater surface was set to approximately 1 cm. This distance was based on a spray cone angle of 60° such that the spray contacted only the heater surface with minimal overspray. The motion of any excess fluid, which would ordinarily drain to the bottom of the chamber/pedestal in terrestrial conditions, is unpredictable in microgravity, possibly floating in the chamber or adhering to structures due to surface tension. Regardless, the test fluid needed to be effectively removed from the chamber for recirculation. This was accomplished by placing a sump configuration at each nozzle. The sumps served to remove excess fluid from the chamber and spray surface through an annulus between the heater pedestal and sump wall. Figure 10 shows the sump and the heater pedestal together.

Vapor generated at the heater surface was exhausted out past the nozzle into the test chamber interior or entrained with the excess liquid and carried through the sump annulus. Excess vapor and liquid in the chamber were controlled by an annular wick structure, both to aid in condensation and to contain the condensate. The wick structure was formed by lining the internal chamber wall with one layer each of 100 and 150 stainless steel mesh, with the 150 mesh being nearest the wall. An additional cylindrical screen was placed in the chamber interior to provide for an annular space between the screen and the chamber wall. This annular space between the chamber wall and inner screen was filled with stainless steel wool to help confine the unconstrained liquid during microgravity.

The test chamber was affixed to a hinge enabling it to be rotated so that the nozzles could be oriented in either a vertical or horizontal position. This allowed greater flexibility in planning and executing experiments. For the experiments described in this thesis, the chamber was positioned such that the nozzles remained in the vertical orientation. A pressure transducer was installed to measure the vapor pressure inside the chamber. A tri-axis accelerometer (Columbia SA307HPTX) with an uncertainty of ±0.03-g was mounted onto the test chamber to record the transient variation in acceleration throughout the flight profile.

Figure 11 shows a schematic diagram of the fluid loops. Each loop contains a combination of pumps, flow meters, pressure transducers, valves, pressure switches, reservoirs, liquid-air heat exchangers, and interconnecting plumbing to monitor and direct the fluid flow. Temperatures throughout the fluid loops were monitored using Type E thermocouples which were 0.159 cm (0.0625 in) in diameter. Key thermocouple locations include the entrances and exits of the test chamber, reservoirs, and heat exchanger assemblies.

A positive displacement scavenging pump (Tuthill) was used to pump subcooled FC-72 fluid from the sumps through a series of three air/liquid heat exchangers to a reservoir. Pressure transducers were placed on either side of the pump, and the fluid passed through a 40 μm filter (Swagelock) before reaching the reservoir. The reservoir contained either stainless steel wool or a vane structure to reduce fluid sloshing during the flight profile and served as both a volume for the scavenging pump to dump excess working fluid and a pickup reservoir for the nozzle pumps. Following the reservoir, the fluid branched off into two identical flow paths, one for each spray nozzle. Each branch consisted of a positive displacement pump followed by a 15 μm filter (Swagelock), a flow meter (Omega), a pressure transducer, and a pressure switch (United Electric). Electrically-actuated ball valves (Hoke) were placed at the entrance and exit of each branch, to permit isolation of the test chamber. All testing was done with subcooled fluid at ambient temperature; however, a length of copper tubing was placed in each branch for future installation of a reheater that would allow for testing of the spray at varying degrees of subcooling and saturated conditions.

The single-phase water loop maintained the temperature of the exterior wall of the test chamber at a constant value. The design and components were similar to those in the FC-72 loop. A positive-displacement pump moved the water from an assembly of two liquid/air heat exchangers to a reservoir via a 140 μm filter, pressure relief switch, flow meter, and pressure transducer. As with the FC-72 loop, the reservoir contained stainless steel wool to reduce fluid sloshing.

The experiment framework was constructed from "2020" and "1010" sizes of aluminum extrusions and hardware (80/20, Inc.). Shelves were constructed of 0.635 cm (0.25 in) thick aluminum and installed for the purpose of mounting equipment. The entire frame rested on a 1.27 cm (0.5 in) thick aluminum plate, which served both as a mounting plate and a spill containment pan.

Detailed structural analyses and testing were conducted to satisfy NASA safety requirements. Structural integrity under various acceleration field strengths was evaluated for flight on the KC-135 aircraft. NASA guidelines required that all framework and equipment be able to withstand a 9-g load in the forward direction, 3-g in the aft, 6-g down, 2-g lateral, and 2-g up. In addition, a factor of safety of two was required, so all structural analysis and testing were performed at twice the given requirements. Much of the smaller equipment installed on the experiment was pull-tested using a load cell, but larger items and the frame itself were analyzed using static equilibrium equations.

The experiment was operated and monitored via a control panel and data acquisition system. The data acquisition system consisted of a laptop computer mounted to the top of the experimental package, coupled with a data acquisition/switch unit (HP 34970A). A diagram of the instrumentation system is shown in Figure 12, and a photograph of the control panel is shown in Figure 13.

Temperature measurements were obtained throughout the chamber, glass heater pedestal, and within the sump annulus using sheathed thermocouples. Type E thermocouples (0.16 cm diameter, time constant < 4.0 s) were placed in the chamber to measure chamber wall and vapor temperatures, and Type E thermocouples (0.0254 cm diameter, time constant < 0.5 s), were mounted within the glass heater pedestal assembly. For additional stability and accuracy in temperature measurement, the thermocouples within the chamber and glass heater pedestal assembly were referenced to a zero point reference junction (Hart 9101) with a stability of ±0.005ºC.

Temperatures, as measured by thermocouples, within the glass heater pedestal assembly were used to determine the heat transfer coefficient due to the liquid spraying onto the top of the pedestals. In addition, the ambient temperature was monitored using a Type E thermocouple and a thermistor (YSI 44006) mounted on the frame of the experiment. Thermocouples mounted within the chamber and glass heater pedestals were calibrated using an RTD temperature probe (Hart Scientific Model 5628) and temperature bath (Hart Scientific Model 7320) in the temperature range from 35° to 120°C. Resulting thermocouple calibrations yielded an uncertainty of ±0.02°C. A typical thermocouple calibration curve is shown in Figure 14. Two additional Type E thermocouples were placed at the edge of the heater, to measure the liquid temperature exiting off of the heater surface, and in the sump annulus, approximately 1.27 cm below the heater surface.

Heater power was monitored using voltage measurements with an uncertainty of ±0.05% across the heater and a precision resistor with a resistance of 0.10 Ω ± 0.02%, resulting in a heater power measurement error ±0.07%. Visual documentation was acquired through the use of two video cameras (Sony DCR-TRV33) mounted to the experimental frame. One camera recorded a full view of the test chamber, observing the behavior of the fluid therein. The second camera was positioned to record a field of view of only the nozzle being tested. When testing switched from one nozzle to the other, the camera position was adjusted to record the appropriate nozzle.

At the beginning of each experiment, the data acquisition program was initiated via a laptop computer, and all cameras, timers, etc., were synchronized and started. The data acquisition system monitored and recorded the flow rate, acceleration, input heat, and temperatures for the duration of the experiment. Temperatures were measured within the glass heater pedestal, at the inlet of the nozzle, and in the liquid film exiting the heater surface. During the experiments, the volumetric flow rate and heater power were varied for values of $\dot{V}$ = 4, 5, 6, 8, and 10 gal/hr and $\dot{Q}$ = 20, 30, and 50 W, respectively. Experiments were conducted for a fixed flow rate while varying the heater power. When the heater interface temperature reached T_1 = 100ºC, the flow rate was adjusted and the heater power varied for the new flow rate setting.

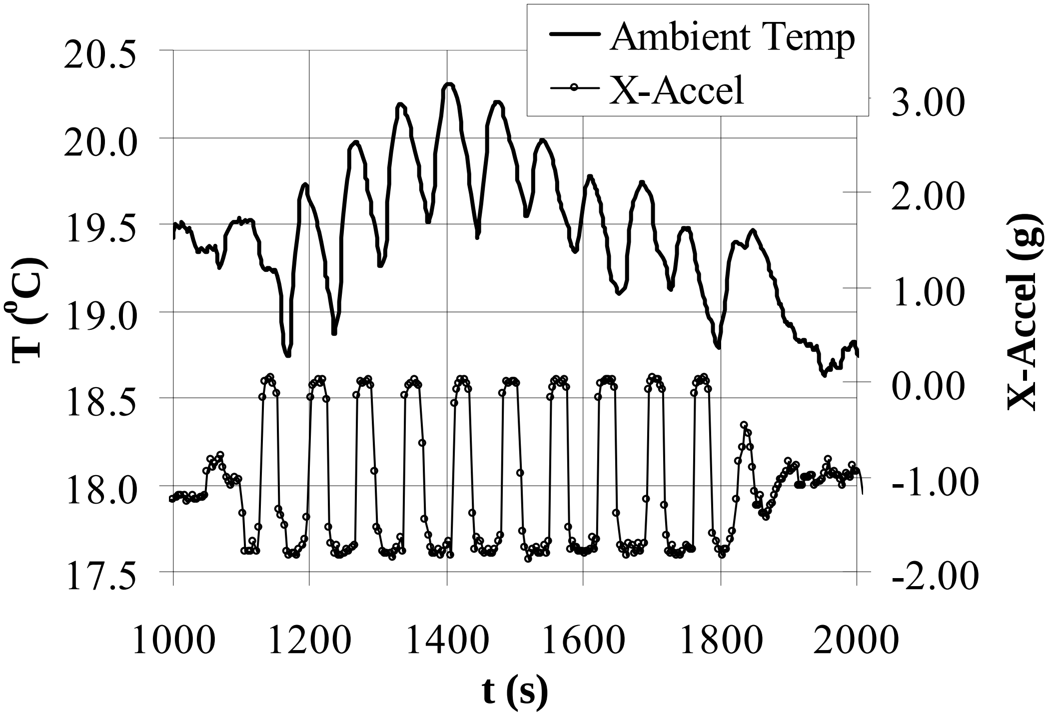

Figure 1: Typical flight profile with ambient temperature and acceleration versus time.

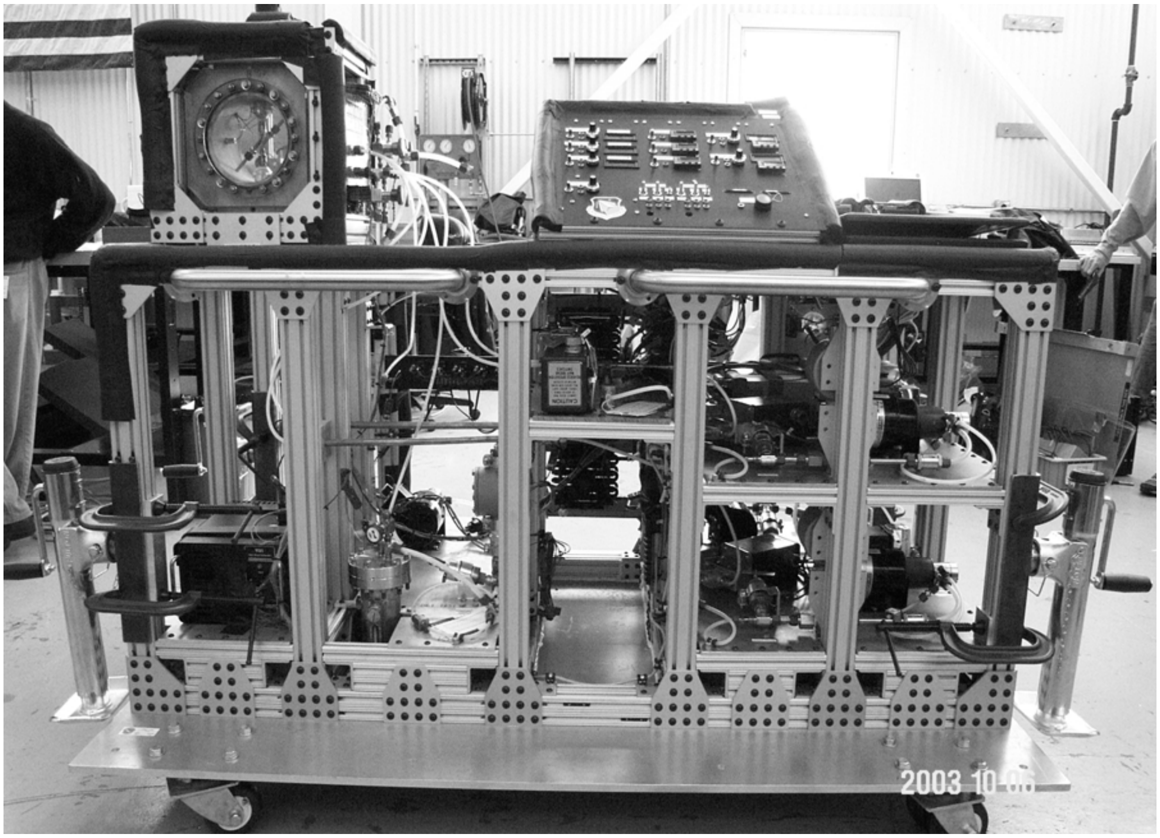

2003 10 06

Figure 2: Photograph of the experimental apparatus.

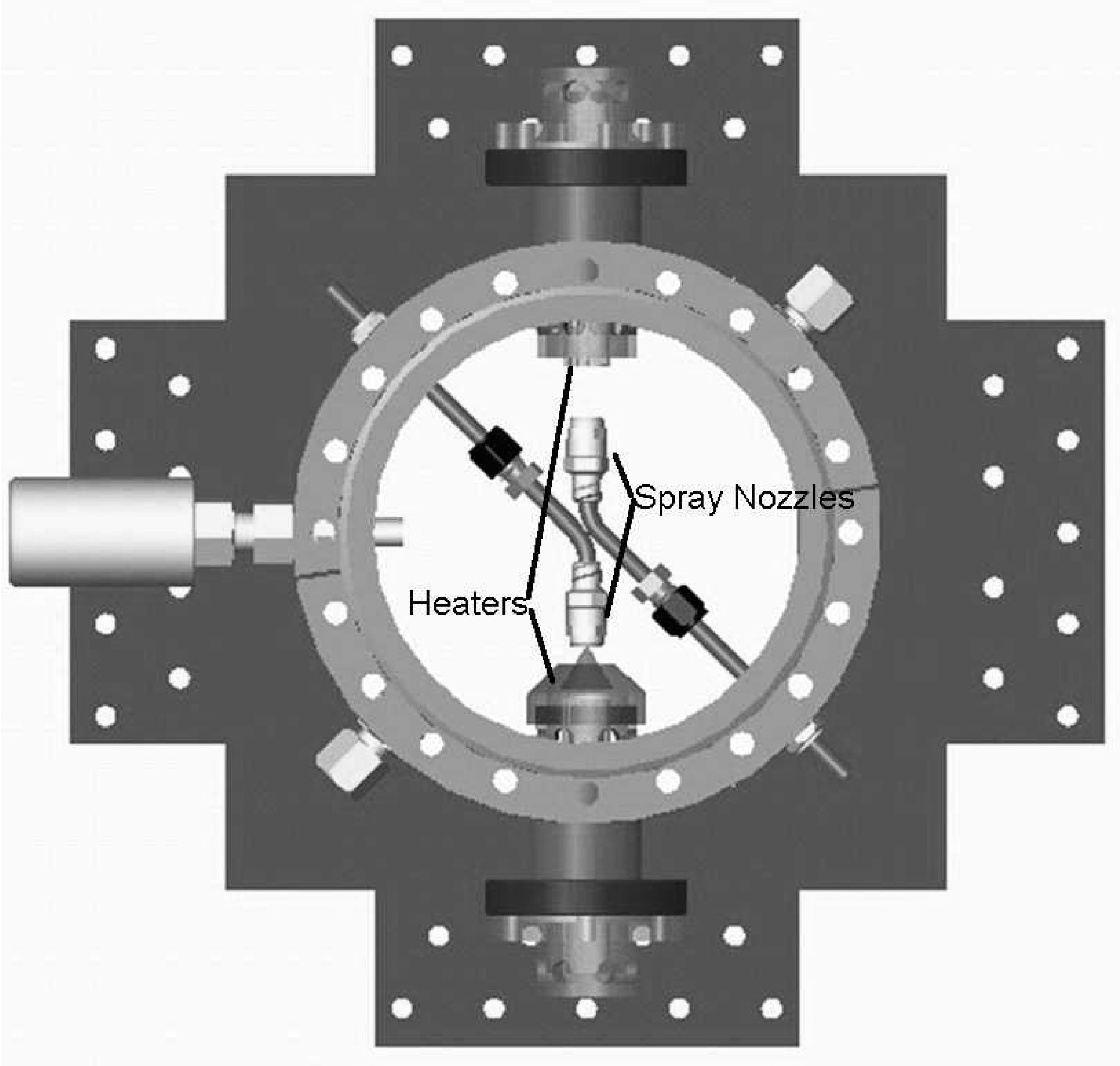

Figure 3: Solidworks model of the spray test chamber.

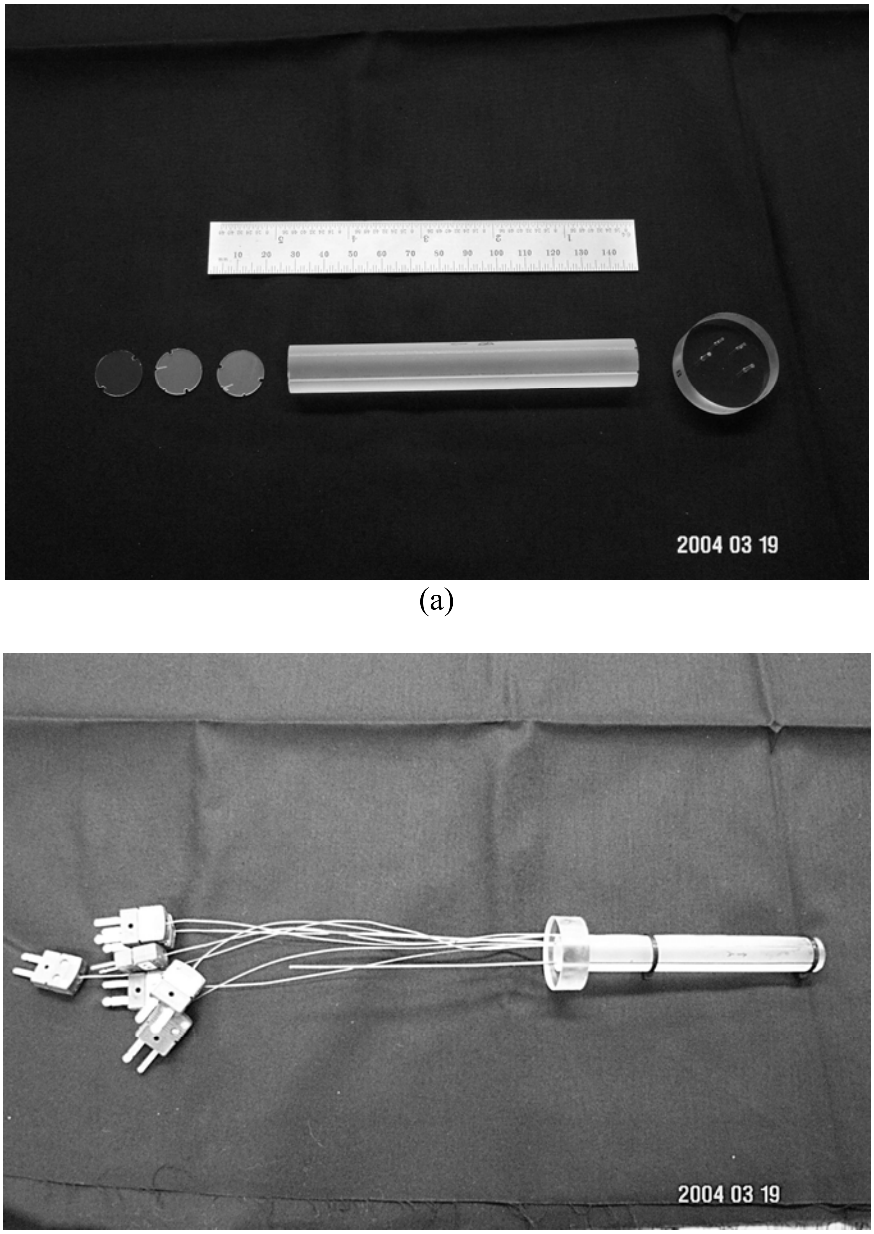

(a)

(b)

Figure 4: Details of the glass heater pedestal assembly: (a) Glass parts used in assembling the heater pedestal; (b) Assembled heater pedestal with embedded thermocouples and copper wires for ohmic heating.

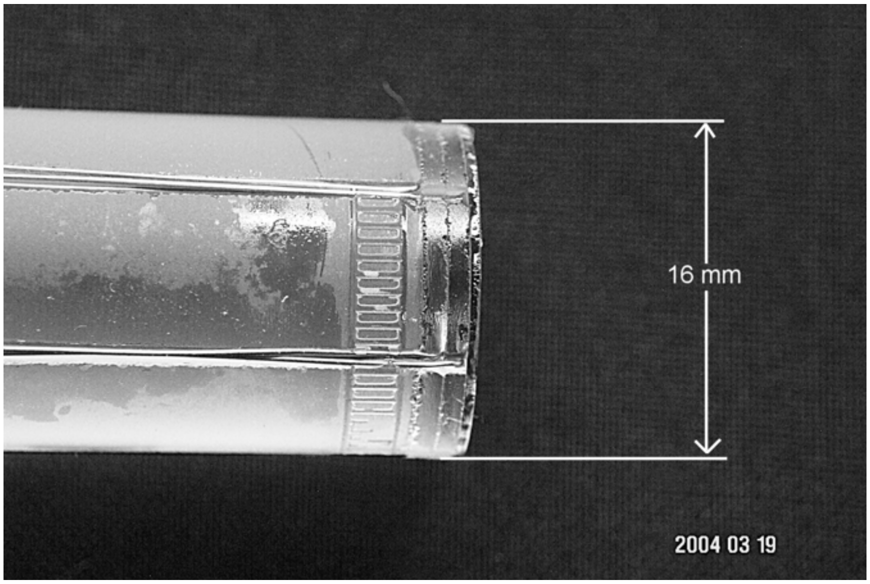

(a)

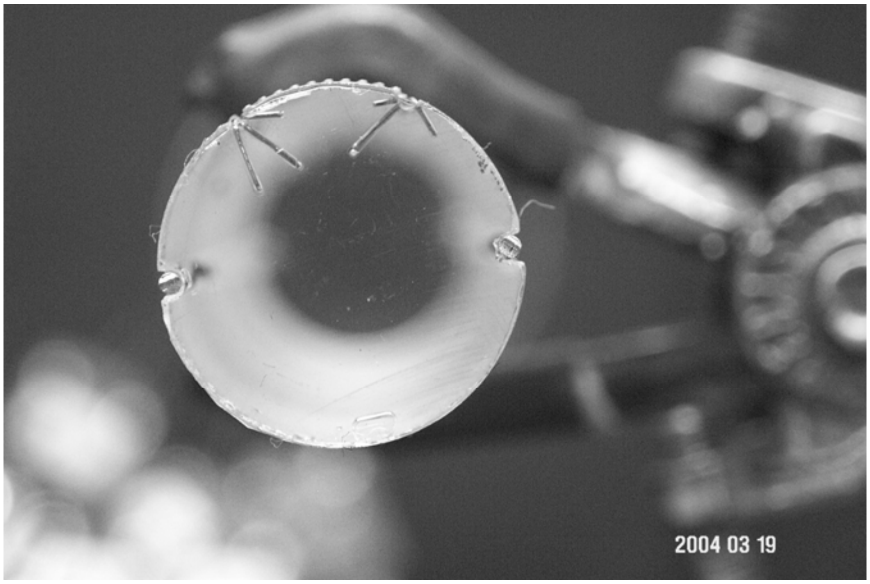

(b)

Figure 5: Details of the glass heater pedestal assembly, continued: (a) Side view of the top of the assembled heater pedestal; (b) Top view of the assembled heater pedestal prior to application of the electrically conductive silver epoxy.

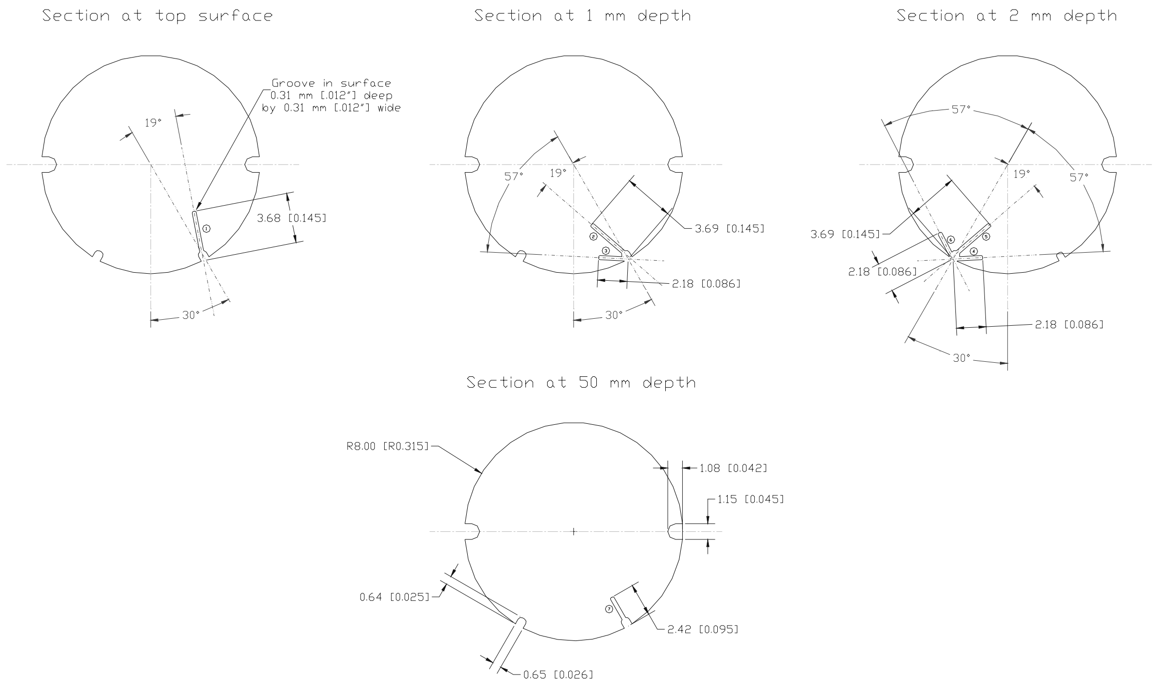

Figure 6: Groove locations in the glass wafers for thermocouple placement (dimensions in mm).

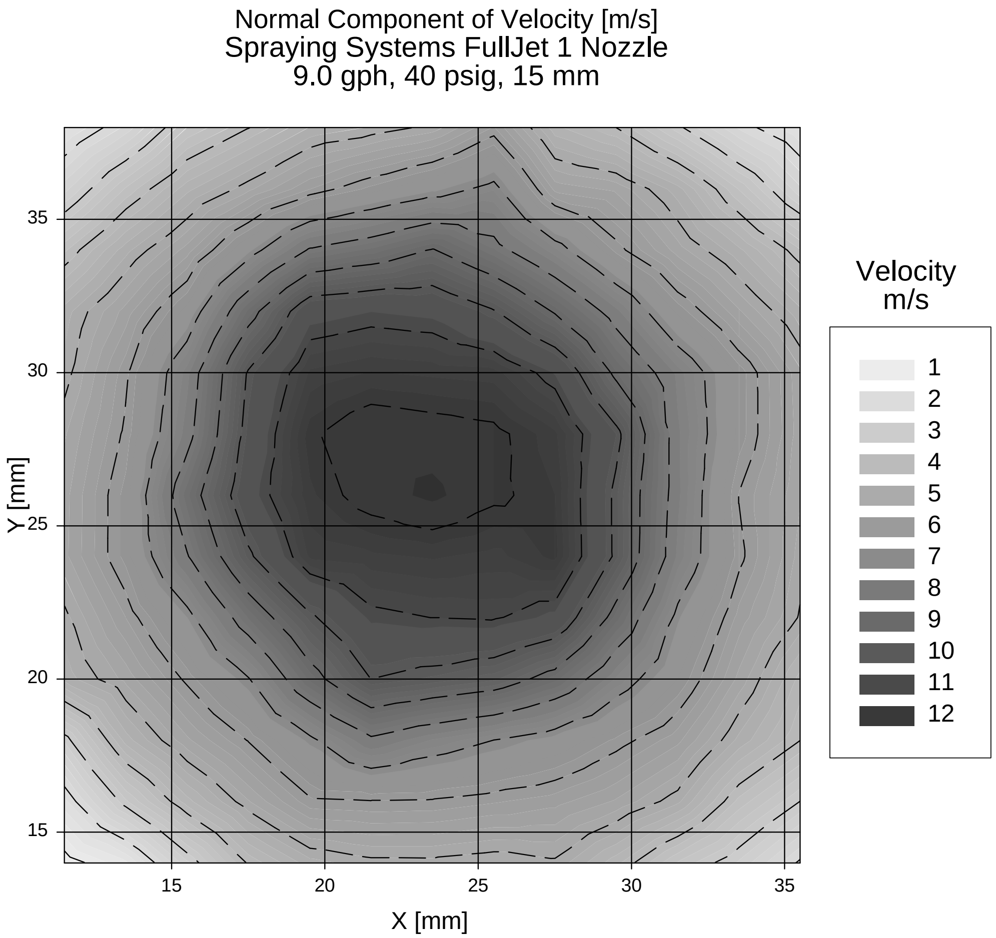

Figure 7: Normal component of velocity for the nozzle (Spraying Systems FullJet1, $V = 9.0$ gal/hr, $p = 40$ psig, $h_\mathrm{j} = 0.015$ m from orifice).

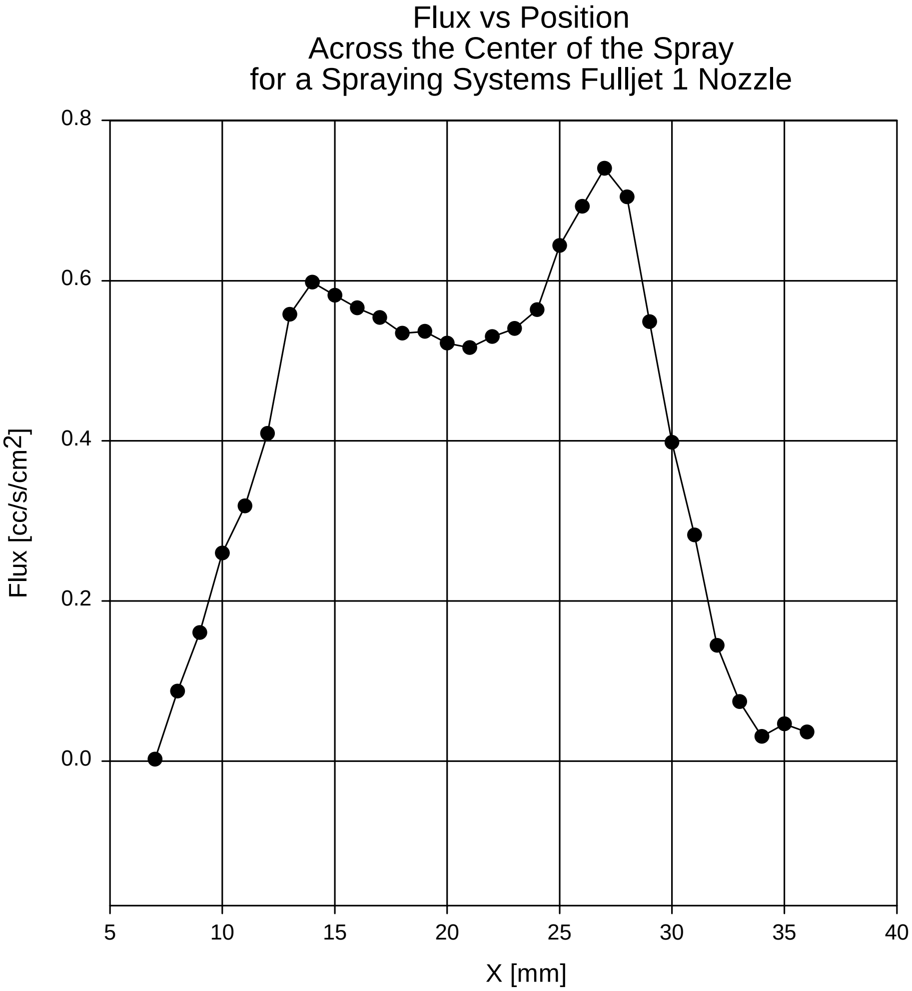

Figure 8: Volumetric flux versus position across center of spray (Spraying Systems FullJet1 nozzle, h_j = 0.017 m from the orifice).

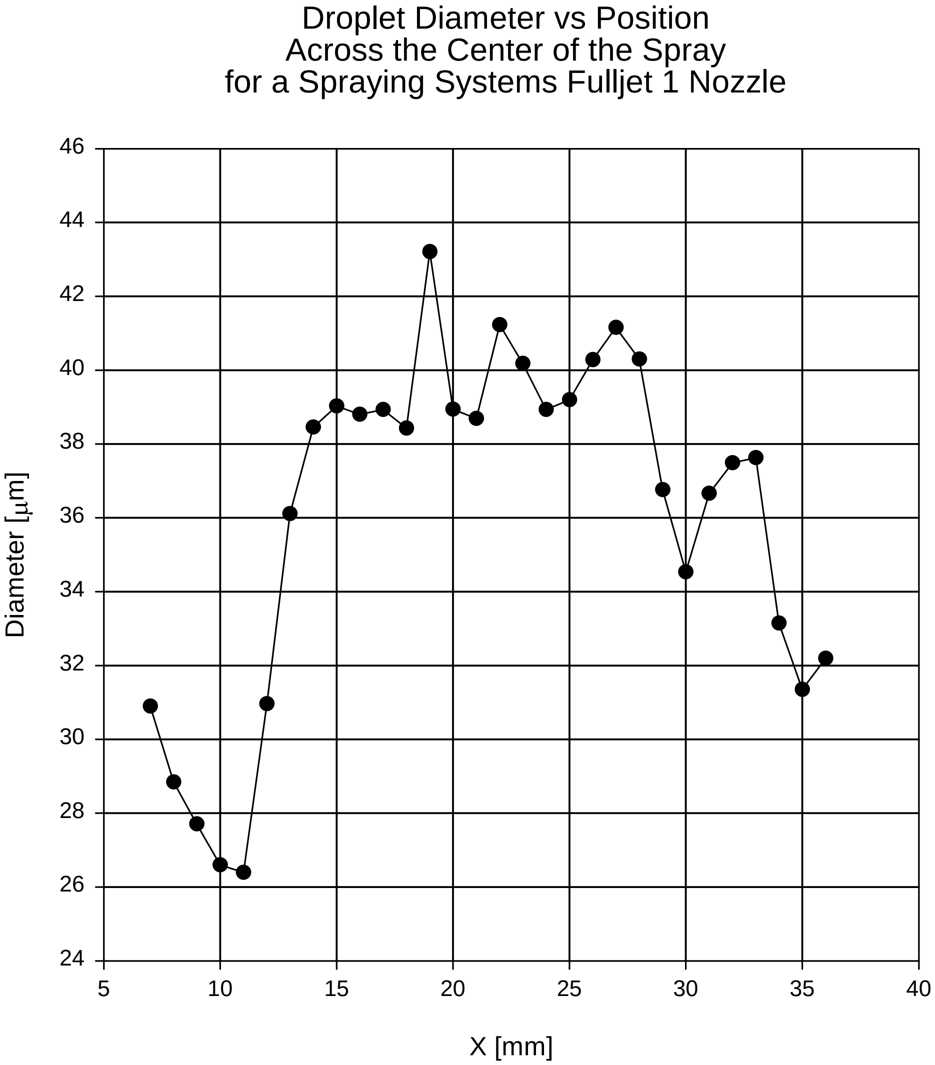

Figure 9: Mean droplet diameter versus position across center of spray (Spraying Systems FullJet1 nozzle, h_j = 0.017 m from orifice).

Figure 10: Solidworks model and photographs of the heater pedestal assembly and sump configuration.

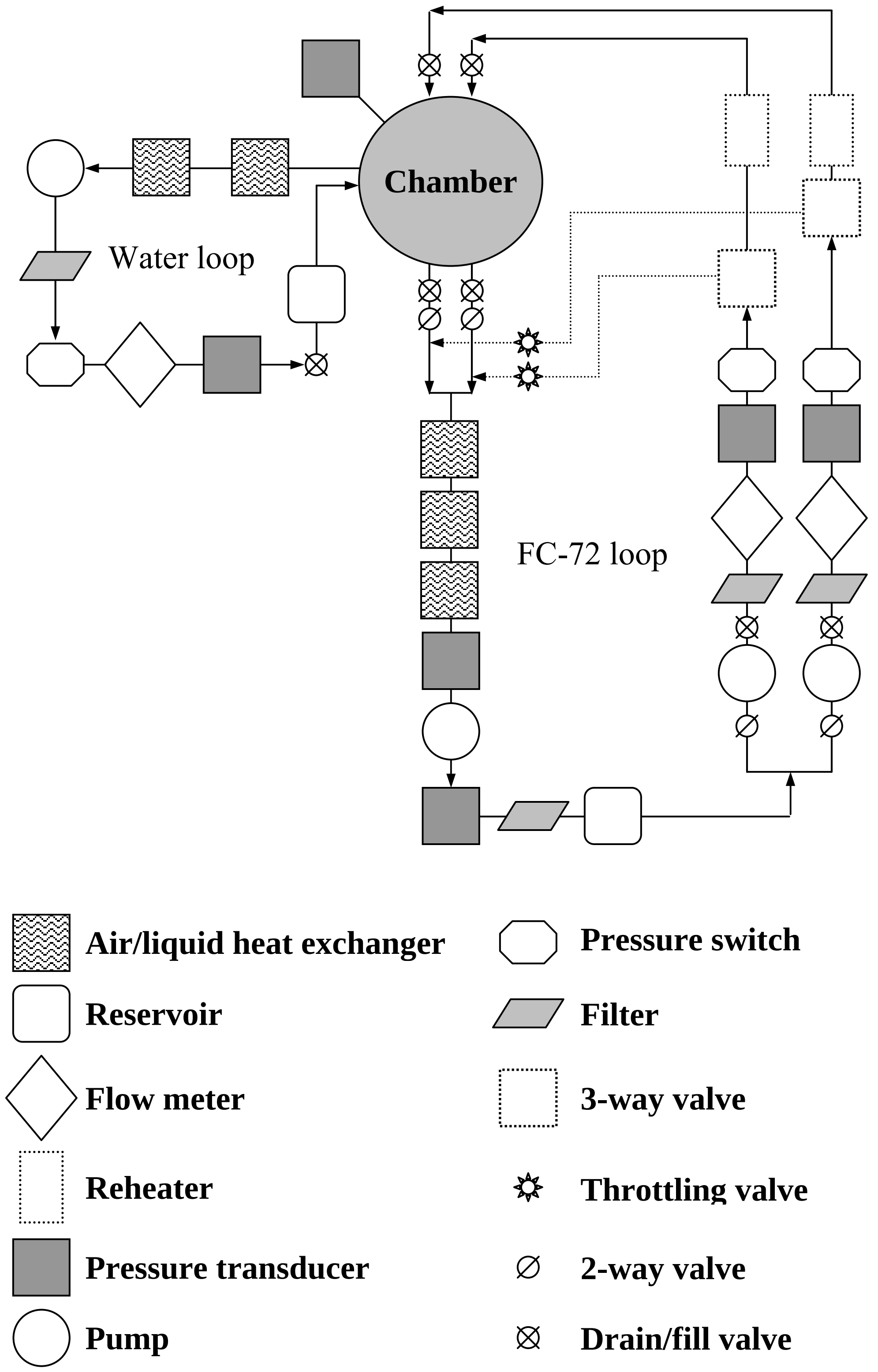

Figure 11: Schematic diagram of the flow loop system.

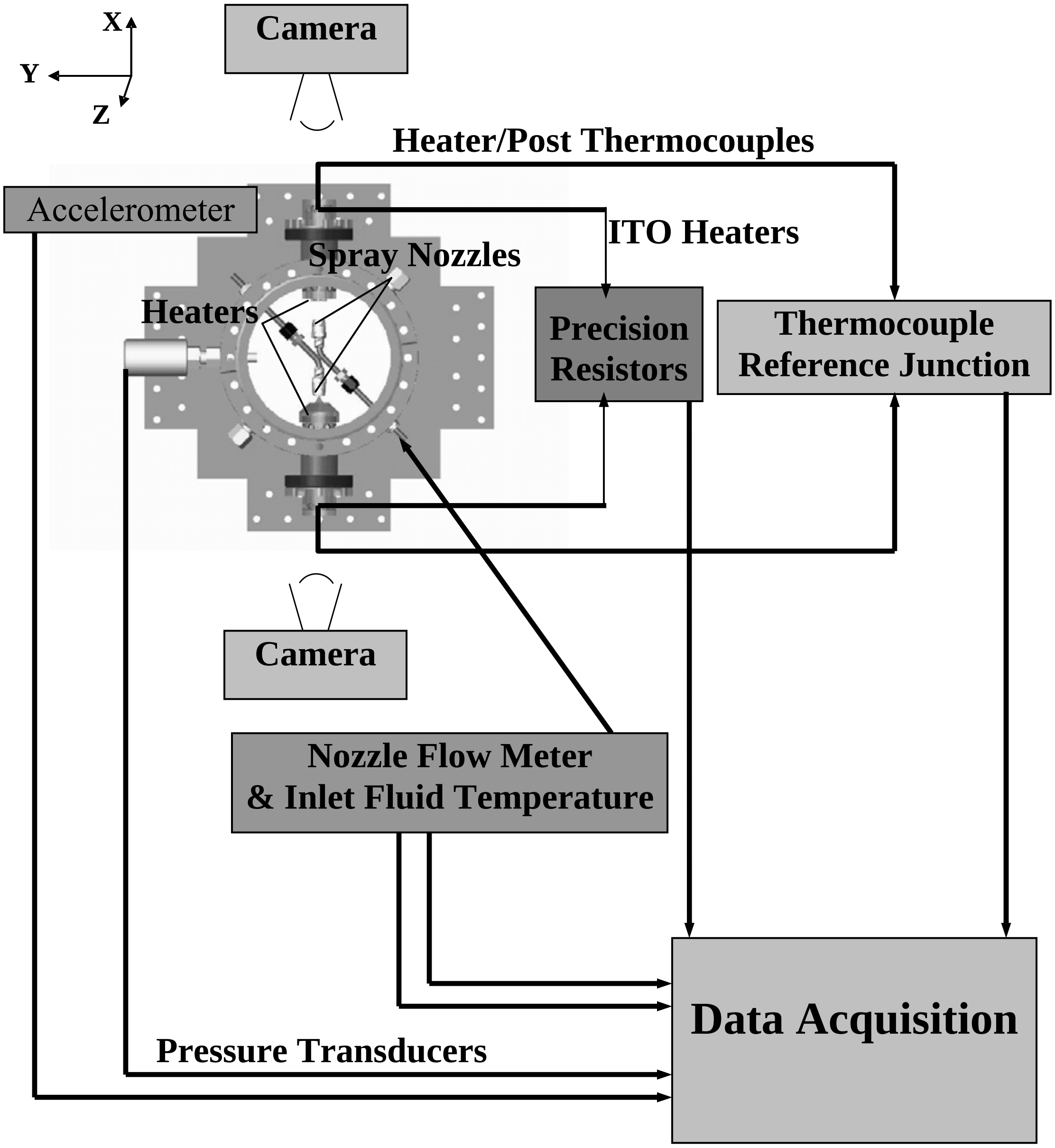

Figure 12: Schematic diagram of the instrumentation.

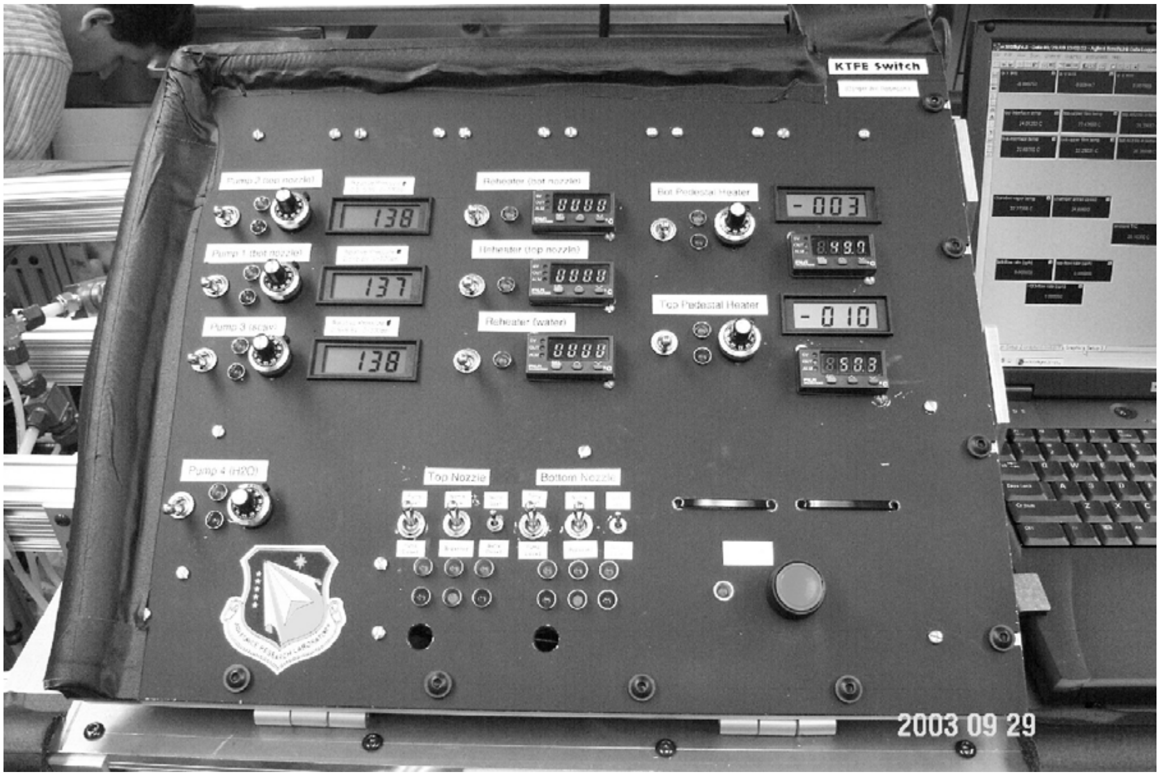

Figure 13: Photograph of the control panel.

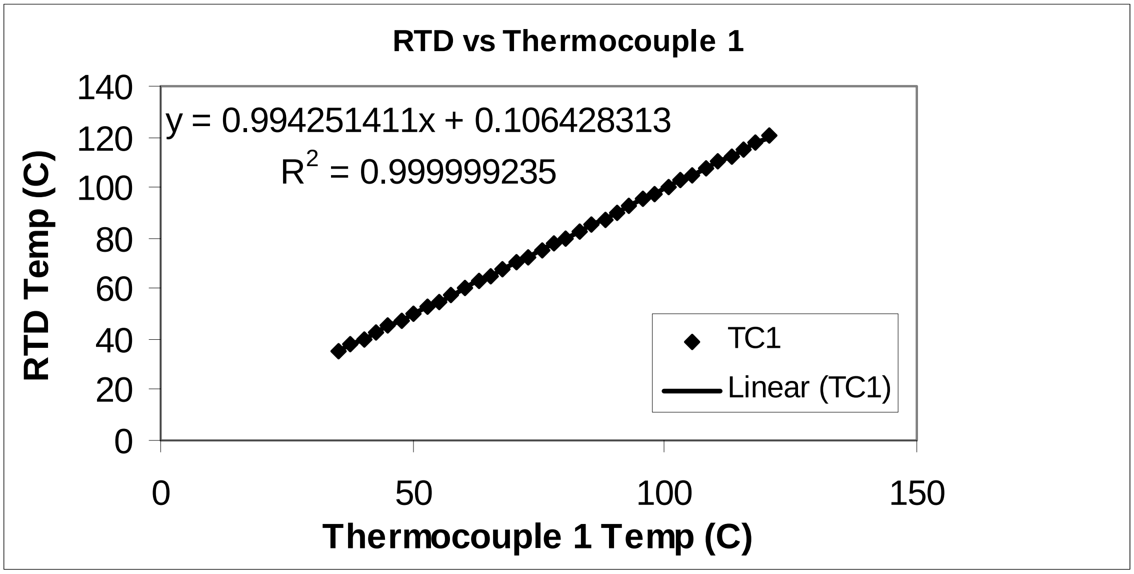

Figure 14: Typical thermocouple calibration curve.

III. Mathematical Model of the Glass Heater Pedestal Assembly

The objective of this section is to mathematically describe the glass heater pedestal assembly, which was fabricated as a series of five layers as shown in Figure 15. The ITO layer used for ohmic heating was sputter-deposited onto the first layer of glass substrate. Two additional thicker layers of glass substrate were machined with grooves to accept thermocouples to measure temperatures within the assembled glass heater pedestal assembly. The three layers of glass were mounted onto the glass pedestal base using optical cement. The entire assembly was placed into the spray chamber under the spray nozzle. The liquid spray impinged onto the top surface of the ITO heater. The liquid droplets were able to either evaporate or flow off of the surface due to the combined effects of gravity and the momentum of the spray. While part of the spray was able to rebound off of the heater surface, most of the liquid ran off the top surface and down the pedestal, either in rivulets or as a liquid film. For the ITO heater layer, assuming that the thermal properties are constant, the transient conservation of energy equation is (Rohsenow et al., 1985)

$$\rho_1 c_{\mathrm{p},1} \frac{\partial T_1}{\partial t} = k_1 \left[\frac{1}{r} \frac{\partial}{\partial r}\left(r \frac{\partial T_1}{\partial r} \right) + \frac{1}{r^2} \frac{\partial^2 T_1}{\partial \theta^2} + \frac{\partial^2 T_1}{\partial z^2} \right] + q_1'''$$

where q_1''' is the internal heat generation per unit volume due to ohmic heating. On the top surface of the ITO heater, the heat transfer coefficient is assumed to vary along the radial and azimuthal directions due to the fact that the spray may not be uniform. Also, the heat transfer coefficient is potentially transient if the liquid flow rate of the spray varies with time:

$$0 \le r \le R_\mathrm{p}, \quad 0 \le \theta \le 2\pi, \quad z = H_\mathrm{p}, \quad t > 0: \quad -k_1 \frac{\partial T_1}{\partial z} = h_1 (T_\mathrm{w} - T_{\mathrm{f},1})$$

where $h_1 = h_1(r,\theta,z=H_\mathrm{p},t)$ is the heat transfer coefficient at the top surface, T_w is the local wall temperature, and $T_{\mathrm{f},1}$ is the local film temperature of the liquid flowing over the heater surface. On the bottom face of the ITO heater, the temperature and heat flux are continuous due to the perfect thermal contact of the heater with the first layer of glass substrate, which is a result of the sputtering process, giving a boundary condition of

$$0 \le r \le R_\mathrm{p}, \quad 0 \le \theta \le 2\pi, \quad z = H_2 + H_3 + H_4 + H_5, \quad t > 0: \quad k_1 \frac{\partial T_1}{\partial z} = k_2 \frac{\partial T_2}{\partial z}, \quad T_1 = T_2$$

Within the first layer of glass substrate, the energy equation is given as follows, again assuming that the properties of the glass do not vary with temperature.

$$\rho_2 c_{\mathrm{p},2} \frac{\partial T_2}{\partial t} = k_2 \left[\frac{1}{r}\frac{\partial}{\partial r}\left(r \frac{\partial T_2}{\partial r} \right) + \frac{1}{r^2}\frac{\partial^2 T_2}{\partial \theta^2} + \frac{\partial^2 T_2}{\partial z^2} \right]$$

The first layer of glass substrate is adhered to the second thicker layer of glass with optical cement. Therefore, the boundary condition at the bottom face of the first glass layer can be modeled using the contact conductance of the interface (Ozisik, 1993):

$$0 \le r \le R_\mathrm{p}, \quad 0 \le \theta \le 2\pi, \quad z = H_3 + H_4 + H_5, \quad t > 0: \quad -k_2 \frac{\partial T_2}{\partial z} = h_{\mathrm{c},2}(T_2 - T_3) = -k_3 \frac{\partial T_3}{\partial z}$$

where $h_{\mathrm{c},2}$ is the contact conductance at this interface. For the second layer of glass, the conservation of energy equation is

$$\rho_3 c_{\mathrm{p},3} \frac{\partial T_3}{\partial t} = k_3 \left[\frac{1}{r}\frac{\partial}{\partial r}\left(r \frac{\partial T_3}{\partial r} \right) + \frac{1}{r^2}\frac{\partial^2 T_3}{\partial \theta^2} + \frac{\partial^2 T_3}{\partial z^2} \right]$$

Again, the boundary condition on the lower face of the second glass layer can be modeled using the contact conductance.

$$0 \le r \le R_\mathrm{p}, \quad 0 \le \theta \le 2\pi, \quad z = H_4 + H_5, \quad t > 0: \quad -k_3 \frac{\partial T_3}{\partial z} = h_{\mathrm{c},3}(T_3 - T_4) = -k_4 \frac{\partial T_4}{\partial z}$$

For the third layer of glass, the conservation of energy equation is

$$\rho_4 c_{\mathrm{p},4} \frac{\partial T_4}{\partial t} = k_4 \left[\frac{1}{r}\frac{\partial}{\partial r}\left(r \frac{\partial T_4}{\partial r} \right) + \frac{1}{r^2}\frac{\partial^2 T_4}{\partial \theta^2} + \frac{\partial^2 T_4}{\partial z^2} \right]$$

The boundary condition on the lower face of the third glass layer can again be modeled using the contact conductance.

$$0 \le r \le R_{\mathrm{p}}, \quad 0 \le \theta \le 2\pi, \quad z = H_5, \quad t > 0: \quad -k_4 \frac{\partial T_4}{\partial z} = h_{\mathrm{c},4}\left(T_4 - T_5\right) = -k_5 \frac{\partial T_5}{\partial z}$$

The conservation of energy equation for the glass base is

$$\rho_5 c_{\mathrm{p},5} \frac{\partial T_5}{\partial t} = k_5 \left[\frac{1}{r} \frac{\partial}{\partial r} \left(r \frac{\partial T_5}{\partial r} \right) + \frac{1}{r^2} \frac{\partial^2 T_5}{\partial \theta^2} + \frac{\partial^2 T_5}{\partial z^2} \right]$$

The lower face of the glass base is assumed to be perfectly insulated, due to its length and low thermal conductivity.

$$0 \le r \le R_{\mathrm{p}}, \quad 0 \le \theta \le 2\pi, \quad z = 0, \quad t > 0: \quad \frac{\partial T_5}{\partial z} = 0$$

Along the outer radius of the ITO heater, the glass substrate layers and the glass base, the heat transfer coefficient varies due to the complicated transient behavior of the liquid as it falls, either in rivulets or as a thin liquid film. Therefore, the boundary conditions along the outer radius of these regions are as follows:

ITO heater:

$$r = R_{\mathrm{p}}, \quad 0 \le \theta \le 2\pi, \quad H_2 + H_3 + H_4 + H_{\mathrm{s}} \le z \le H_{\mathrm{p}}, \quad t > 0: \quad -k_1 \frac{\partial T_1}{\partial r} = h_2 (T_{\mathrm{w}} - T_{\mathrm{f},2})$$

First glass layer:

$$r = R_{\mathrm{p}}, \quad 0 \le \theta \le 2\pi, \quad H_3 + H_4 + H_{\mathrm{s}} \le z \le H_{\mathrm{p}} - H_1, \quad t > 0: \quad -k_2 \frac{\partial T_2}{\partial r} = h_2 (T_{\mathrm{w}} - T_{\mathrm{f},2})$$

Second glass layer:

$$r = R_{\mathrm{p}}, \quad 0 \le \theta \le 2\pi, \quad H_4 + H_{\mathrm{s}} \le z \le H_3 + H_4 + H_5, \quad t > 0: \quad -k_3 \frac{\partial T_3}{\partial r} = h_2 (T_{\mathrm{w}} - T_{\mathrm{f},2})$$

Third glass layer:

$$r = R_{\mathrm{p}}, \quad 0 \le \theta \le 2\pi, \quad H_{\mathrm{s}} \le z \le H_4 + H_5, \quad t > 0: \quad -k_4 \frac{\partial T_4}{\partial r} = h_2 (T_{\mathrm{w}} - T_{\mathrm{f},2})$$

Glass base:

$$r = R_{\mathrm{p}}, \quad 0 \le \theta \le 2\pi, \quad 0 \le z \le H_5, \quad t > 0: \quad -k_1 \frac{\partial T_1}{\partial r} = h_2 (T_{\mathrm{w}} - T_{\mathrm{f},2})$$

where $h_2 = h_2(r = R_\mathrm{p}, \theta, z, t)$ is the heat transfer coefficient along the outer radius of the glass heater pedestal assembly, $T_\mathrm{w} = T_\mathrm{w}(\theta, z, t)$ is the local wall temperature and $T_{\mathrm{f},2} = T_{\mathrm{f},2}(\theta, z, t)$ is the local film temperature of the liquid falling down the side.

The initial conditions for the above conservation of energy equations are that the temperature throughout the entire domain is assumed to be constant:

$$0 \le r \le R_\mathrm{p}, \quad 0 \le \theta \le 2\pi, \quad 0 \le z \le H_\mathrm{p}, \quad t = 0: \quad T_1 = T_2 = T_3 = T_4 = T_5 = T_0$$

where T_0 is the initial temperature.

For the present analysis, the following assumptions have been made:

1. Steady state conditions prevail.
2. The thermophysical properties of the first glass layer correspond to the Corning glass, whereas the second and third glass layers and the glass base are made of borosilicate glass. The properties of the ITO heater are also specified.

   $$k_1 = k_\mathrm{ITO}, \ \rho_1 = \rho_\mathrm{ITO}, \ c_{\mathrm{p},1} = c_{\mathrm{p,ITO}}$$

   $$k_2 = k_\mathrm{cg}, \ \rho_2 = \rho_\mathrm{cg}, \ c_{\mathrm{p},2} = c_{\mathrm{p,cg}}$$

   $$k_3 = k_4 = k_5 = k_\mathrm{bg}, \ \rho_3 = \rho_4 = \rho_5 = \rho_\mathrm{bg}, \ c_{\mathrm{p},3} = c_{\mathrm{p},4} = c_{\mathrm{p},5} = c_{\mathrm{p,bg}}$$

3. The heat transfer coefficient on the top surface of the ITO heater is constant.

   $$h_1(r, \theta, z = H_\mathrm{p}, t) = \text{constant}$$

4. The heat transfer coefficient on the outer radius of the glass heater pedestal assembly is constant.

   $$h_2(r = R_\mathrm{p}, \theta, z, t) = \text{constant}$$

5. The contact conductances at the interfaces of the glass layers are infinite, which means that both the temperatures and heat fluxes at these interfaces are continuous.
6. The temperatures used to define the heat transfer coefficients are obtained from the experimental data. The freestream temperature for the spray heat transfer coefficient is the average of the fluid temperature entering the nozzle and the upper film temperature.

   $$T_{\mathrm{f},1} = \frac{1}{2}\left(T_\mathrm{noz} + T_\mathrm{uf}\right)$$

7. The freestream temperature for the heat transfer coefficient on the side of the heater pedestal assembly is the average of the upper and lower film temperatures.

   $$T_{\mathrm{f},2} = \frac{1}{2}\left(T_{\mathrm{uf}} + T_{\mathrm{lf}}\right)$$

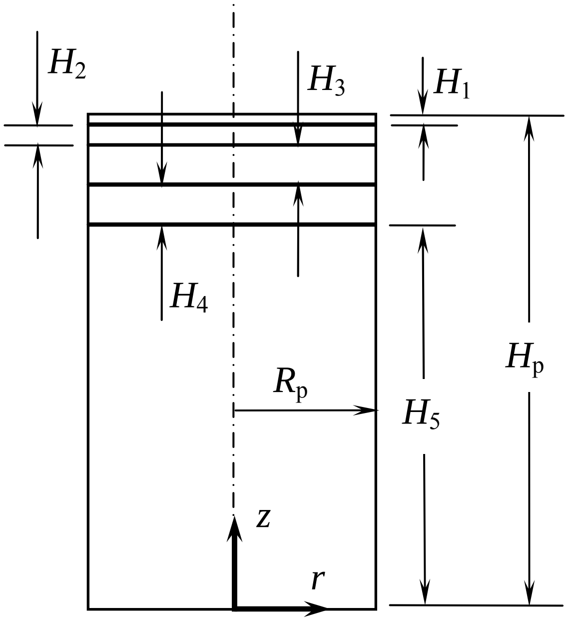

Figure 15: Schematic diagram of the glass heater pedestal assembly.

IV. Numerical Model of the Glass Heater Pedestal Assembly

The objective of this section is twofold: First, a preliminary analysis will be described in which transient temperature distributions within a right-circular cylinder were determined both analytically and numerically. This study was performed in order to become confident with the computer program used in this analysis (ANSYS 5.4 finite element software). Secondly, time-step and grid independence studies will be outlined to show that the results of the numerical heat transfer analysis for the glass heater pedestal assembly are grid independent.

Preliminary Analysis

Prior to modeling of the glass heater pedestal assembly, the results of an analytical, two-dimensional, transient heat conduction model of a right circular cylinder were compared to those of a numerical finite element model using the software package ANSYS 5.4. In this way, expertise was developed in the modeling of heat conduction problems, which could then be used to model the glass heater pedestal assembly. Beginning with the energy equation in cylindrical coordinates, appropriate assumptions were made and boundary and initial conditions were applied to determine the solution analytically. The corresponding numerical model was then developed, and transient temperature profiles within the right circular cylinder were obtained. The results of the analytical model and those of the numerical model were compared, and it was found that the two models were in agreement.

A schematic diagram of the analytical model of the transient heat conduction within a right circular cylinder of finite length is shown in Figure 16(*a*). The energy equation for this case is given by Rohsenow (1985):

$$\rho c_{\mathrm{p}} \frac{\partial T}{\partial t} = \nabla \cdot k \nabla T + q''' \tag{4.1}$$

It is assumed that all of the thermal properties are constant, there is no internal heat generation, and that the solution domain is axisymmetric, as shown in Figure 16(*b*). Under these assumptions, the energy equation reduces to

$$\frac{\partial^2 T}{\partial r^2} + \frac{1}{r}\frac{\partial T}{\partial r} + \frac{\partial^2 T}{\partial z^2} = \frac{1}{\alpha}\frac{\partial T}{\partial t} \tag{4.2}$$

On the top face of the cylinder, a constant heat flux is applied.

$$0 \le r \le R, \quad z = H, \quad t > 0: \quad \frac{\partial T}{\partial z} = -\frac{q_0''}{k} \tag{4.3}$$

On the bottom face, the temperature is zero.

$$0 \le r \le R, \quad z = 0, \quad t > 0: \quad T = 0\,\mathrm{K} \tag{4.4}$$

At the centerline, the symmetry condition is imposed.

$$r = 0, \quad 0 \le z \le H, \quad t > 0: \quad \frac{\partial T}{\partial r} = 0 \tag{4.5}$$

At the outer radius of the cylinder, the temperature is zero.

$$r = R, \quad 0 \le z \le H, \quad t > 0: \quad T = 0\,\mathrm{K} \tag{4.6}$$

At the initial time, the temperature throughout the cylinder is constant.

$$0 \le r \le R, \quad 0 \le z \le H, \quad t = 0: \quad T = T_\mathrm{i} \tag{4.7}$$

The energy equation and the boundary and initial conditions are nondimensionalized using the following definitions:

$$T^* = \frac{T}{T_\mathrm{i}}, \qquad z^* = \frac{z}{H}, \qquad r^* = \frac{r}{H}, \qquad t^* = \frac{\alpha t}{H^2}$$

The conservation of energy equation becomes

$$\frac{\partial^2 T^*}{\partial r^{*2}} + \frac{1}{r^*}\frac{\partial T^*}{\partial r^*} + \frac{\partial^2 T^*}{\partial z^{*2}} = \frac{\partial T^*}{\partial t^*} \tag{4.8}$$

The boundary conditions and the initial condition reduce to

$$0 \le r^* \le B, \quad z^* = 1, \quad t^* > 0: \quad \frac{\partial T^*}{\partial z^*} = -q_0''^* \tag{4.8a}$$

$$0 \le r^* \le B, \quad z^* = 0, \quad t^* > 0: \quad T^* = 0 \tag{4.8b}$$

$$r^* = 0, \quad 0 \le z^* \le 1, \quad t^* > 0: \quad \frac{\partial T^*}{\partial r^*} = 0 \tag{4.8c}$$

$$r^* = B, \quad 0 \le z^* \le 1, \quad t^* > 0: \quad T^* = 0 \tag{4.8d}$$

$$0 \le r^* \le B, \quad 0 \le z^* \le 1, \quad t^* = 0: \quad T^* = 1 \tag{4.8e}$$

where the aspect ratio is $B = R/H$ and the dimensionless heat flux is given by

$$q_0^{''}* = \frac{q_0^{''} H}{k T_i} \tag{4.9}$$

Due to the linear nature of the above dimensionless problem, it can be divided into a transient portion and a steady-state portion, where each of the sub-problems contains one nonhomogeneous condition (Figure 17). The dimensionless temperature is defined as $T^* = T_1 + T_2$, where the *'s have been dropped for clarity. The steady-state problem is given by the following equations:

$$\frac{\partial^2 T_1}{\partial r^2} + \frac{1}{r}\frac{\partial T_1}{\partial r} + \frac{\partial^2 T_1}{\partial z^2} = 0 \tag{4.10}$$

$$0 \le r \le B, \quad z = 1: \quad \frac{\partial T_1}{\partial z} = -q_0^{''} \tag{4.10a}$$

$$0 \le r \le B, \quad z = 0: \quad T_1 = 0 \tag{4.10b}$$

$$r = 0, \quad 0 \le z \le 1: \quad \frac{\partial T_1}{\partial r} = 0 \tag{4.10c}$$

$$r = B, \quad 0 \le z \le 1: \quad T_1 = 0 \tag{4.10d}$$

The transient portion of the problem is:

$$\frac{\partial^2 T_2}{\partial r^2} + \frac{1}{r}\frac{\partial T_2}{\partial r} + \frac{\partial^2 T_2}{\partial z^2} = \frac{\partial T_2}{\partial t} \tag{4.11}$$

$$0 \le r \le B, \quad z = 1: \quad \frac{\partial T_2}{\partial z} = 0 \tag{4.11a}$$

$$0 \le r \le B, \quad z = 0: \quad T_2 = 0 \tag{4.11b}$$

$$r = 0, \quad 0 \le z \le 1: \quad \frac{\partial T_2}{\partial r} = 0 \tag{4.11c}$$

$$r = B, \quad 0 \le z \le 1: \quad T_2 = 0 \tag{4.11d}$$

$$0 \le r \le B, \quad 0 \le z \le 1, \quad t = 0: \quad T_2 = 1 - T_1(r, z) \tag{4.11e}$$

The steady state portion of the problem is solved by assuming the functional form of the solution is $T_1(r, z) = P(r)S(z)$. Separation of variables produces the following equations and boundary conditions.

$$\frac{d^2S}{dz^2} - S\tau^2 = 0 \tag{4.12}$$

$$S(B) = 0 \tag{4.12a}$$

$$\frac{d^2P}{dr^2} + \frac{1}{r}\frac{dP}{dr} + P\tau^2 = 0 \tag{4.13}$$

$$P(B) = 0 \tag{4.13a}$$

$$\left.\frac{\partial P}{\partial r}\right|_{r=0} = 0 \tag{4.13b}$$

The solution of the axial direction problem is

$$S(z) = a_2 \sinh \tau_{\mathrm{u}} z \tag{4.14}$$

and that of the radial direction is

$$P(r) = J_0(\tau_{\mathrm{u}} r) \tag{4.15}$$

where the eigenvalues $(\tau_{\mathrm{u}}\text{'s})$ are the positive roots of $J_0(\tau_{\mathrm{u}} B) = 0$. Assembling to obtain the solution to the steady-state problem $T_1(r,z) = P(r)S(z)$ and applying the nonhomogeneous boundary condition,

$$\left.\frac{\partial T_1}{\partial z}\right|_{z=1} = -q_0'' \tag{4.10a}$$

the following equation is obtained.

$$-q_0'' = \sum_{\mathrm{u}=1}^{\infty} d_{\mathrm{u}} \tau_{\mathrm{u}} J_0(\tau_{\mathrm{u}} r) \cosh \tau_{\mathrm{u}} \tag{4.16}$$

By using the principle of orthogonality, the constants can be found.

$$d_{\mathrm{u}} = \frac{-2q_0''}{B\tau_{\mathrm{u}}^2 J_1(\tau_{\mathrm{u}} B) \cosh \tau_{\mathrm{u}}} \tag{4.17}$$

Thus, the steady-state portion of the problem is

$$T_1(r,z) = \frac{-2q_0''}{B} \sum_{\mathrm{u}=1}^{\infty} \frac{J_0(\tau_{\mathrm{u}} r) \sinh \tau_{\mathrm{u}} z}{\tau_{\mathrm{u}}^2 J_1(\tau_{\mathrm{u}} B) \cosh \tau_{\mathrm{u}}} \tag{4.18}$$

where the τ_{u}'s are given by the positive roots of $J_0(\tau_{\mathrm{u}} B) = 0$.

The transient problem is solved in a similar manner by assuming that the solution can be obtained by separation of variables by letting $T_2(r, z, t) = R(r)Z(z)\Gamma(t)$. The transient dimensionless conservation of energy equation and the boundary conditions and initial condition can be solved as three separate problems:

$$\frac{d\Gamma}{dt} + \lambda^2\Gamma = 0 \tag{4.19}$$

$$\frac{d^2 Z}{dz^2} + Z\eta^2 = 0 \tag{4.20}$$

$$Z(0) = 0 \tag{4.20a}$$

$$\left.\frac{dZ}{dz}\right|_{z=1} = 0 \tag{4.20b}$$

$$\frac{d^2 R}{dr^2} + \frac{1}{r}\frac{dR}{dr} + R\beta^2 = 0 \tag{4.21}$$

$$R(B) = 0 \tag{4.21a}$$

$$\left.\frac{dR}{dr}\right|_{r=0} = 0 \tag{4.21b}$$

where the separation constants are related by $\lambda^2 = \beta^2 + \eta^2$. The solution of the transient portion of the problem is

$$\Gamma(t) = c_1 \exp[-(\beta^2 + \eta^2)t] \tag{4.22}$$

The solution of the axial direction problem is given by

$$Z(z) = b_1 \sin\eta_{\mathrm{n}} z, \quad \eta_{\mathrm{n}} = (2\mathrm{n}-1)\frac{\pi}{2}, \quad \mathrm{n} = 1, 2, 3... \tag{4.23}$$

The solution of the radial direction problem is

$$R(r) = J_0(\beta_{\mathrm{m}} r) \tag{4.24}$$

where the eigenvalues $(\beta_{\mathrm{m}}'s)$ are the positive roots of $J_0(\beta_{\mathrm{m}} B) = 0$. Assembling for the solution to the transient problem $T_2(r, z, t) = R(r)Z(z)\Gamma(t)$ and applying initial condition $T_2(r, z, 0) = 1 - T_1(r, z)$ gives

$$1 - T_1(r, z) = \sum_{\mathrm{m}=1}^{\infty}\sum_{\mathrm{n}=1}^{\infty} c_{\mathrm{mn}} J_0(\beta_{\mathrm{m}} r)\sin\eta_{\mathrm{n}} z \tag{4.25}$$

The constants can be determined by using orthogonality.

$$c_{\mathrm{mn}} = \frac{4}{B\beta_{\mathrm{m}} J_1(\beta_{\mathrm{m}} B)}\left[\frac{1}{\eta_{\mathrm{n}}} + \frac{(-1)^{\mathrm{n}}}{\beta_{\mathrm{m}}^2 + \eta_{\mathrm{n}}^2}\right] \tag{4.26}$$

Thus, the solution of the transient portion of the problem is as follows

$$T_2(r,z,t) = \frac{4}{B}\sum_{\mathrm{m}=1}^{\infty}\sum_{\mathrm{n}=1}^{\infty}\frac{1}{\beta_{\mathrm{m}} J_1(\beta_{\mathrm{m}} B)}\left[\frac{1}{\eta_{\mathrm{n}}} + \frac{(-1)^n}{\beta_{\mathrm{m}}^2 + \eta_{\mathrm{n}}^2}\right] J_0(\beta_{\mathrm{m}} r)\sin\eta_{\mathrm{n}} \mathrm{z}\cdot\exp[-(\beta^2+\eta^2)t] \tag{4.27}$$

where

$$\eta_{\mathrm{n}} = (2\mathrm{n}-1)\frac{\pi}{2}$$

and the β_{m}'s are given by the positive roots of $J_0(\beta_{\mathrm{m}} B) = 0$. Assembling for the original problem gives the dimensionless temperature distribution within the right circular cylinder

$$\begin{aligned} T^* = {} & \frac{4}{B}\sum_{\mathrm{m}=1}^{\infty}\sum_{\mathrm{n}=1}^{\infty}\frac{1}{\beta_{\mathrm{m}} J_1(\beta_{\mathrm{m}} B)}\left[\frac{1}{\eta_{\mathrm{n}}} + \frac{(-1)^n}{\beta_{\mathrm{m}}^2 + \eta_{\mathrm{n}}^2}\right] J_0(\beta_{\mathrm{m}} r^*)\sin\eta_{\mathrm{n}} z^*\cdot\exp[-(\beta^2+\eta^2)t^*] \\ & - \frac{2q_0''^*}{B}\sum_{\mathrm{m}=1}^{\infty}\frac{J_0(\beta_{\mathrm{m}} r^*)\sinh\beta_{\mathrm{m}} z^*}{\beta_{\mathrm{m}}^2 J_1(\beta_{\mathrm{m}} B)\cosh\beta_{\mathrm{m}}} \end{aligned} \tag{4.28}$$

where the asterisks have been re-introduced into the equation for clarity.

A numerical model of the right-circular cylinder was developed using ANSYS 5.4 finite element software for comparison with the analytical solution. The thermal model consisted of 8-node, Plane77, axisymmetric, quadrilateral elements. A grid independence study was performed to determine the proper number of elements for the steady state numerical model. The uniformly-meshed model was tested for 2 × 2, 4 × 4, and 10 × 10 elements. Figure 18 shows the dimensionless temperature along the radius of the model at three different *z**-locations. The results of the numerical model closely match those of the analytical solution for 10 × 10 elements. The maximum percent difference between the 10 × 10 numerical model and the analytical solution was 0.05%. A time-step convergence study was then performed on the transient model to determined appropriate values for Δ*t**. Figure 19 shows the dimensionless temperature at three *z**-locations along the centerline of the right circular cylinder *r** = 0. Here the transient numerical model is shown for time-step values of Δ*t** = 0.005, 0.01, and 0.05. For Δ*t** = 0.005, the maximum percent difference between the numerical and analytical solutions occurred at $t^* = 0.005$ and $(r^*, z^*) = (0, 1)$, with a value of 2.69%. The maximum percent difference between the numerical and analytical solutions for all other time step values was 1.49%.

Grid Independence Study

A steady state, numerical model of the cylindrical glass heater pedestal assembly was built in ANSYS, using the same preferences and elements described above. Instead of a single thickness, however, the model consisted of several layers, reflecting the structure of the heater, substrate, and post, as well as thermocouple locations within the assembly. The height of the pedestal, excluding the heater and substrate, was assumed to be $(H_3 + H_4 + H_5) = 10$ cm for modeling purposes. The height of the glass base was H_5 = 9.8 cm, and as stated in the Experimental Design and Testing section, the thickness of each borosilicate layer was $H_3 = H_4 = 1$ mm. The thickness of the Corning glass substrate was $H_2 = 0.5$ mm, and the ITO heater was $H_1 = 1$ μm thick. A thermal conductivity, $k = 1.04$ W/m-K was assumed for the entire model. To reflect the symmetry of the model, a zero-heat flux boundary condition was placed on the centerline of the structure. The spray convection was modeled as a convective heat transfer coefficient (h_1) on the top edge, and the convection from flow down the side walls of the pedestal assembly was represented by a separate convective heat transfer coefficient along the right edge of the model (h_2). The bottom of the pedestal was assumed to be adiabatic. The heater was modeled with a volumetric heat generation applied to the top-most layer (ITO) of the model.

A grid independence study was performed to ensure adequate meshing of the model. The coarse mesh was determined by thermocouple location. In the coarse mesh, the maximum element width in the r-direction was $\Delta r = 0.00235$ m. In the z-direction, the heater, substrate, and the two thin layers were each one element thick, and the remaining portion of the base was divided into 10 elements, with a spacing ratio of 30, so that the element size increased downward. This produced 56 total elements in the coarse model. The mesh was refined by doubling the number of elements in both directions, with the exception of the heater, where its thickness remained at one element. The result was a fine mesh consisting of 216 elements. Figure 20 and Figure 21 illustrate the coarse and fine meshes, respectively. For the grid independence study, convective heat transfer coefficient values of h_1 = 10,000 W/(m-K) and h_2 = 400 W/(m-K) were chosen, along with a heater power of Q = 20 W. Temperatures were recorded at all nodes and compared. The maximum percent difference between the coarse and fine meshes was 0.058%. Figure 22 shows the temperature along the radial direction for three separate z-locations. As expected, the temperature within the pedestal assembly decreases in the radial direction due to the convection at the outer radius. In addition, the temperature increases in the axial direction due to the presence of the ITO heater at the upper surface. Based on these results, it was determined that the model was sufficiently grid-independent when the fine mesh is used.

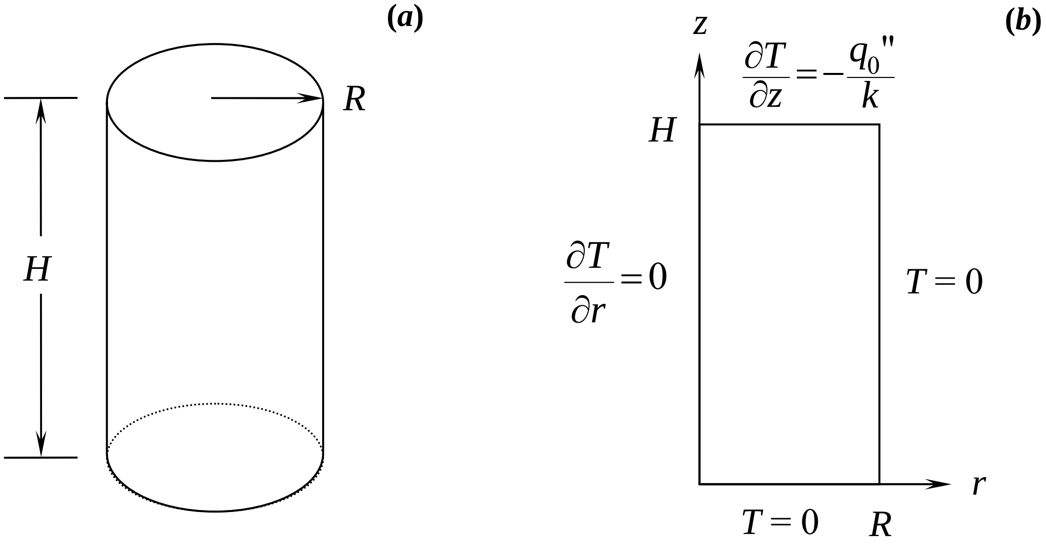

Figure 16: Transient heat conduction in a right circular cylinder: (*a*) Geometrical nomenclature; (*b*) Solution domain.

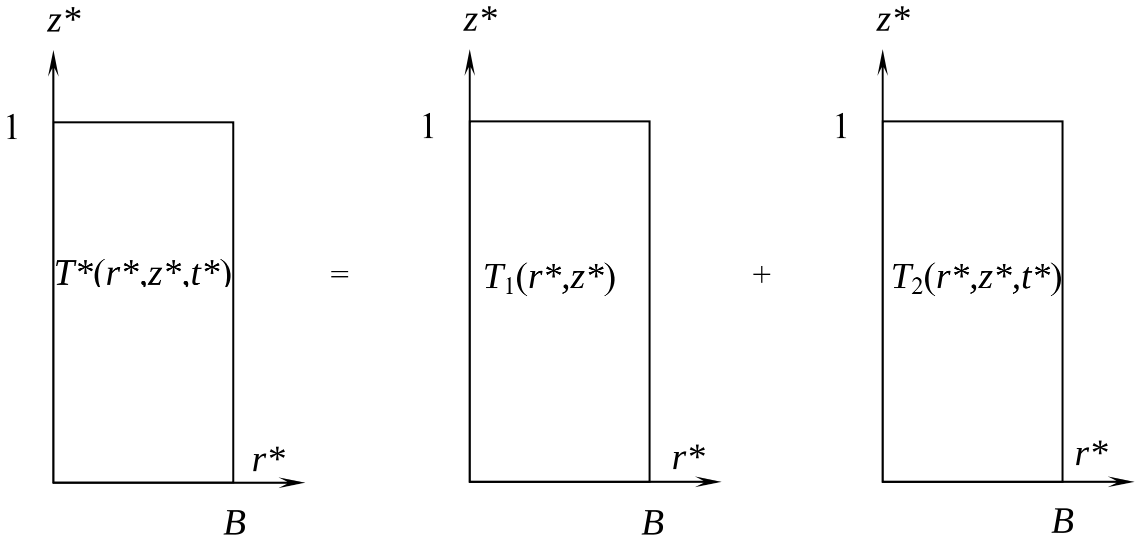

Figure 17: Division of the problem into steady-state and transient portions.

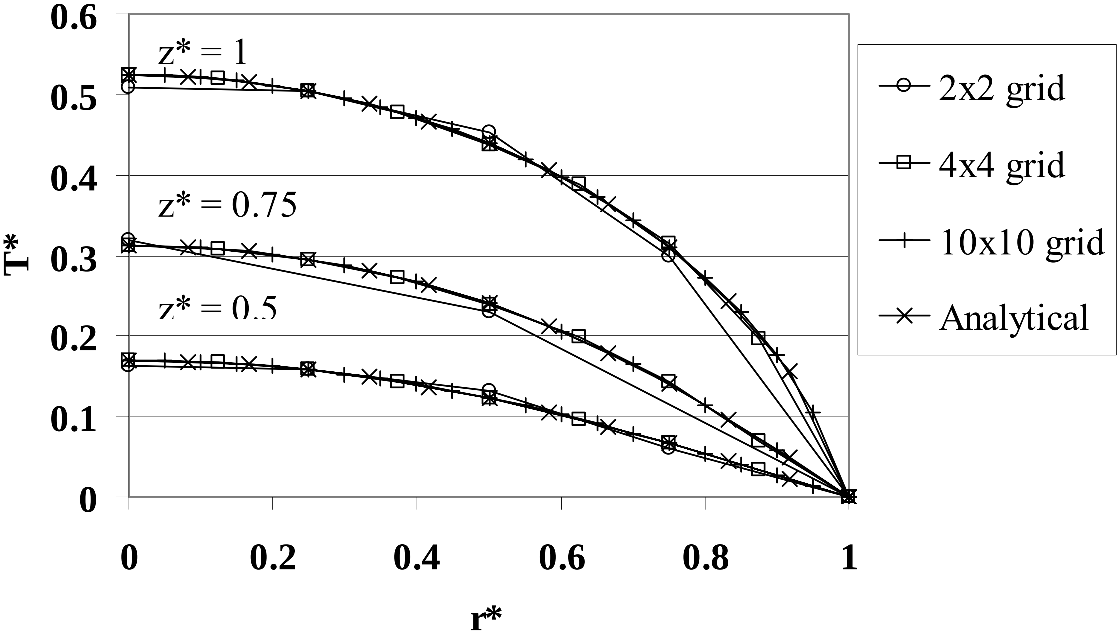

Figure 18: Dimensionless temperature versus dimensionless radius for the right circular cylinder (steady state, $B = 1, q_0''* = 1$).

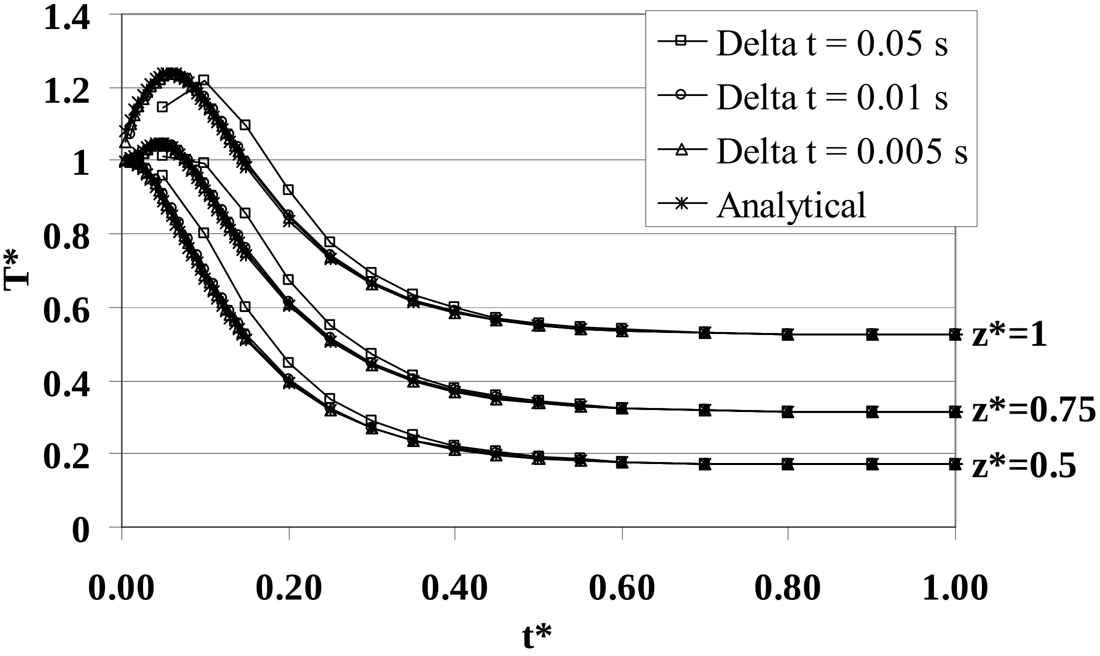

Figure 19: Dimensionless temperature versus dimensionless time for the right circular cylinder ($B = 1$, $r^* = 0, q_0''^* = 1$).

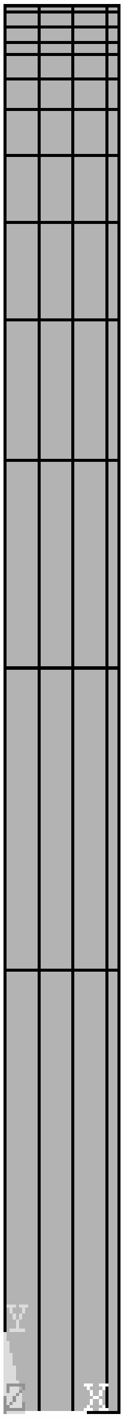

Figure 20: Coarse mesh for the glass heater pedestal assembly.

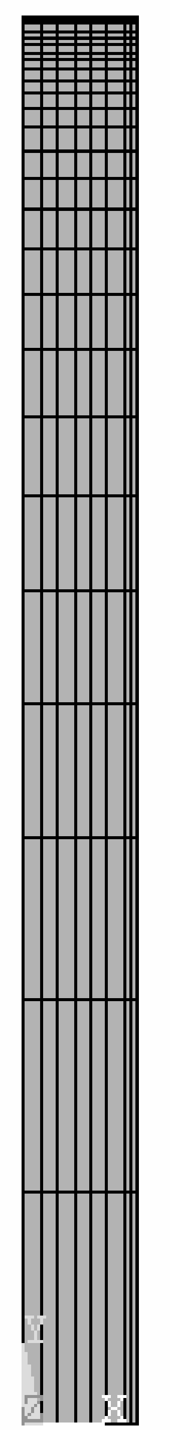

Figure 21: Fine mesh for the glass heater pedestal assembly.

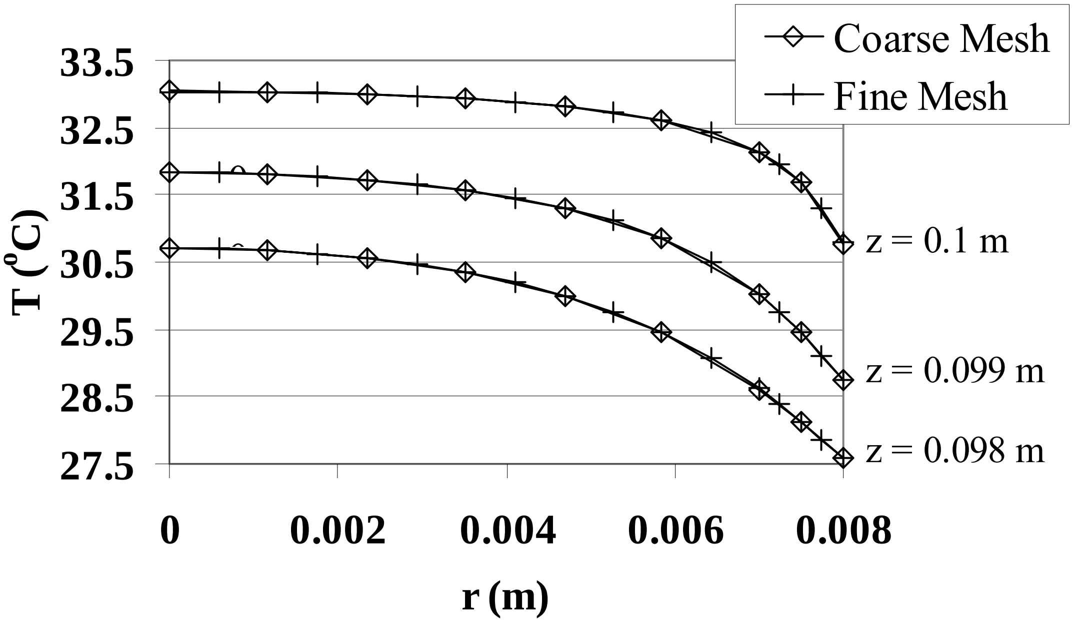

Figure 22: Temperature versus radial location for *z* = 0.1, 0.099, and 0.098 m for the coarse and fine meshes.

V. Results and Discussion

Baseline experiments using subcooled FC-72 fluid were carried out to determine the effects of the volumetric flow rate of the spray, the heat transfer rate, and heater orientation with respect to terrestrial gravity on the heat transfer coefficient on the top surface of a glass heater pedestal assembly. The ranges of the parameters in the experiments are as follows: $4.0 \le \dot{V} \le 10.0$ gal/hr, $16.0 \le Q \le 50.0$ W. Experiments were executed for two heater orientations: the bottom nozzle spraying downward onto an upward-facing heater, and the top nozzle spraying upward onto a downward-facing heater. Raw data from a typical experiment is shown in Figure 23. As can be seen, the temperatures within the pedestal assembly closely follow the heat input to the ITO heater with respect to time. The average volumetric flow rate of the spray was relatively constant, but some variation around the average can be seen, which was due to fluctuations within the fluid collection system. While the vapor pressure within the spray chamber slowly increased over the period of the test due to the heat input to the working fluid through the glass heater pedestal, the temperature of the fluid remained below the saturation temperature, T_{sat}.

In order to determine the heat transfer coefficient of the spray on the ITO heater surface, the following procedure was used. For a given experimental run in which the volumetric flow rate of the spray and the heater power were specified, the average steady-state temperatures for thermocouples 1, 2 and 3 (TC1, TC2, TC3) were recorded. The numerical model of the glass heater pedestal assembly was then used to match the experimental temperatures at the specified geometric locations of the thermocouples. This involved varying both the spray heat transfer coefficient at the top surface of the ITO heater (h_1), and the heat transfer coefficient along the outer radius of the pedestal assembly (h_2). Results from a typical comparison between the experimental data and the numerical model are shown in Figure 24. The spray heat transfer coefficient was varied over a large range, while the heat transfer coefficient on the outer radius of the pedestal assembly was fixed at a particular value. The points at which the numerical temperatures at the locations of thermocouples 1, 2, and 3 matched those of the experimental values was noted for that particular value of the outer radius heat transfer coefficient. The process was then repeated with a different value of the outer radius heat transfer coefficient, which was varied from $0 \leq h_2 \leq 400$ W/(m^2-K). This range was chosen based on experimental data reported in the open literature (Incropera and DeWitt, 2001), and is considered to be a conservative range, meaning that it is believed that the actual *average* heat transfer coefficient is within this range. It should be emphasized that the numerical model imposed a single value for the heat transfer coefficient at the outer radius. In reality, the heat transfer is probably high very close to the top surface, and quickly decreases to zero in the axial direction, and the heat transfer coefficient varies along the wall. Therefore, the assumption that the range of the average heat transfer coefficient lies between $0 \leq h_2 \leq 400$ W/(m^2-K) is justified.

Once the numerical model was run for the entire range of h_2, the range of the spray heat transfer coefficient was defined for each thermocouple by the values at which the numerical temperature values matched the experimental value. The range was contained between the intersections, at $h_2 = 0$ and $h_2 = 400$ W/(m^2-K), of the numerical data with the experimental data. This is illustrated in Figure 24, with vertical lines to show the range for each thermocouple. It should be noted that the actual value of the spray heat transfer coefficient is not known, but it is believed to lie in the range discussed above. To simplify the presentation of the data, the spray heat transfer coefficient was defined as the average of the range, as shown in Figure 25 and Figure 26. Here, error bars are used to denote the extent of the range. As can be seen, the spray heat transfer coefficient was not a strong function of the heat input, due to the fact that the fluid was subcooled. Allowing the fluid temperatures to reach those greater than the saturation temperature would have created a greater dependence on the heat input. The spray heat transfer coefficient was more dependent on the volumetric flow rate of the subcooled fluid, and increased with the flow rate of the spray, as expected. Also worth noting is that Thermocouple 1 is the most accurate predictor of spray heat transfer coefficient, since it was located closest to the heater surface and was least affected by the wall heat transfer coefficient, h_2, as demonstrated graphically in Figure 24. For all test cases, the estimated spray heat transfer coefficient was $10{,}000 \leq h_1 \leq 15{,}000$ W/(m^2-K), with an approximate rms error of $E(h_1 A) \approx 20\%$, as discussed in Baysinger, et al. (2004).

It is worth noting that the temperatures measured in the downward-facing heater pedestal assembly were generally slightly lower than those measured in the upward-facing heater pedestal. Figure 27 shows the behavior of the spray for both the downward-facing heater pedestal and the upward-facing heater pedestal. In both cases a stagnation line is visible within the sump cap. This line is created by droplets of fluid which deflect from the heater surface to the inside wall of the cap. For the upward-facing heater pedestal, the stagnation line is visible slightly above the heater surface. For the downward-facing heater pedestal, however, the stagnation line forms further up on the pedestal, in the vicinity of the thermocouples. Also visible in the region of the stagnation line is an area of turbulent flow. It is believed that the fluid in this area provides extra cooling to the pedestal, resulting in the slightly lower temperatures observed for the downward-facing heater pedestal assembly. In turn, the lower temperatures in the regions of thermocouples 2 and 3 (TC2, TC3) result in the higher estimated spray heat transfer coefficients for those locations, as illustrated in Figure 26.

While most of the heat generated was removed by the spray, a small portion was lost down the pedestal assembly via conduction. It was desired to estimate this heat conducted into the pedestal in order to validate the use of a simplified estimation of the heat transfer coefficient as outlined by Baysinger et al. (2004). The estimated spray heat transfer coefficient was used to determine the heat lost through the pedestal due to conduction, ΔQ, for several experimental tests using the upward-facing heater pedestal. First, the actual amount of heat removed by the sprayed fluid, Q_1, was found using the convection equation:

$$Q_1 = h_1(\pi R_p{}^2)(T_{\mathrm{s}}(r) - T_{\mathrm{f},1}),$$

where h_1 is the estimated spray heat transfer coefficient, R_{p} is the radius of the glass heater pedestal assembly, $T_{\mathrm{s}}(r)$ is the local surface temperature given by the numerical model, and $T_{\mathrm{f},1}$ is the experimentally measured film temperature across the top of the heater as described in the Mathematical Modeling section. The result was then used in the following equation to find ΔQ:

$$\Delta Q = 1 - \frac{Q_l}{Q_h}$$

where Q_h is the power generated by the ITO heater.

Figure 28 displays temperature versus power for the average steady state surface temperature, $\overline{T}_s$, across the heater and the temperature of the surface located directly above Thermocouple 1, $T_{s,TC1}$. As expected, increasing the power supplied to the heater results in increased temperature. Increasing the volumetric flow rate provides more coolant to the heated surface, resulting in decreased temperatures within the glass heater pedestal assembly, also shown in Figure 28.

Figure 29 shows the percent of heat lost due to conduction within the pedestal, ΔQ, over the radius of the heater surface. The heat lost increases approaching the outer edge, due to the convection along the side wall of the pedestal from the fluid moving through the sump structure. Finally, Figure 30 shows ΔQ versus the input heater power, based on $\overline{T}_s$ and based on $T_{s,TC1}$. As seen in the graph, increasing power increases ΔQ, while increasing the volumetric flow rate decreases ΔQ. In addition, the heat lost due to conduction was in the range of $\Delta Q = 1$ to 2.5% which is comparable to earlier estimates of 1% (Baysinger et al., 2004). This shows that the one-dimensional method for estimating the spray heat transfer coefficient is valid as long as the thermocouple that is used to determine the heat transfer coefficient is close to the centerline and top surface of the heater pedestal. While this information will be used in the analyses and planning of future experimental tests, it should be noted that these estimates are reliable only for subcooled conditions of the fluid.

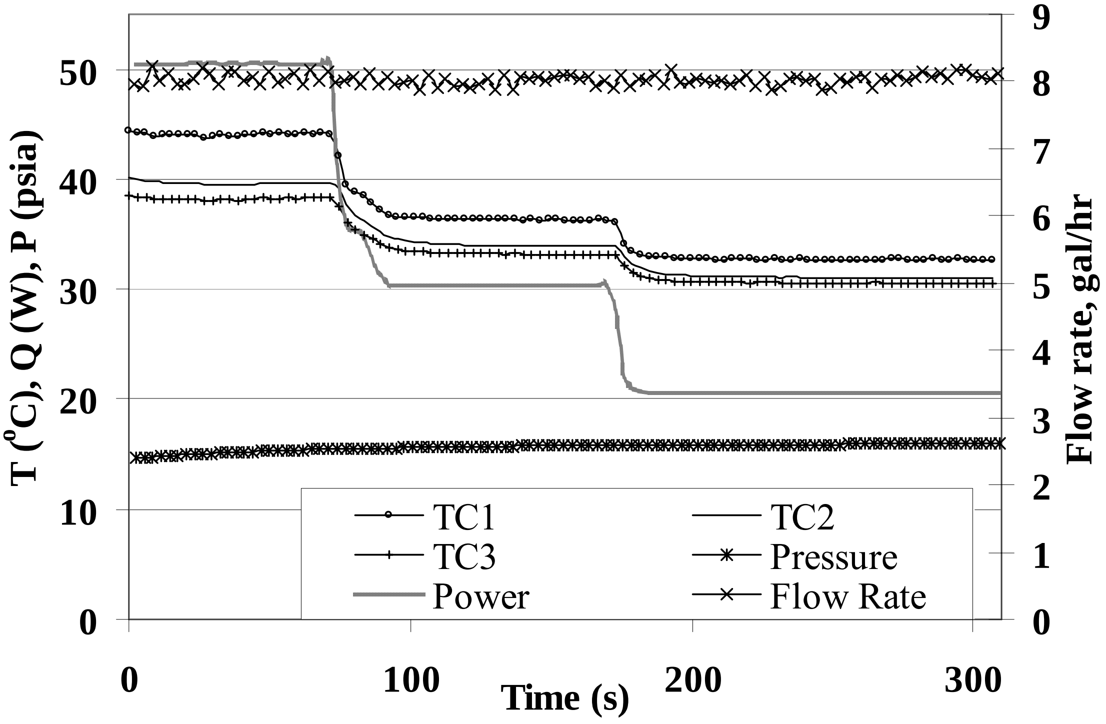

Figure 23: Temperatures within the upward-facing glass heater pedestal assembly, input power to the ITO heater, spray chamber pressure, and volumetric flow rate of the spray versus time for a typical test run.

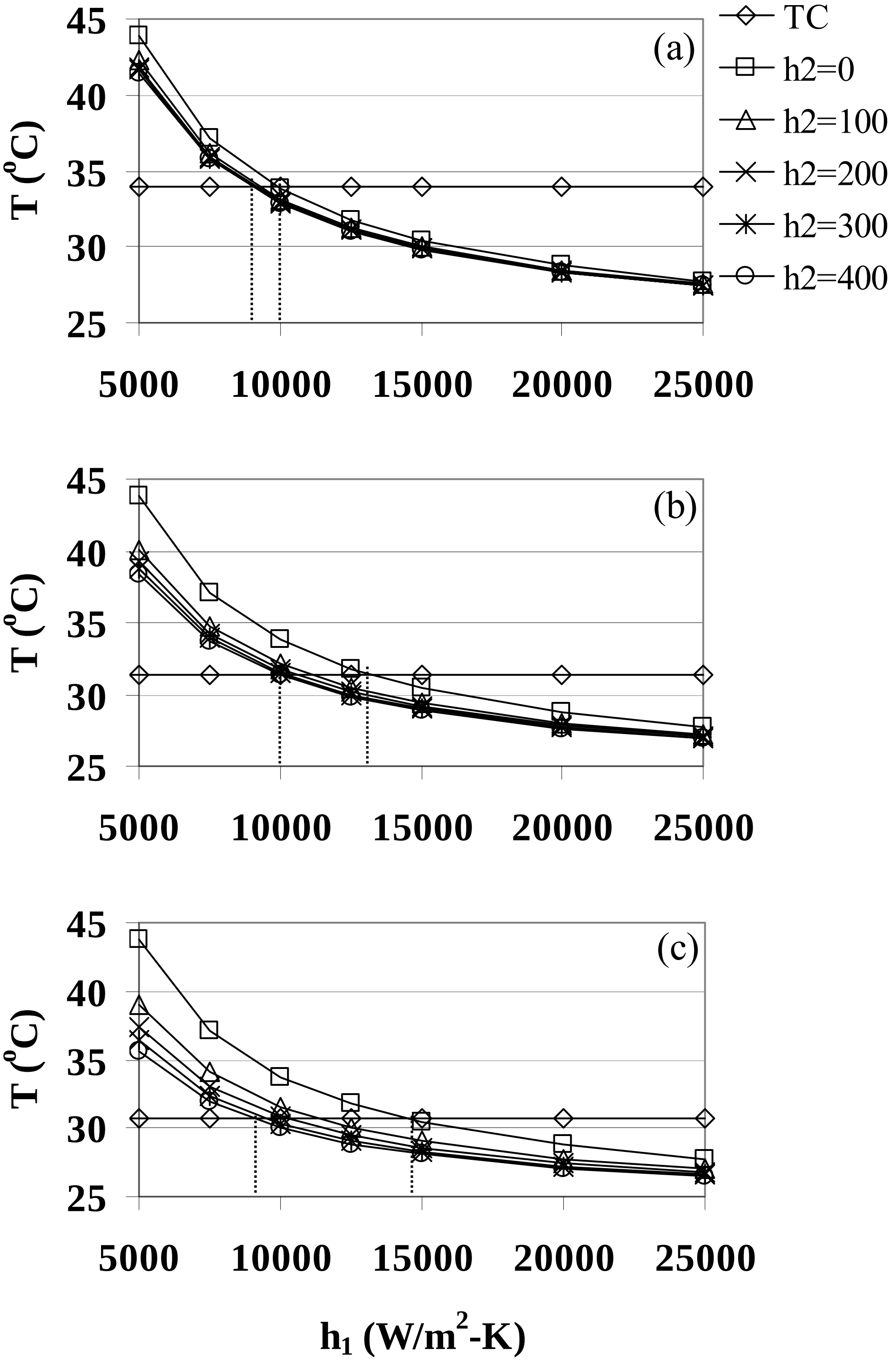

Figure 24: Thermocouple temperatures within the upward-facing glass heater pedestal assembly versus spray heat transfer coefficient, h_1 ($\dot{V} = 5.0\,\text{gal/hr}$, Q = 20 W): (a) Thermocouple 1; (b) Thermocouple 2; (c) Thermocouple 3.

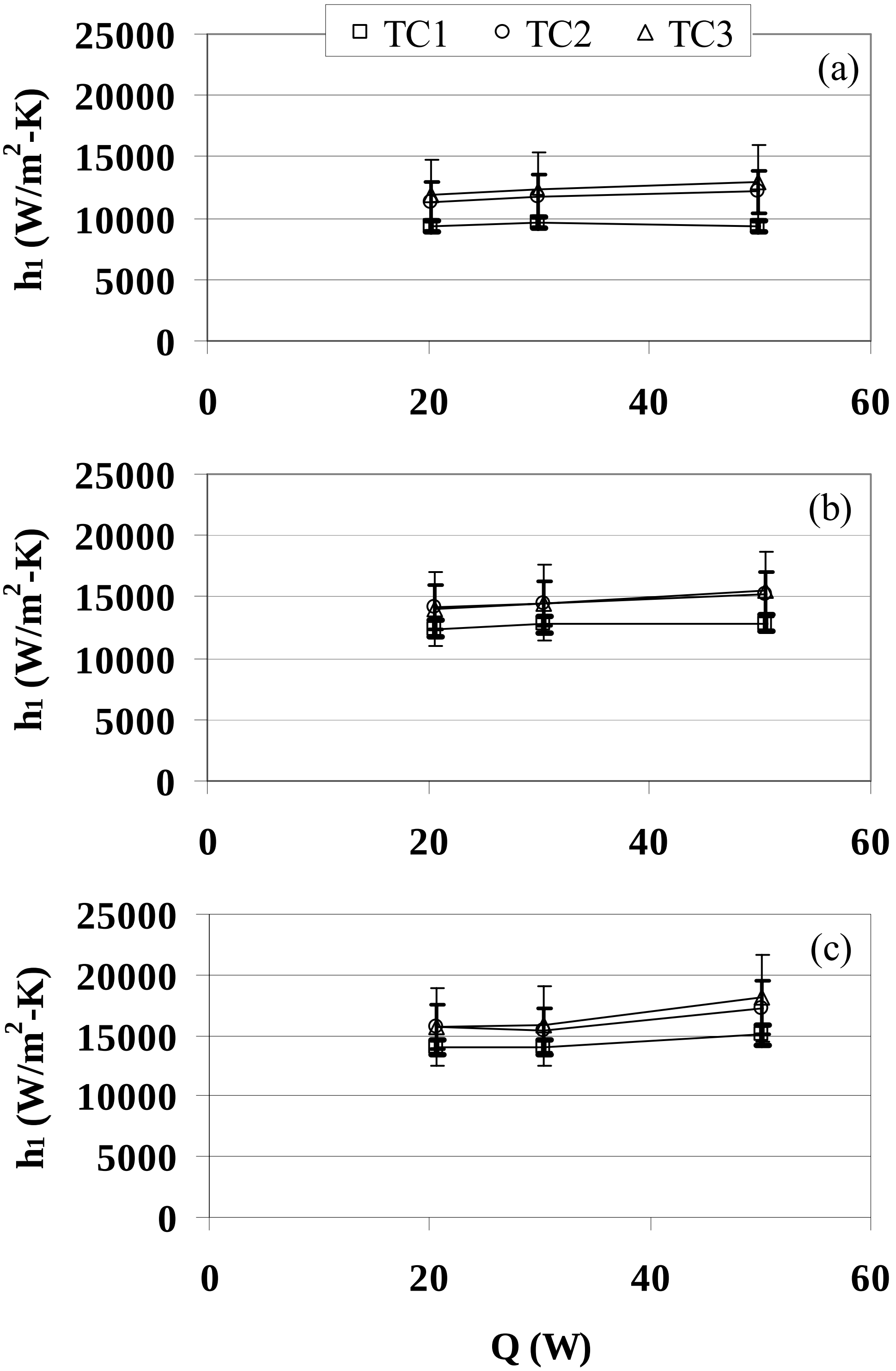

Figure 25: Spray heat transfer coefficient, h_1, versus heater power (upward-facing heater) (a) $\dot{V} = 5.0$ gal/hr; (b) $\dot{V} = 8.0$ gal/hr; (c) $\dot{V} = 10.0$ gal/hr.

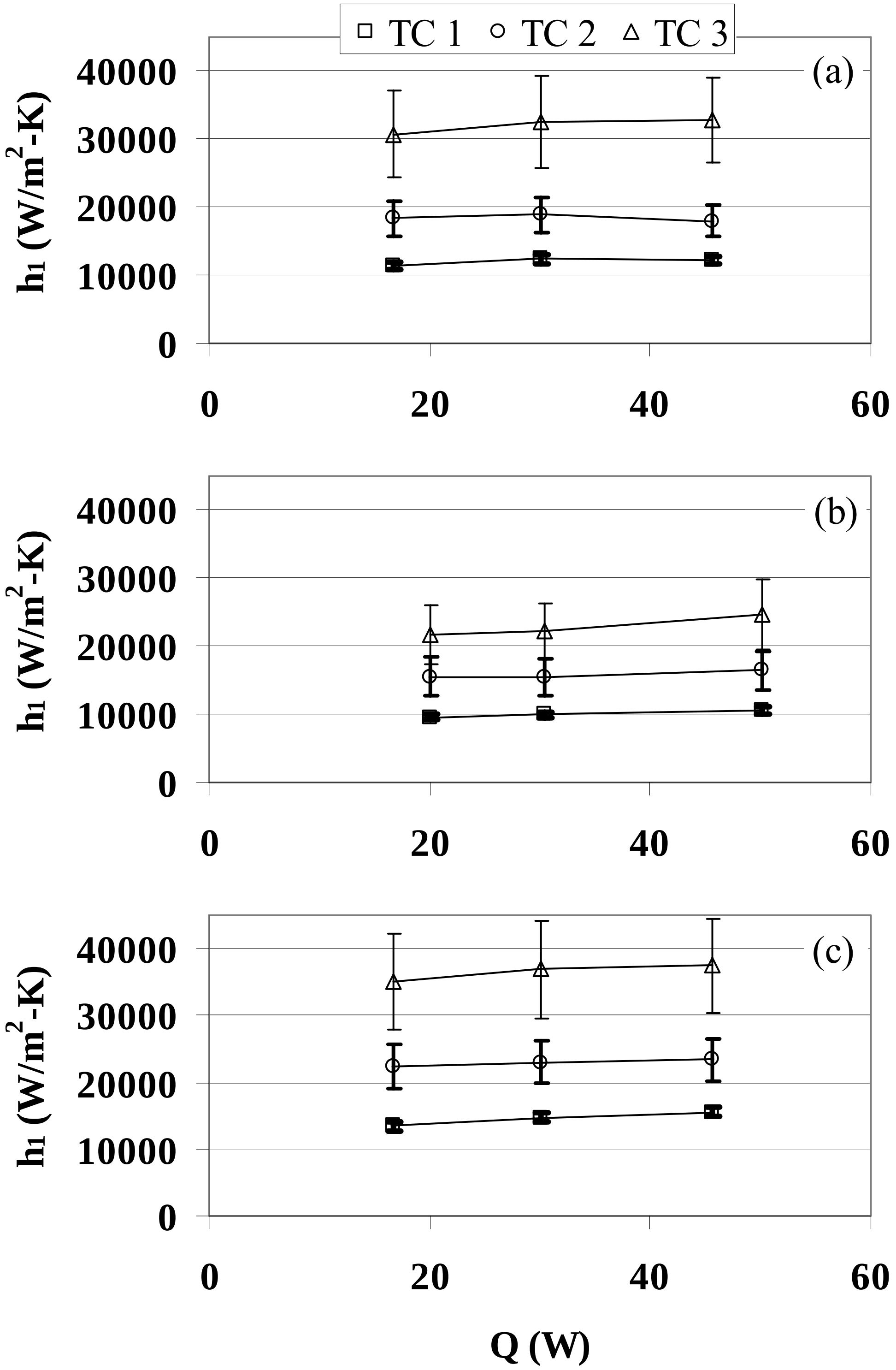

Figure 26: Spray heat transfer coefficient, h_1, versus heater power (downward-facing heater) (a) $\dot{V} = 4.0$ gal/hr; (b) $\dot{V} = 5.0$ gal/hr; (c) $\dot{V} = 6.0$ gal/hr.

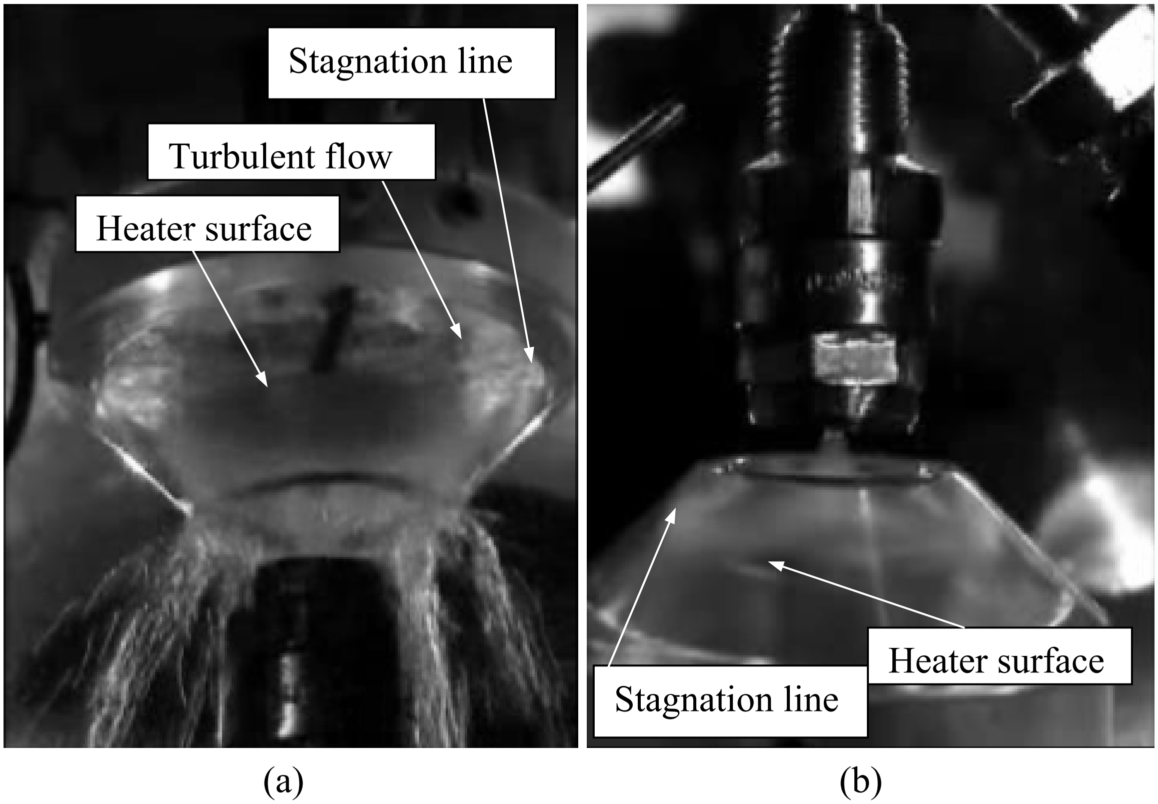

(a) (b)

Figure 27: Behavior of the sprayed fluid: (a) Downward-facing heater; (b) Upward-facing heater.

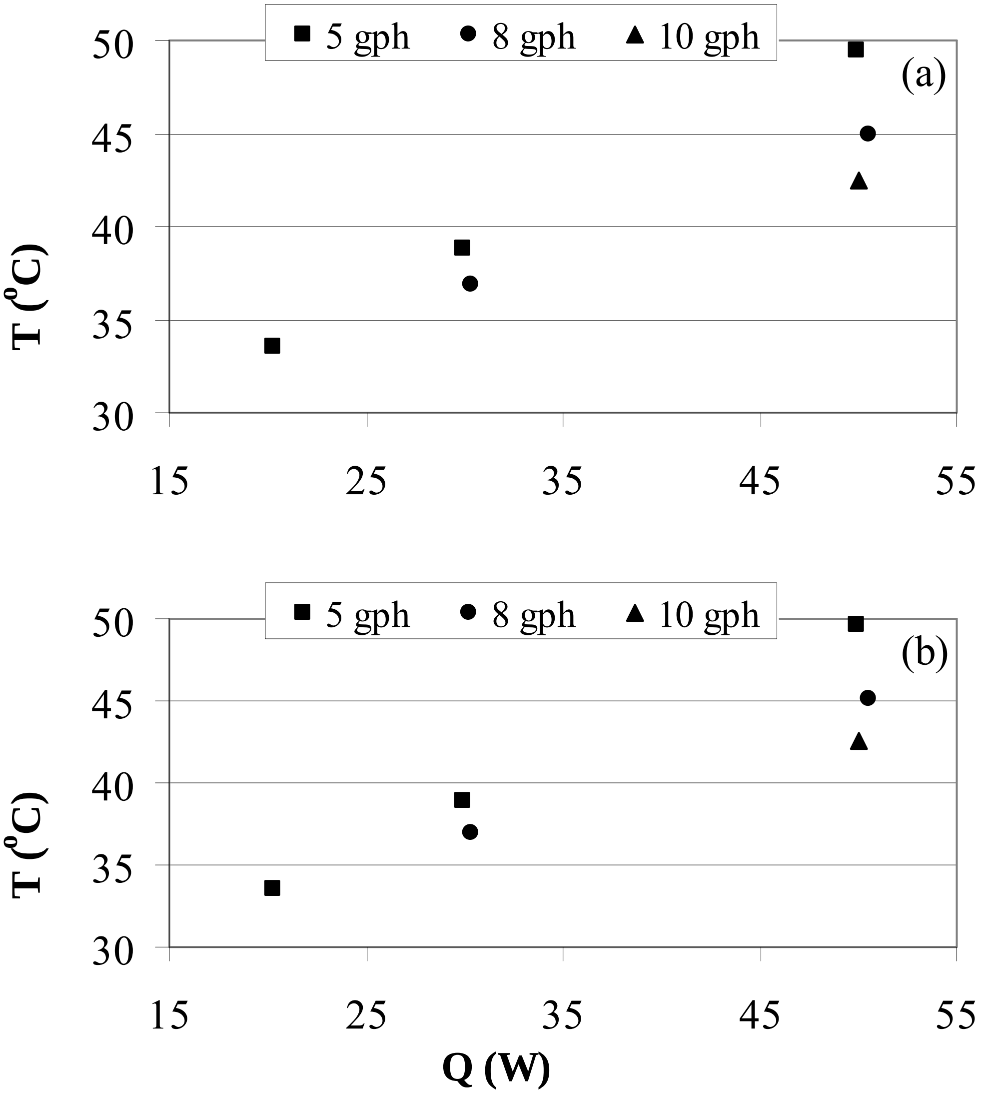

Figure 28: Temperature versus power (a) Average surface temperature; (b) Surface temperature directly above thermocouple 1 (upward-facing heater).

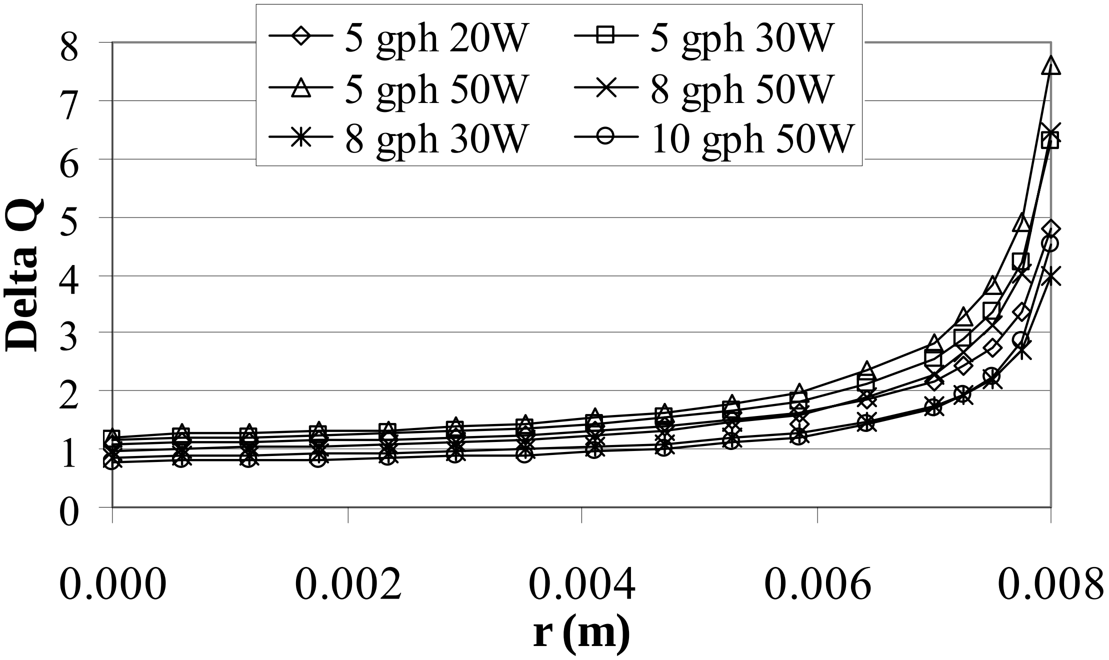

Figure 29: Local heat lost due to conduction within the upward-facing glass pedestal heater assembly versus radial location.

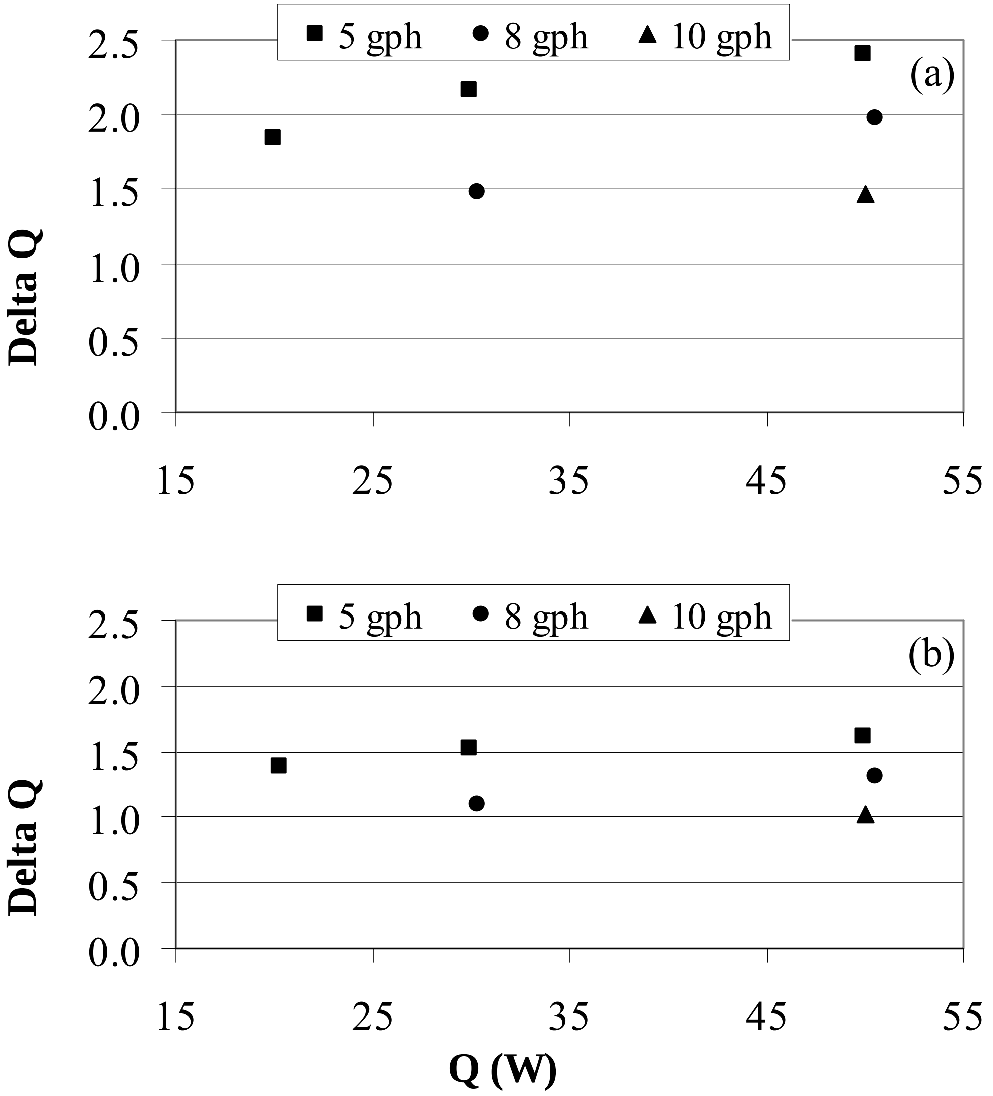

Figure 30: Heat lost due to conduction in the upward-facing glass heater pedestal assembly versus power: (a) Based on average surface temperature; (b) Based on surface temperature directly above thermocouple 1.

VI. Conclusions

Baseline tests were performed for a spray cooling system using subcooled fluid under terrestrial gravity conditions. A preliminary numerical study was done to ensure that the finite element software would provide a reliable approximation of the experimental setup. A steady state numerical model of the glass heater pedestal assembly was then built and tested using the finite element software. The spray heat transfer coefficient along the top of the heated surface was estimated for several volumetric flow rates, heat transfer rates, and heater orientations with respect to gravity. Several key observations were made:

- The spray heat transfer coefficient, h_1, was a weak function of heat input, Q_h, but varied significantly with volumetric flow rate, $\dot{V}$.
- The temperature at thermocouple 1 (TC1) was not significantly affected by h_2, making it the best predictor of h_1.
- Temperatures within the heated pedestal remained below the saturation temperature, T_{sat}, in the spray chamber, indicating that the assumption of subcooled fluid was appropriate for the given conditions.
- For a volumetric flow range of $4.0 \le \dot{V} \le 10.0$ gal/hr and power range of $0.0 \le Q \le 50.0$ W, h_1 was estimated to be on the order of $10{,}000 \le h_1 \le 15{,}000$ W/(m^2-K) for both the upward- and downward-facing heaters.
- Local heat conduction into the upward-facing heater pedestal assembly was fairly constant for $\frac{r}{R_p} \le 0.5$, and was found to be $1.0 \le \Delta Q \le 2.5\%$.

Appendix A: Additional Figures

This appendix contains a complete list of the figures used to determine the values presented in the main body of the thesis.

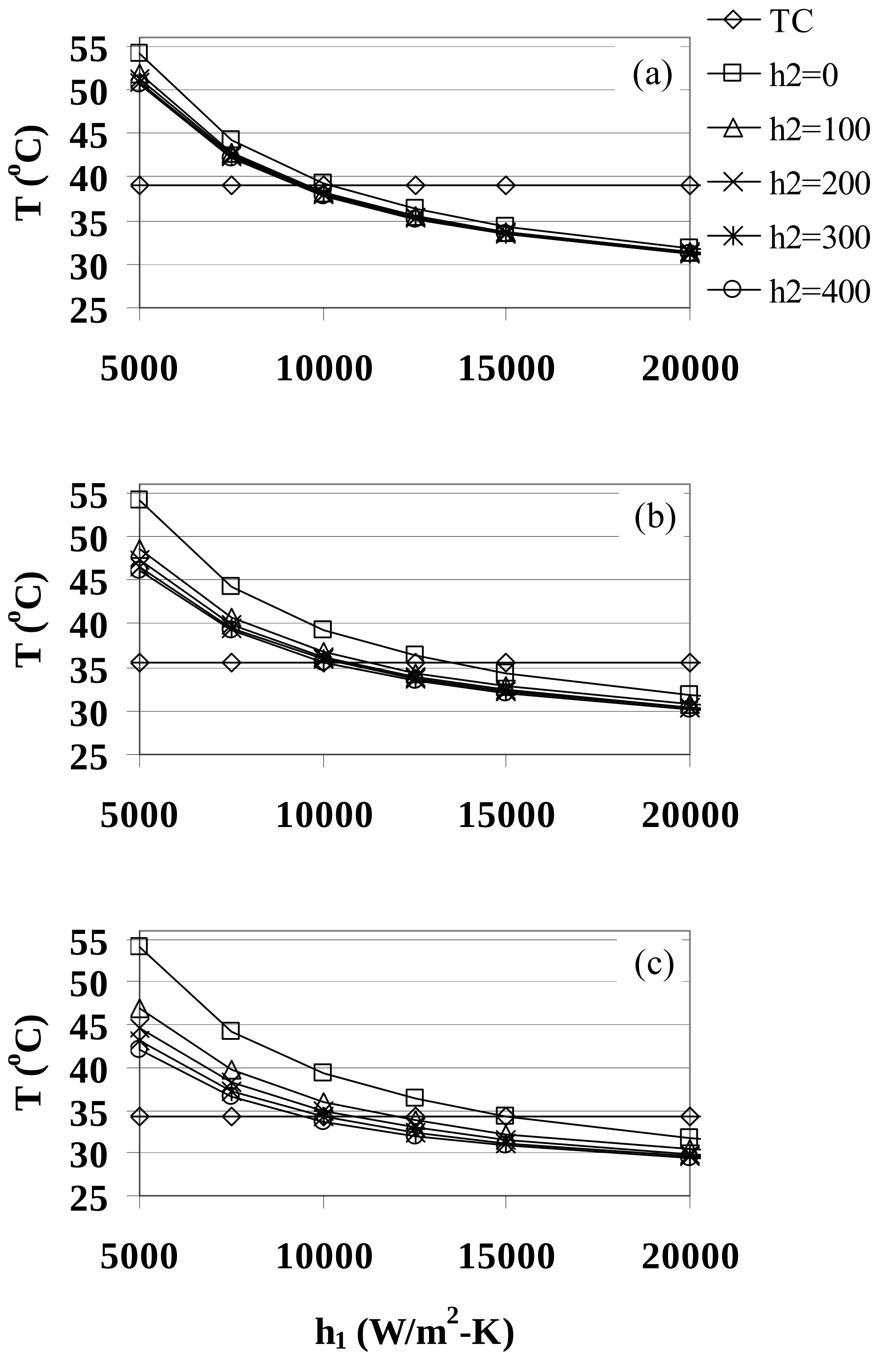

Figure 31: Thermocouple temperatures within the upward-facing glass heater pedestal assembly versus spray heat transfer coefficient: ($\dot{V}$ = 5.0 gal/hr, Q = 30 W): (a) Thermocouple 1; (b) Thermocouple 2; (c) Thermocouple 3.

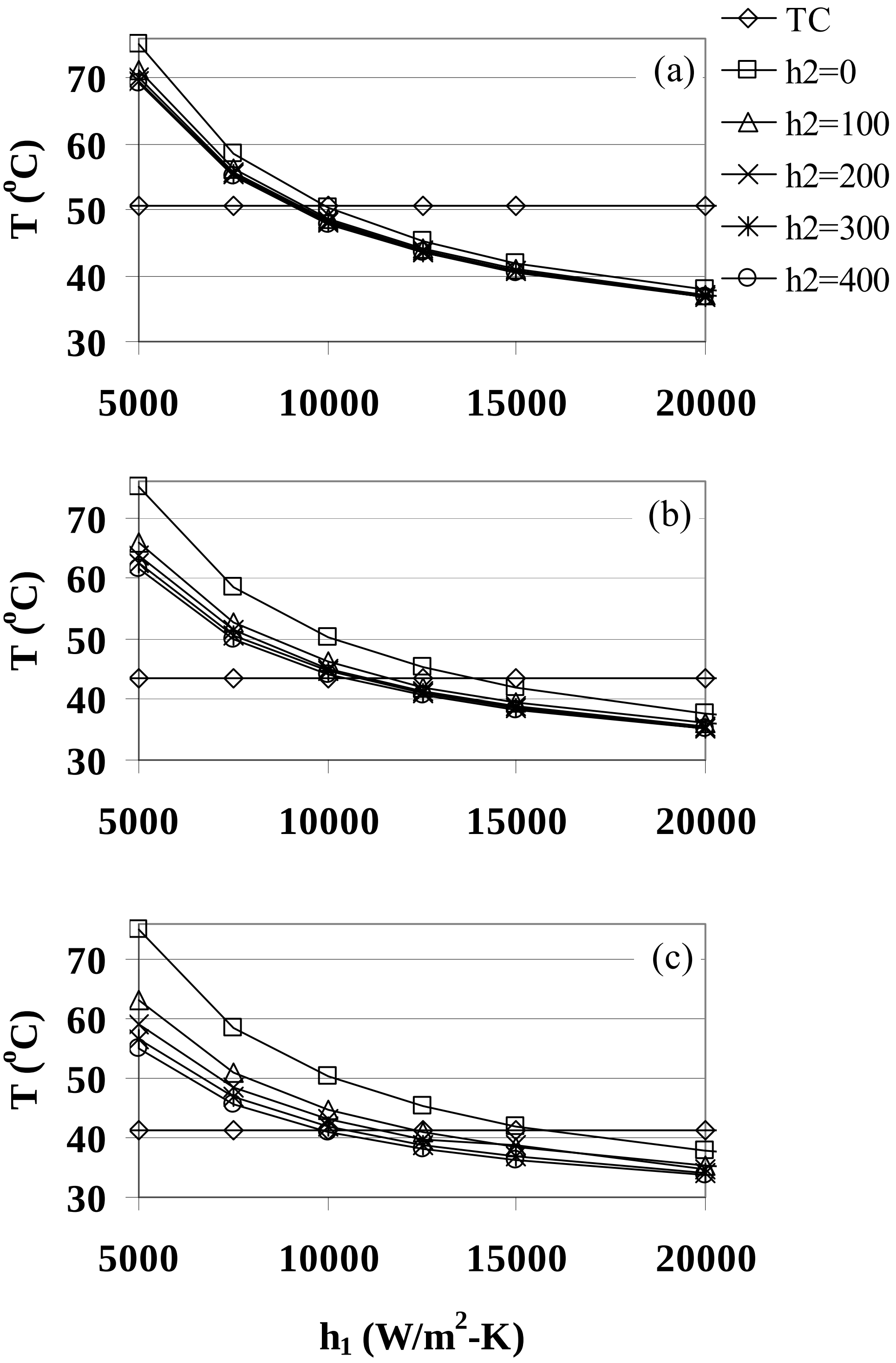

Figure 32: Thermocouple temperatures within the upward-facing glass heater pedestal assembly versus spray heat transfer coefficient ($\dot{V} = 5.0\,\text{gal/hr}$, Q = 50 W): (a) Thermocouple 1; (b) Thermocouple 2; (c) Thermocouple 3.

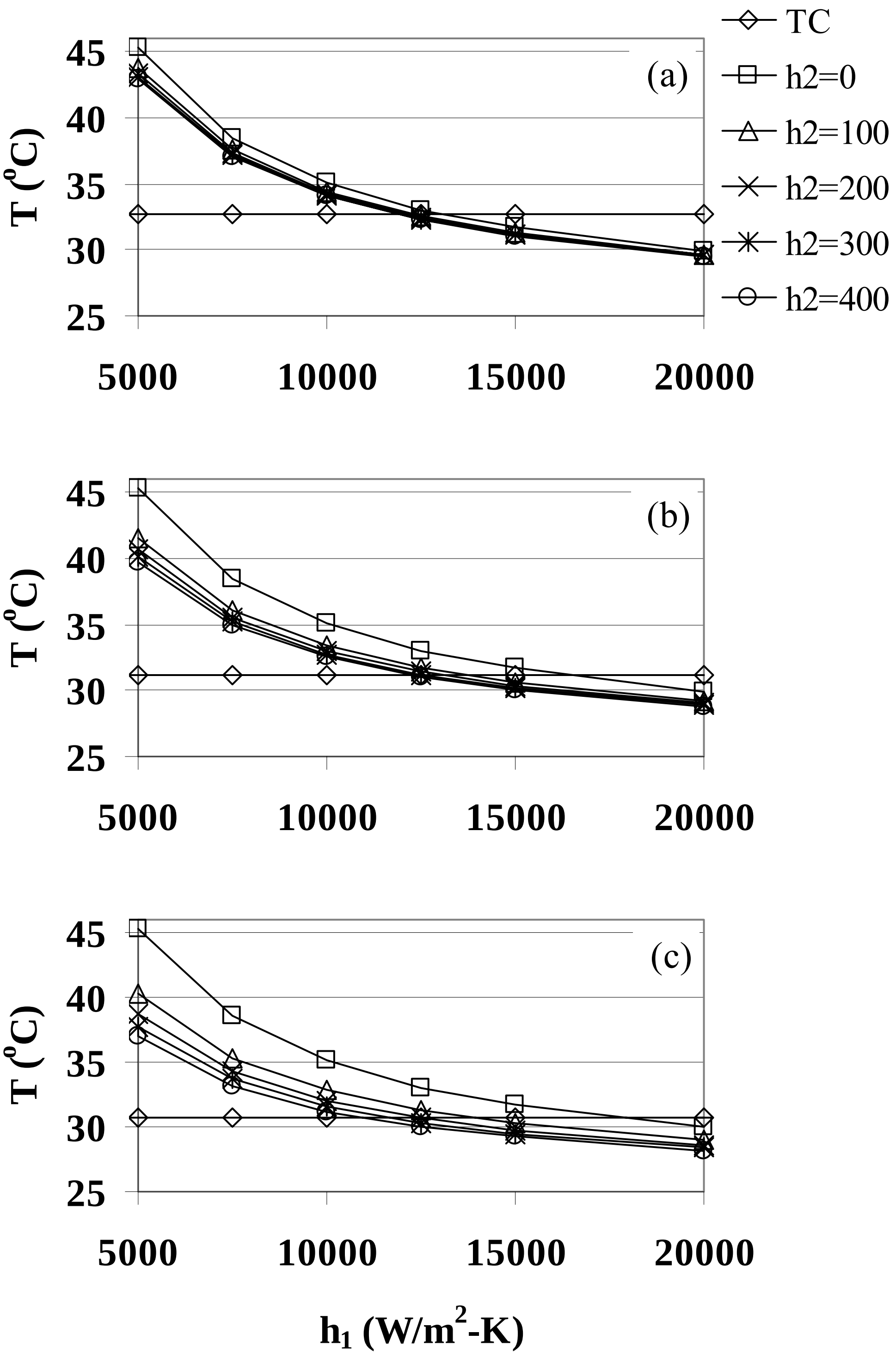

Figure 33: Thermocouple temperatures within the upward-facing glass heater pedestal assembly versus spray heat transfer coefficient ($\dot{V} = 8.0$ gal/hr, Q = 20 W): (a) Thermocouple 1; (b) Thermocouple 2; (c) Thermocouple 3.

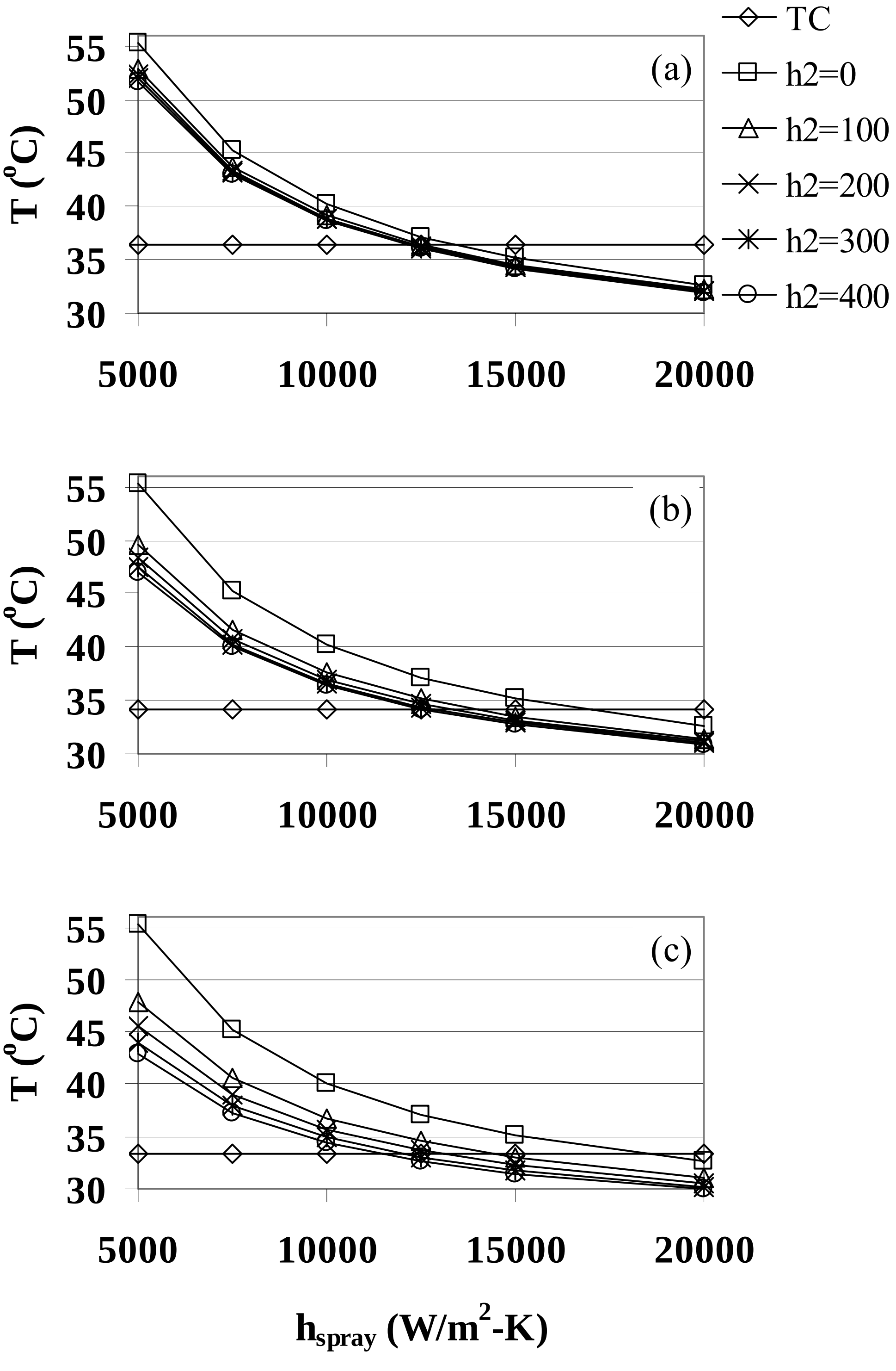

Figure 34: Thermocouple temperatures within the upward-facing glass heater pedestal assembly versus spray heat transfer coefficient ($\dot{V} = 8.0\,\text{gal/hr}$, Q = 30 W): (a) Thermocouple 1; (b) Thermocouple 2; (c) Thermocouple 3.

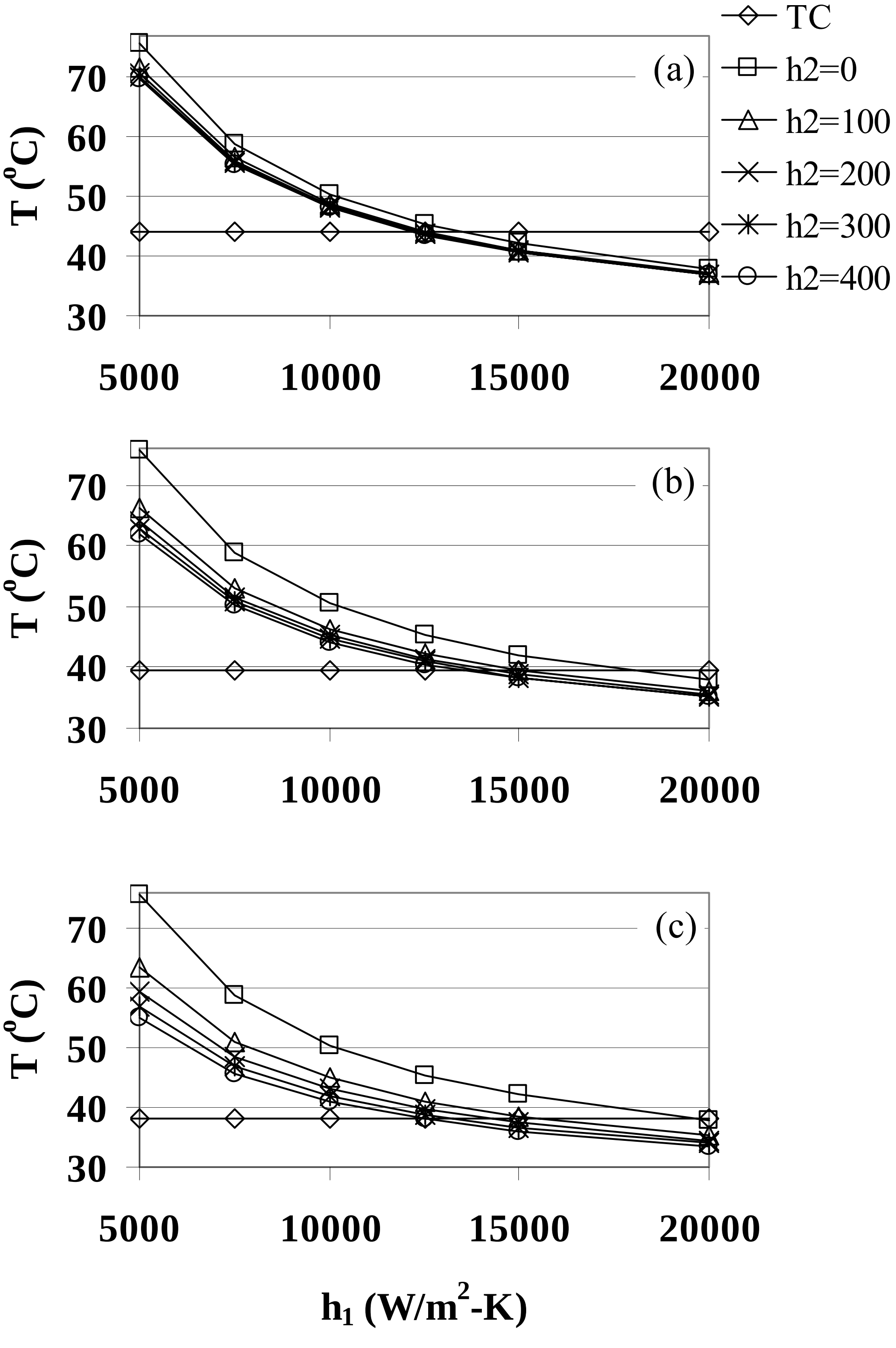

Figure 35: Thermocouple temperatures within the upward-facing glass heater pedestal assembly versus spray heat transfer coefficient ($\dot{V} = 8.0\,\text{gal/hr}$, Q = 50 W): (a) Thermocouple 1; (b) Thermocouple 2; (c) Thermocouple 3.

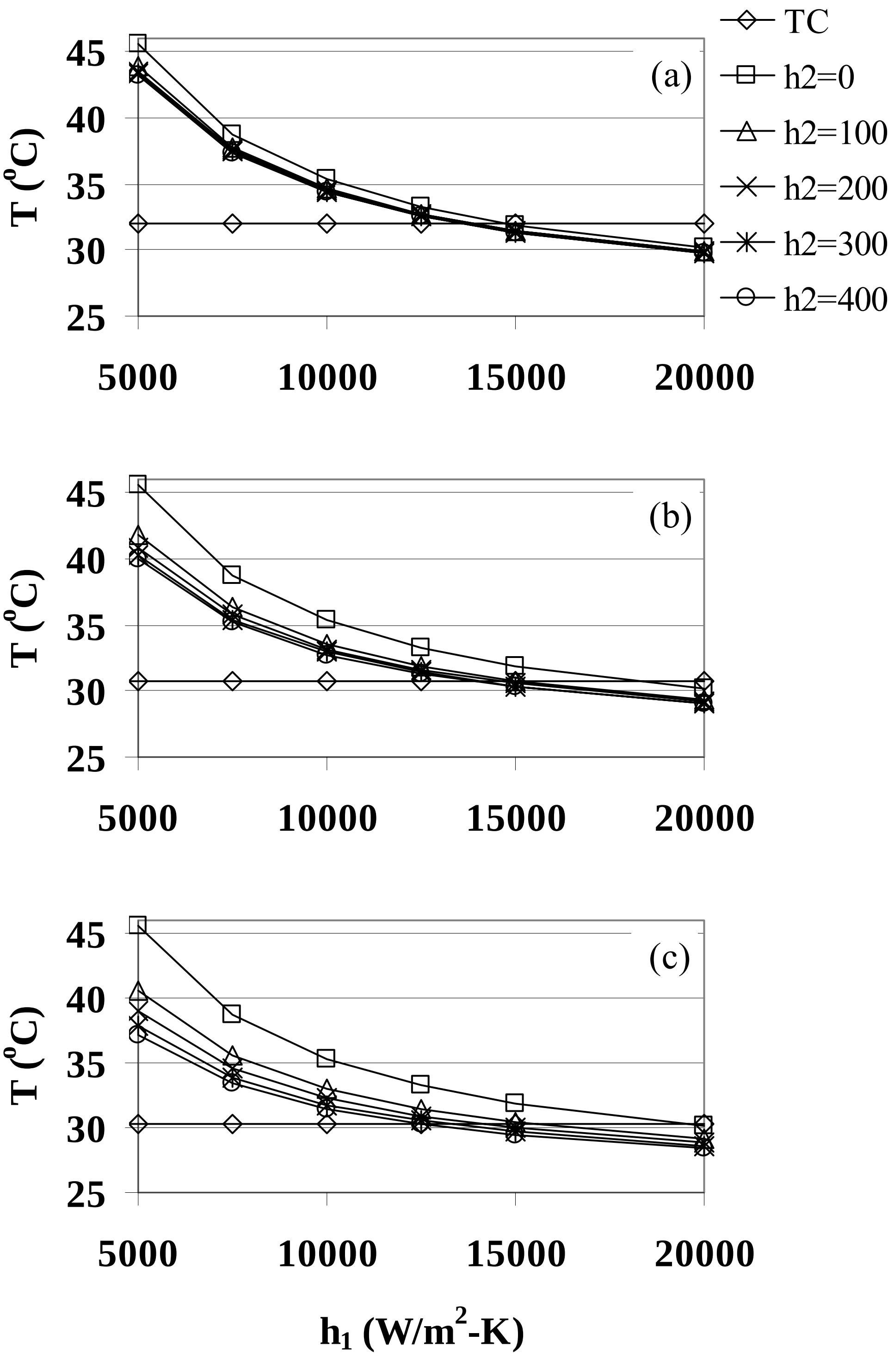

Figure 36: Thermocouple temperatures within the upward-facing glass heater pedestal assembly versus spray heat transfer coefficient ($\dot{V} = 10.0$ gal/hr, Q = 20 W): (a) Thermocouple 1; (b) Thermocouple 2; (c) Thermocouple 3.

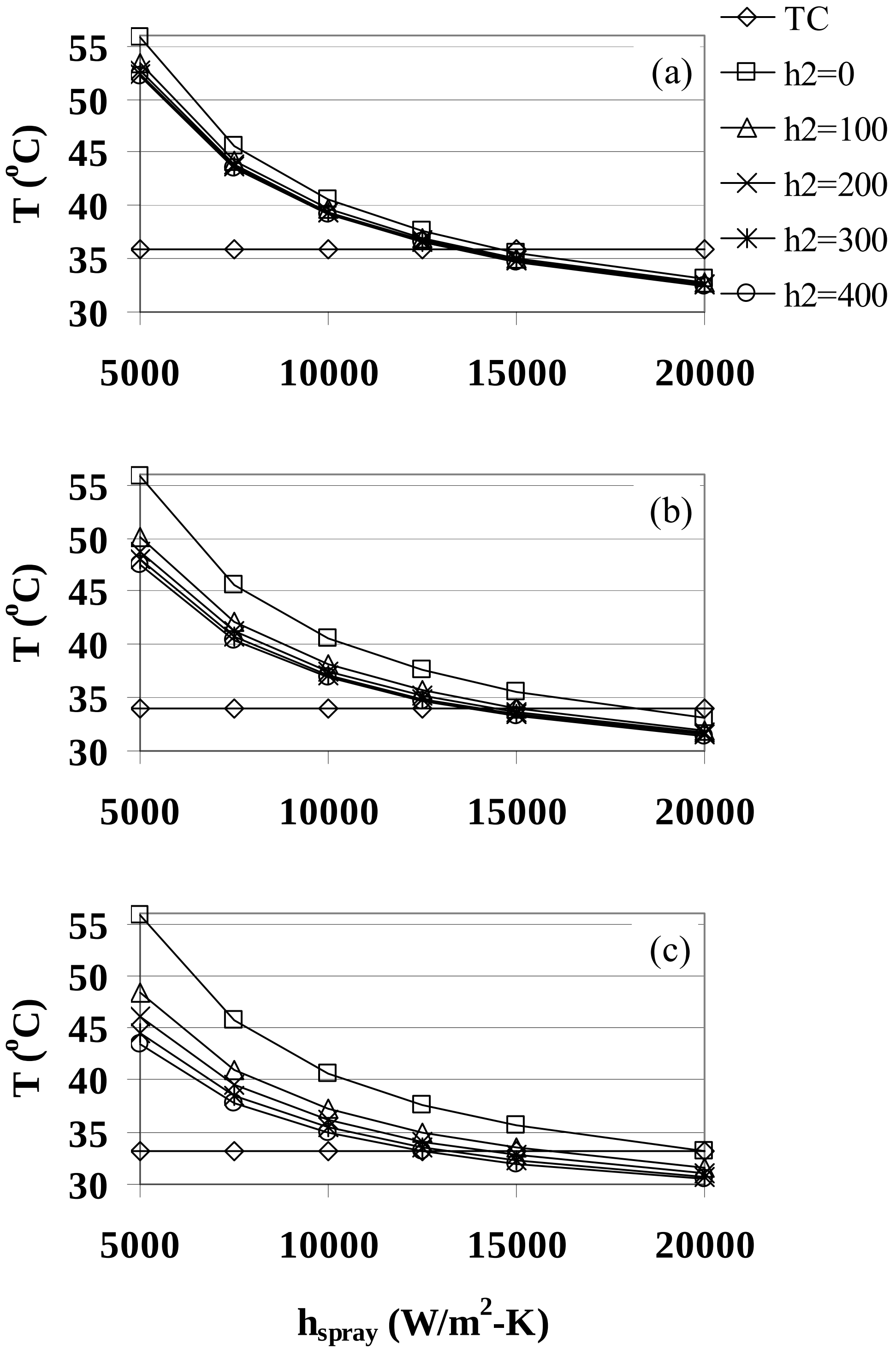

Figure 37: Thermocouple temperatures within the upward-facing glass heater pedestal assembly versus spray heat transfer coefficient ($\dot{V} = 10.0$ gal/hr, Q = 30 W): (a) Thermocouple 1; (b) Thermocouple 2; (c) Thermocouple 3.

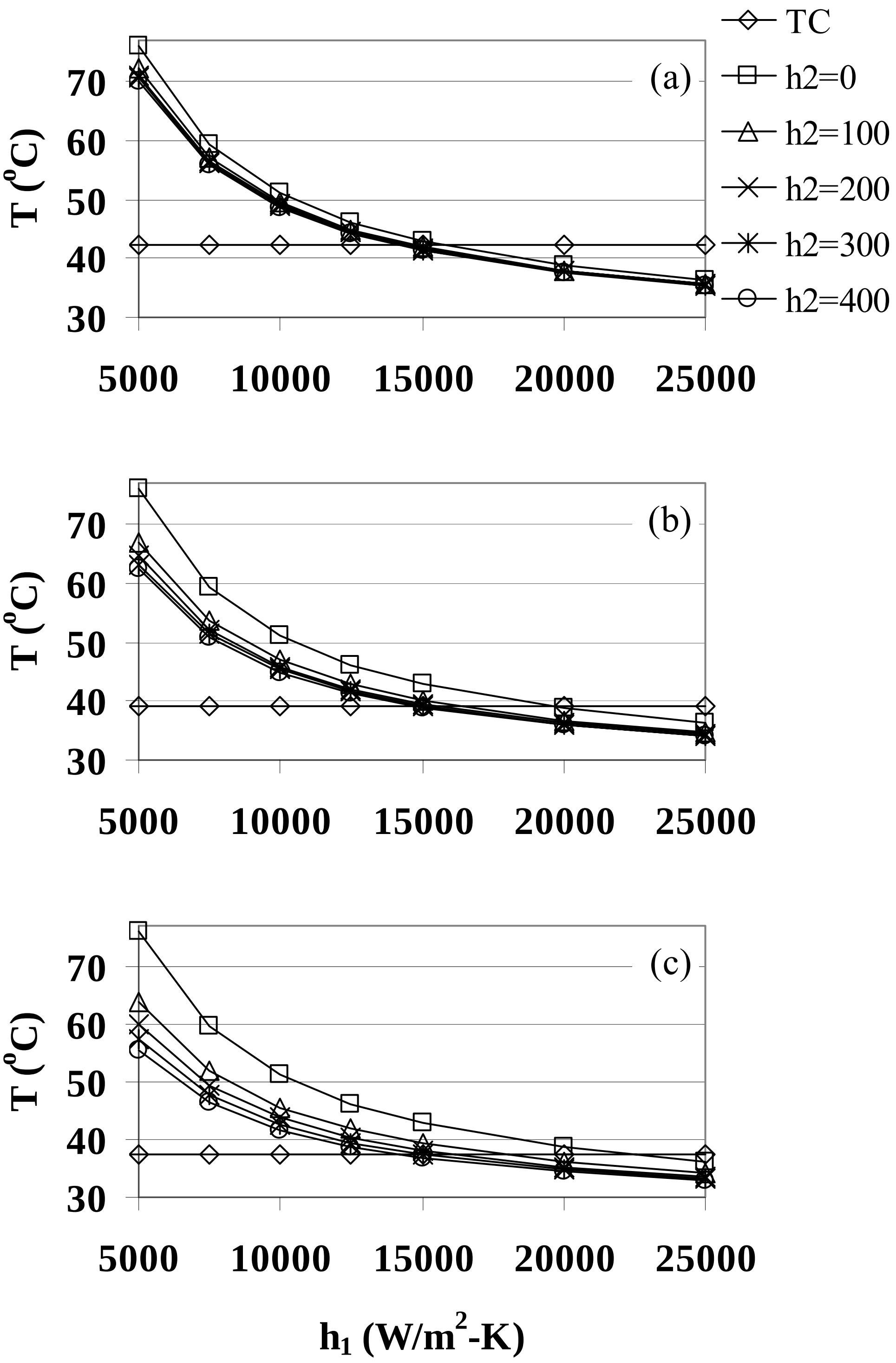

Figure 38: Thermocouple temperatures within the upward-facing glass heater pedestal assembly versus spray heat transfer coefficient ($\dot{V} = 10.0\,\text{gal/hr}$, Q = 50 W): (a) Thermocouple 1; (b) Thermocouple 2; (c) Thermocouple 3.

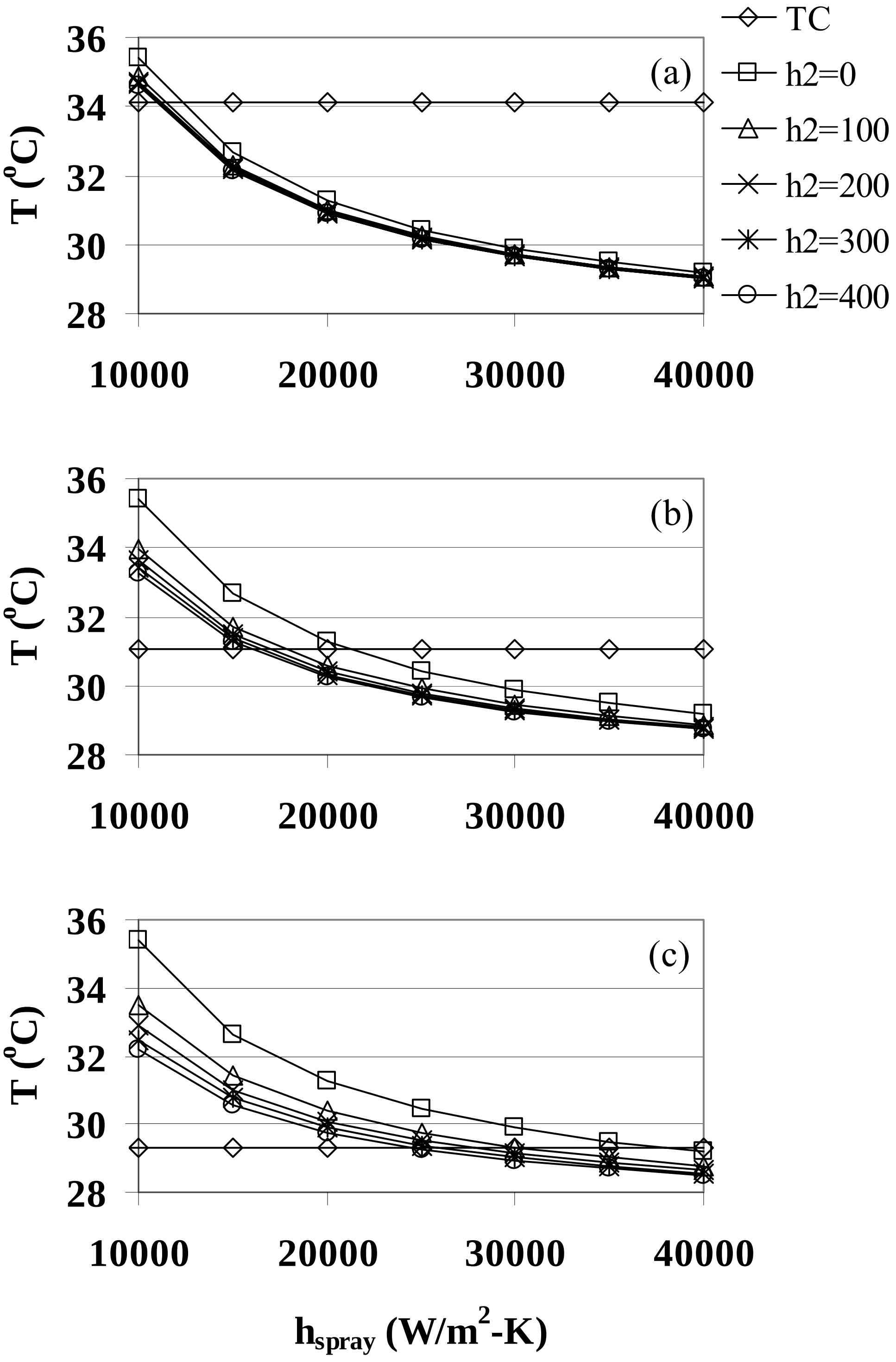

Figure 39: Thermocouple temperatures within the downward-facing glass heater pedestal assembly versus spray heat transfer coefficient ($\dot{V} = 4.0$ gal/hr, Q = 16 W): (a) Thermocouple 1; (b) Thermocouple 2; (c) Thermocouple 3.

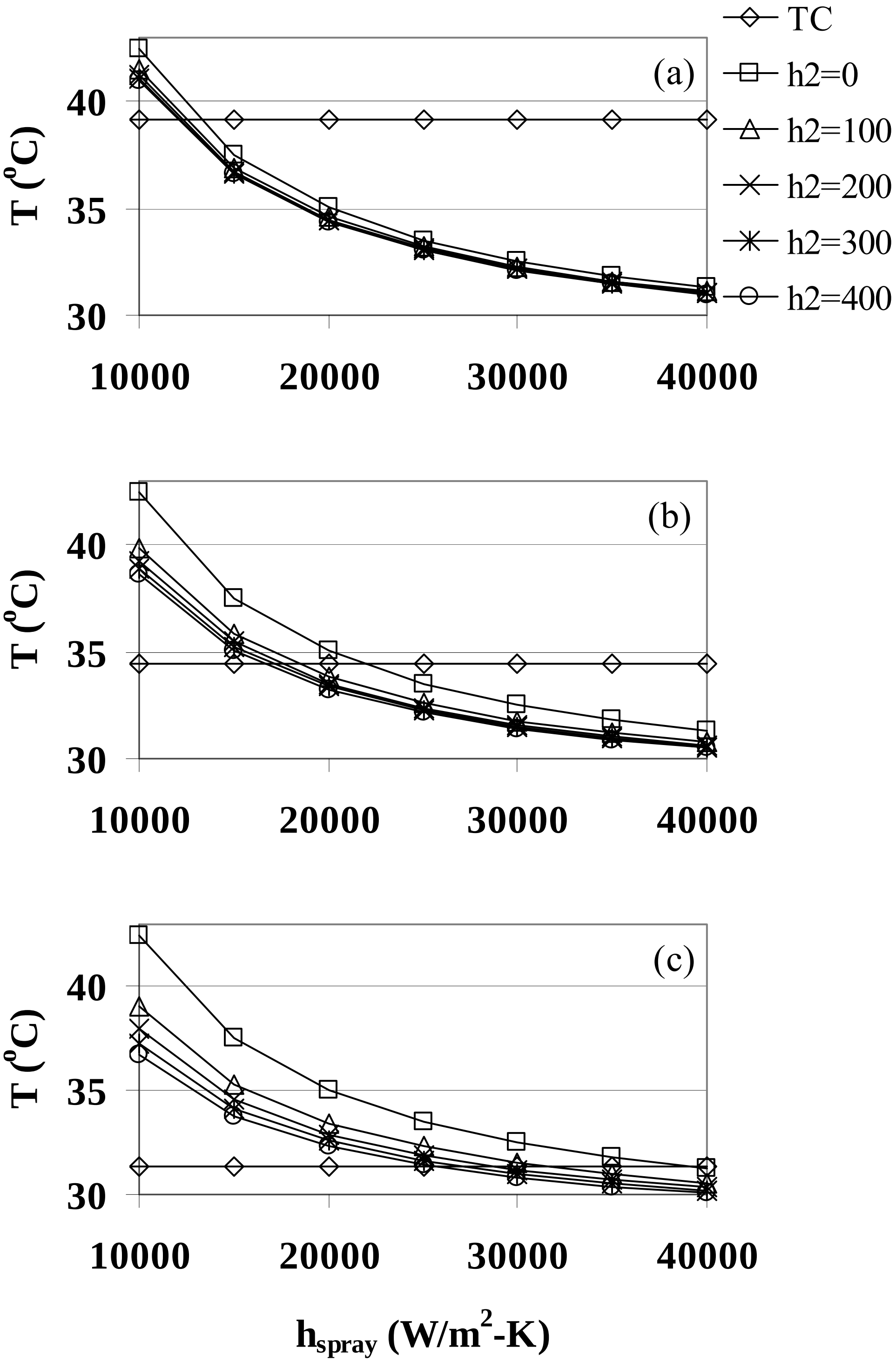

Figure 40: Thermocouple temperatures within the downward-facing glass heater pedestal assembly versus spray heat transfer coefficient ($\dot{V} = 4.0$ gal/hr, Q = 30 W): (a) Thermocouple 1; (b) Thermocouple 2; (c) Thermocouple 3.

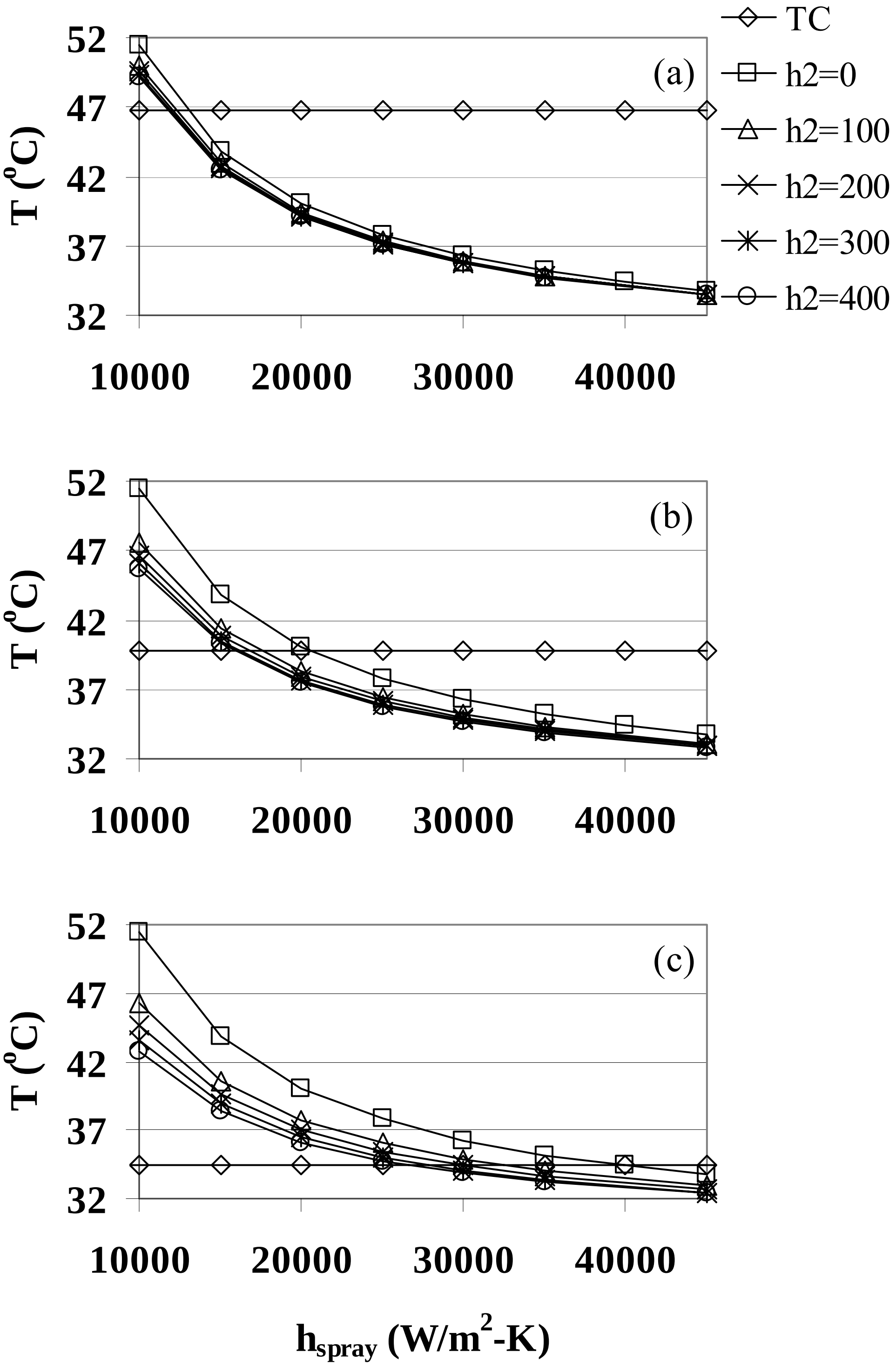

Figure 41: Thermocouple temperatures within the downward-facing glass heater pedestal assembly versus spray heat transfer coefficient ($\dot{V} = 4.0\,\text{gal/hr}$, Q = 45 W): (a) Thermocouple 1; (b) Thermocouple 2; (c) Thermocouple 3.

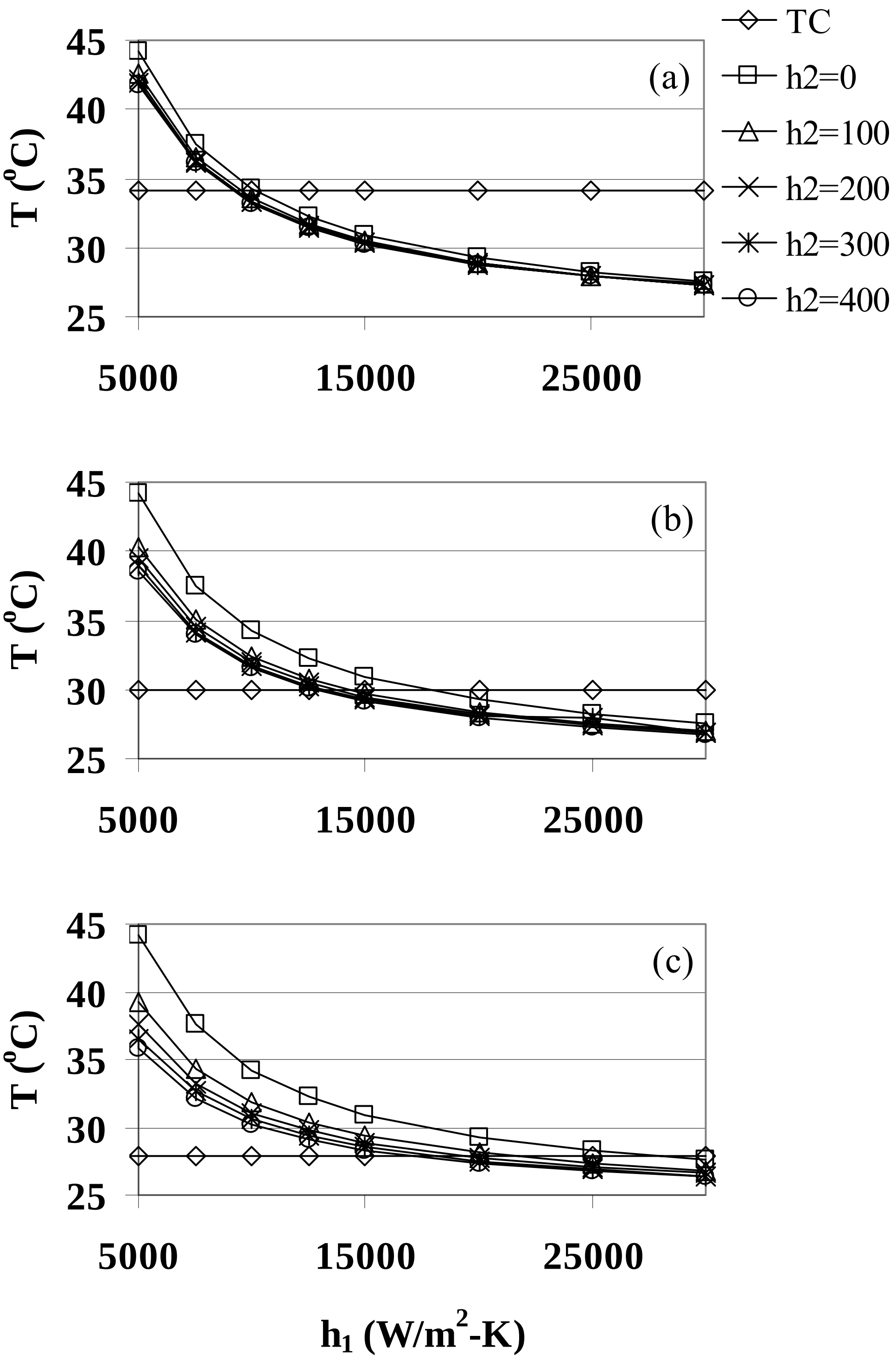

Figure 42: Thermocouple temperatures within the downward-facing glass heater pedestal assembly versus spray heat transfer coefficient ($\dot{V} = 5.0$ gal/hr, Q = 20 W): (a) Thermocouple 1; (b) Thermocouple 2; (c) Thermocouple 3.

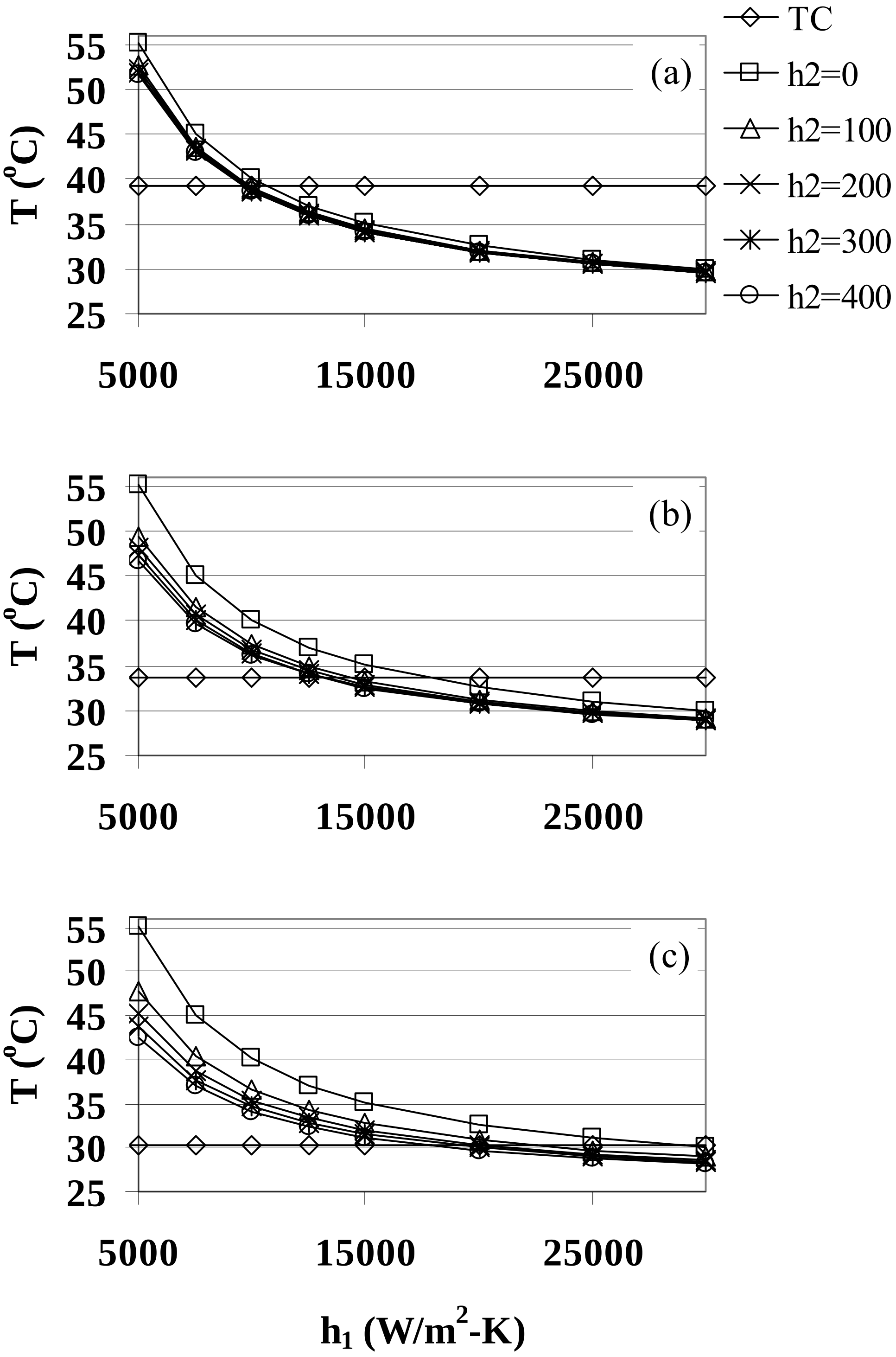

Figure 43: Thermocouple temperatures within the downward-facing glass heater pedestal assembly versus spray heat transfer coefficient ($\dot{V} = 5.0$ gal/hr, Q = 30 W): (a) Thermocouple 1; (b) Thermocouple 2; (c) Thermocouple 3.

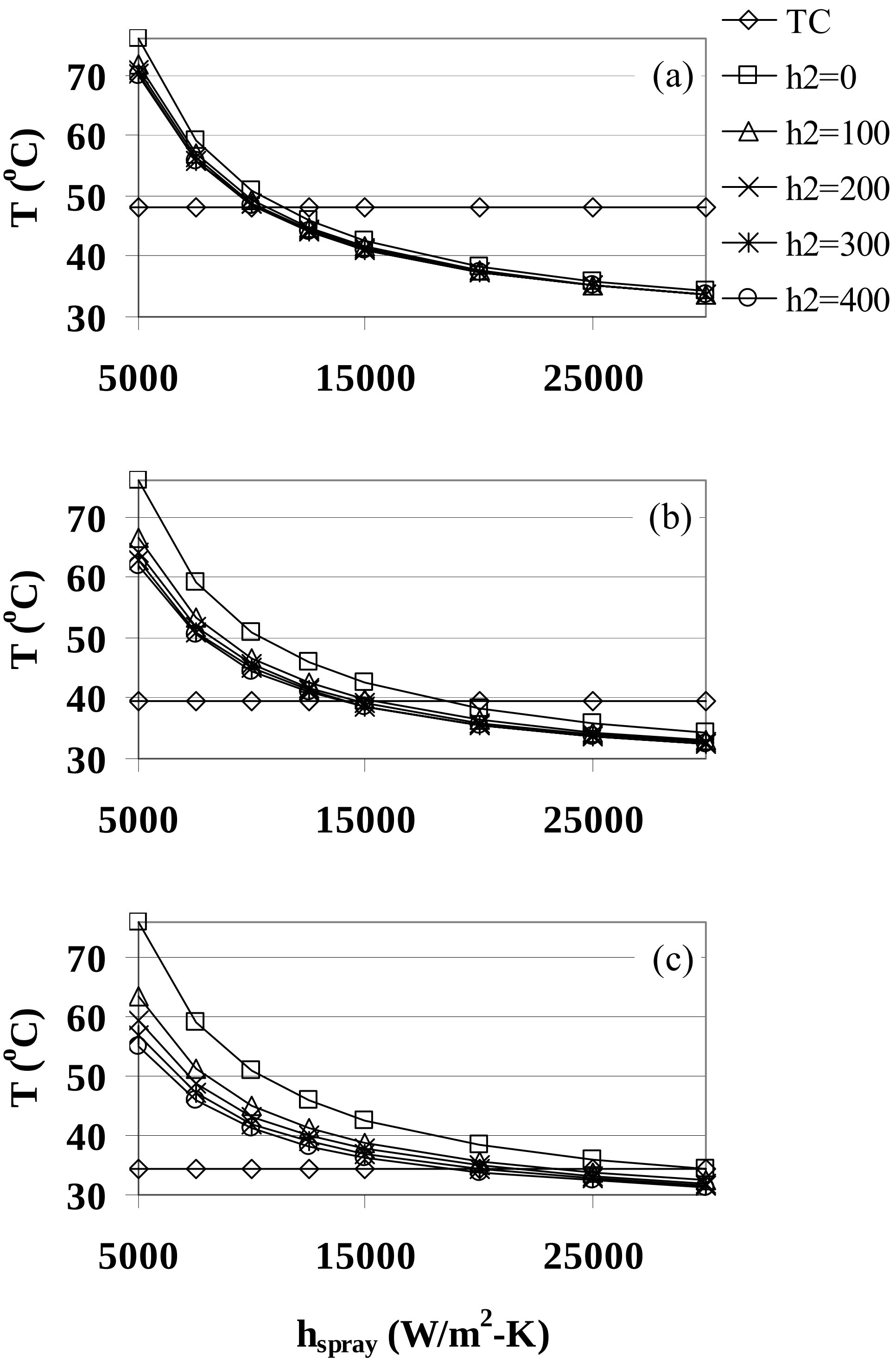

Figure 44: Thermocouple temperatures within the downward-facing glass heater pedestal assembly versus spray heat transfer coefficient ($\dot{V} = 5.0\,\text{gal/hr}$, Q = 50 W): (a) Thermocouple 1; (b) Thermocouple 2; (c) Thermocouple 3.

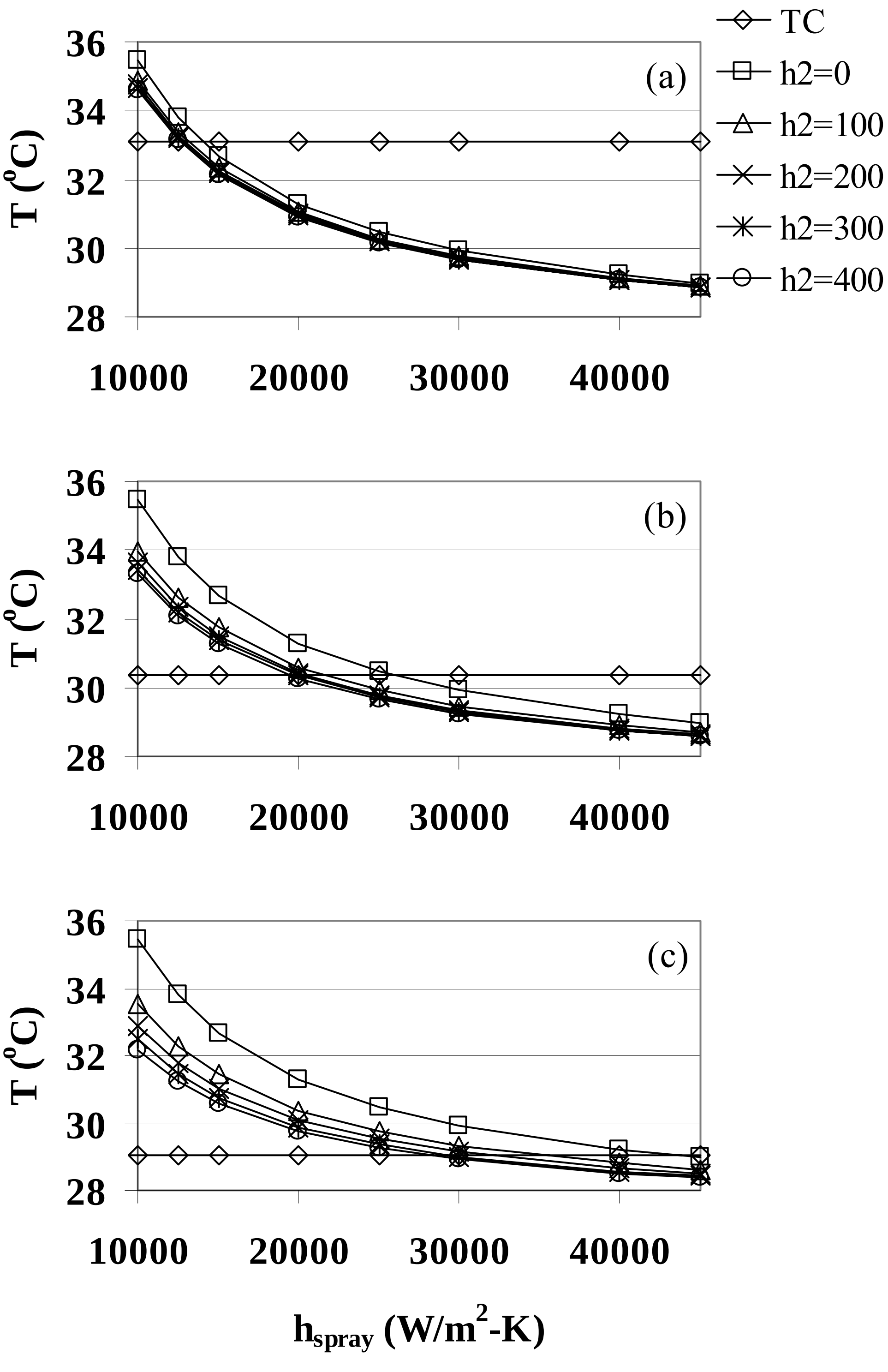

Figure 45: Thermocouple temperatures within the downward-facing glass heater pedestal assembly versus spray heat transfer coefficient ($\dot{V} = 6.0$ gal/hr, Q = 16 W): (a) Thermocouple 1; (b) Thermocouple 2; (c) Thermocouple 3.

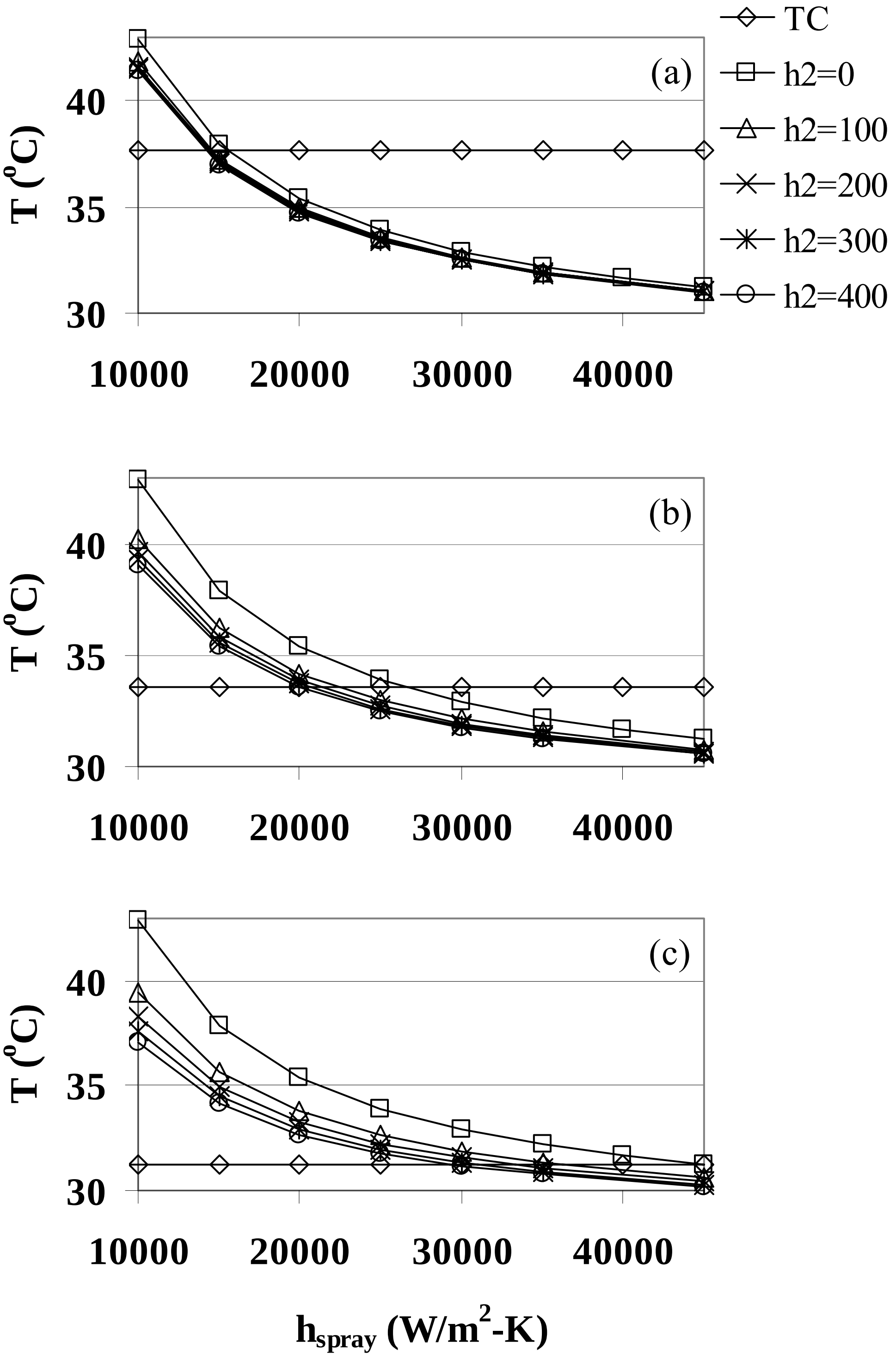

Figure 46: Thermocouple temperatures within the downward-facing glass heater pedestal assembly versus spray heat transfer coefficient ($\dot{V} = 6.0$ gal/hr, Q = 30 W): (a) Thermocouple 1; (b) Thermocouple 2; (c) Thermocouple 3.

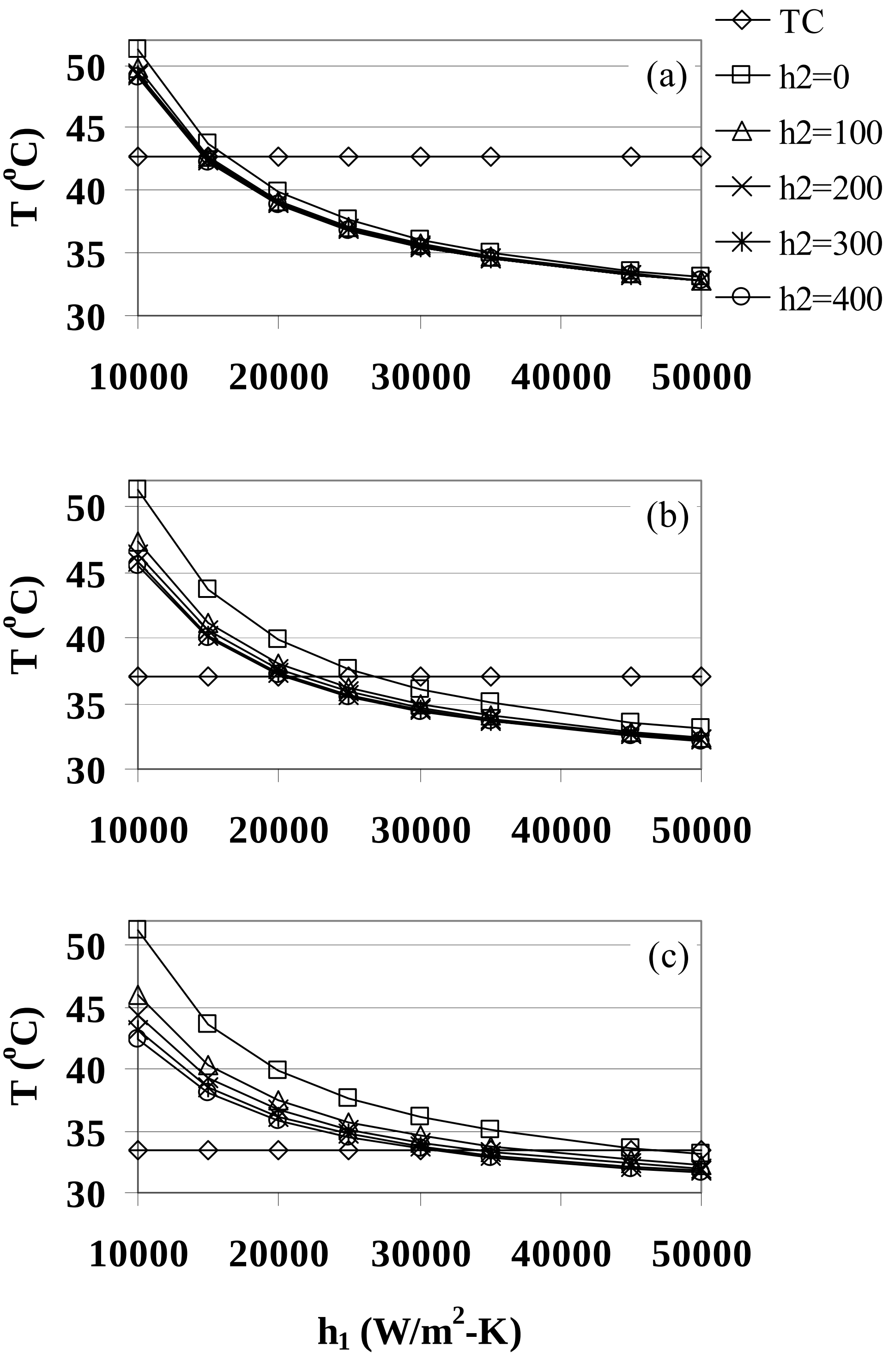

Figure 47: Thermocouple temperatures within the downward-facing glass heater pedestal assembly versus spray heat transfer coefficient ($\dot{V} = 6.0$ gal/hr, Q = 45 W): (a) Thermocouple 1; (b) Thermocouple 2; (c) Thermocouple 3.

Appendix B: Supplemental Materials

This appendix contains a listing of the MATLAB code used in the preliminary analysis of a right circular cylinder, as well as ANSYS log and output files of input and output used to build the numerical model of the glass heater pedestal assembly.

MATLAB Program Code

```
%%Function to find Temp1 for ME890

function Temp1 = Temp1

format long
B=1;
R=B;                                    %Radial Dimension
Xel=10;                                 %Number elements in x-direction
Zel=10;                                 %Number elements in z-direction
Xnodes=Xel+1;                           %Number nodes in x-direction
Znodes=Zel+1;                           %Number nodes in z-direction
Xinc=R/Xel;
Zinc=1/Zel;

%%Initialize Temp2 matrix
Temp1=zeros(Znodes+2,Xnodes+2);

%%Set nodes and position labels
for p=3:Xnodes+2
    Temp1(1,p)=p-2;
    Temp1(2,p)=(p-3)*Xinc;
end

for q=3:Znodes+2
    Temp1(q,1)=q-2;
    Temp1(q,2)=(q-3)*Zinc;
end

%%Initialize increment matrix
IncMat=zeros(Znodes+2,Xnodes+2);

%%Set nodes and position labels
for p=3:Xnodes+2
    IncMat(1,p)=p-2;
    IncMat(2,p)=(p-3)*Xinc;
end

for q=3:Znodes+2
    IncMat(q,1)=q-2;
    IncMat(q,2)=(q-3)*Zinc;
end

%%Get T1 at each node
for n=3:Znodes+2
    z=Temp1(n,2);

    for m=3:Xnodes+2
        r=Temp1(2,m);

    a=1;
    b=1;
    moveon=0;
    epsilon=1e-6;
```

```
    t=5;
    while moveon==0
                    sumold=0;
                    oldroot=0;

                    for i=1:a
                        root=besselroot(oldroot);
                        beta=root/B;

                        for j=1:b
                            eta=((2*j)-1)*(pi/2);

                            c=((1/eta)+(((-1)^j)
                        /(beta^2+eta^2)))/(beta*besselj(1,(beta*B)));

                            quantity=(c*besselj(0,(beta*r))*sin(eta*z)
                                     *exp(-(beta^2+eta^2)*t));

                            sumnew=sumold+quantity;

                            diff=abs(sumnew-sumold);
                            sumold=sumnew;
                            oldroot=root;
                        end
                    end

                    if diff<epsilon
                        moveon=1;
                    else
                        a=a+1;
                        b=b+1;
                    end
                end

                IncMat(n,m)=a;
                Temp1(n,m)=sumnew*4/B;
                a;
                b;

    if Temp1(n,m)<1e-16
        Temp1(n,m)=0;
    end

end
end
Temp1;
IncMat(n,m);
```

```
%Function to find Temp2 for ME890

function Temp2 = Temp2

format long
B=1;
R=B;                                    %Radial Dimension
Xel=10;                                 %Number elements in x-direction
Zel=10;                                 %Number elements in z-direction
Xnodes=Xel+1;                           %Number nodes in x-direction
Znodes=Zel+1;                           %Number nodes in z-direction
Xinc=R/Xel;
Zinc=1/Zel;

%Initialize Temp2 matrix
Temp2=zeros(Znodes+2,Xnodes+2);

%Set nodes and position labels
for p=3:Xnodes+2
    Temp2(1,p)=p-2;
    Temp2(2,p)=(p-3)*Xinc;
end

for q=3:Znodes+2
    Temp2(q,1)=q-2;
    Temp2(q,2)=(q-3)*Zinc;
end

%Initialize increment matrix
IncMat=zeros(Znodes+2,Xnodes+2);

%Set nodes and position labels
for p=3:Xnodes+2
    IncMat(1,p)=p-2;
    IncMat(2,p)=(p-3)*Xinc;
end

for q=3:Znodes+2
    IncMat(q,1)=q-2;
    IncMat(q,2)=(q-3)*Zinc;
end

%Get T2 at each node
for n=3:Znodes+2
    z=Temp2(n,2);

    for m=3:Xnodes+2
        r=Temp2(2,m);
        epsilon=1e-6;
        moveon=0;
        inc=1;
        sumold=0;
        oldroot=0;

    while moveon==0
          root=besselroot(oldroot);
          beta=root/B;
```

```
          sumnew=sumold+(besselj(0,(beta*r))*sinh(beta*z)
                 /(beta^2*besselj(1,(beta*B))*cosh(beta)));

        diff=abs(sumnew-sumold);

        if diff<epsilon
            moveon=1;
        else
            sumold=sumnew;
            oldroot=root;
            inc=inc+1;
        end
    end

    IncMat(n,m)=inc;
    Temp2(n,m)=(2/B)*sumnew;

    if Temp2(n,m)<1e-10
        Temp2(n,m)=0;
    end

    end
end
Temp2;
beta;
```

ANSYS Log File

```
/BATCH
! /COM,ANSYS RELEASE  5.4    UP19970828         09:47:49    10/29/2004
!*
/FILNAM,StStateGlassModel

!*
/NOPR
/PMETH,OFF
KEYW,PR_SET,1
KEYW,PR_STRUC,0
KEYW,PR_THERM,1
KEYW,PR_FLUID,0
KEYW,PR_ELMAG,0
KEYW,MAGNOD,0
KEYW,MAGEDG,0
KEYW,MAGHFE,0
KEYW,MAGELC,0
KEYW,PR_MULTI,0
/GO
!*
! /COM,
! /COM,Preferences for GUI filtering have been set to display:
! /COM,  Thermal
!*
/PREP7
!*
ET,1,PLANE77
!*
KEYOPT,1,1,0
KEYOPT,1,3,1
!*
!*
UIMP,1,EX, , , ,
UIMP,1,DENS, , , ,
UIMP,1,ALPX, , , ,
UIMP,1,REFT, , , ,
UIMP,1,NUXY, , , ,
UIMP,1,PRXY, , , ,
UIMP,1,GXY, , , ,
UIMP,1,MU, , , ,
UIMP,1,DAMP, , , ,
UIMP,1,KXX, , ,1.04,
UIMP,1,C, , , ,
UIMP,1,ENTH, , , ,
UIMP,1,HF, , , ,
UIMP,1,EMIS, , , ,
UIMP,1,QRATE, , , ,
UIMP,1,MURX, , , ,
UIMP,1,MGXX, , , ,
UIMP,1,RSVX, , , ,
UIMP,1,PERX, , , ,
UIMP,1,VISC, , , ,
UIMP,1,SONC, , , ,
```

```
!*
K,1,0,0,0,
K,2,0,.098,0,
K,3,0,.099,0,
K,4,0,.1,0,
K,5,0,.1005,0,
K,6,0,.100501,0,
K,7,.0047,.100501,0,
K,8,.0047,.1005,0,
K,9,.0047,.1,0,
K,10,.0047,.099,0,
K,11,.0047,.098,0,
K,12,.0047,0,0,
K,13,.007,0,0,
K,14,.007,.098,0,
K,15,.007,.099,0,
K,16,.007,.1,0,
K,17,.007,.1005,0,
K,18,.007,.100501,0,
K,19,.008,.100501,0,
K,20,.008,.1005,0,
K,21,.008,.1,0,
K,22,.008,.099,0,
K,23,.008,.098,0,
K,24,.008,0,0,
! klist,all,,,coord
LSTR,       1,       2
LSTR,       2,       3
LSTR,       3,       4
LSTR,       4,       5
LSTR,       5,       6
! LLIST,ALL, , ,
LSTR,      12,      11
LSTR,      11,      10
LSTR,      10,       9
LSTR,       9,       8
LSTR,       8,       7
! LLIST,ALL, , ,
LSTR,      13,      14
LSTR,      14,      15
LSTR,      15,      16
LSTR,      16,      17
LSTR,      17,      18
LSTR,      24,      23
LSTR,      23,      22
LSTR,      22,      21
LSTR,      21,      20
LSTR,      20,      19
! LLIST,ALL, , ,
LSTR,       6,       7
LSTR,       7,      18
LSTR,      18,      19
LSTR,       5,       8
LSTR,       8,      17
LSTR,      17,      20
LSTR,       4,       9
LSTR,       9,      16
```

```
LSTR,      16,      21
LSTR,       3,      10
LSTR,      10,      15
LSTR,      15,      22
LSTR,       2,      11
LSTR,      11,      14
LSTR,      14,      23
LSTR,       1,      12
LSTR,      12,      13
LSTR,      13,      24
! LLIST,ALL, , ,
FLST,2,4,4
FITEM,2,5
FITEM,2,21
FITEM,2,10
FITEM,2,24
AL,P51X
FLST,2,4,4
FITEM,2,10
FITEM,2,22
FITEM,2,15
FITEM,2,25
AL,P51X
! alist, all
FLST,2,4,4
FITEM,2,15
FITEM,2,23
FITEM,2,20
FITEM,2,26
AL,P51X
FLST,2,4,4
FITEM,2,4
FITEM,2,24
FITEM,2,9
FITEM,2,27
AL,P51X
FLST,2,4,4
FITEM,2,9
FITEM,2,25
FITEM,2,14
FITEM,2,28
AL,P51X
! alist, all
FLST,2,4,4
FITEM,2,14
FITEM,2,26
FITEM,2,19
FITEM,2,29
AL,P51X
FLST,2,4,4
FITEM,2,3
FITEM,2,27
FITEM,2,8
FITEM,2,30
AL,P51X
FLST,2,4,4
FITEM,2,8
```

```
FITEM,2,28
FITEM,2,13
FITEM,2,31
AL,P51X
FLST,2,4,4
FITEM,2,13
FITEM,2,29
FITEM,2,18
FITEM,2,32
AL,P51X
FLST,2,4,4
FITEM,2,2
FITEM,2,30
FITEM,2,7
FITEM,2,33
AL,P51X
FLST,2,4,4
FITEM,2,7
FITEM,2,31
FITEM,2,12
FITEM,2,34
AL,P51X
FLST,2,4,4
FITEM,2,12
FITEM,2,32
FITEM,2,17
FITEM,2,35
AL,P51X
FLST,2,4,4
FITEM,2,1
FITEM,2,33
FITEM,2,6
FITEM,2,36
AL,P51X
FLST,2,4,4
FITEM,2,6
FITEM,2,11
FITEM,2,34
FITEM,2,37
AL,P51X
FLST,2,4,4
FITEM,2,11
FITEM,2,16
FITEM,2,38
FITEM,2,35
AL,P51X
! alist, all
AATT,       1, ,   1,       0
! alist, all

FLST,5,4,4,ORDE,4
FITEM,5,5
FITEM,5,10
FITEM,5,15
FITEM,5,20
CM,_Y,LINE
LSEL, , , ,P51X
```

```
!*
CM,_Y1,LINE
CMSEL,,_Y
LESIZE,_Y1, , ,1,1,
CMDEL,_Y
CMDEL,_Y1
!*
FLST,5,12,4,ORDE,8
FITEM,5,2
FITEM,5,-4
FITEM,5,7
FITEM,5,-9
FITEM,5,12
FITEM,5,-14
FITEM,5,17
FITEM,5,-19
CM,_Y,LINE
LSEL, , , ,P51X
!*
CM,_Y1,LINE
CMSEL,,_Y
LESIZE,_Y1, , ,2,1,
CMDEL,_Y
CMDEL,_Y1
!*
FLST,5,4,4,ORDE,4
FITEM,5,1
FITEM,5,6
FITEM,5,11
FITEM,5,16
CM,_Y,LINE
LSEL, , , ,P51X
!*
CM,_Y1,LINE
CMSEL,,_Y
LESIZE,_Y1, , ,20,20,
CMDEL,_Y
CMDEL,_Y1
!*
FLST,5,12,4,ORDE,12
FITEM,5,22
FITEM,5,-23
FITEM,5,25
FITEM,5,-26
FITEM,5,28
FITEM,5,-29
FITEM,5,31
FITEM,5,-32
FITEM,5,34
FITEM,5,-35
FITEM,5,37
FITEM,5,-38
CM,_Y,LINE
LSEL, , , ,P51X
!*
CM,_Y1,LINE
CMSEL,,_Y
```

```
LESIZE,_Y1, , ,2,1,
CMDEL,_Y
CMDEL,_Y1
!*
FLST,5,6,4,ORDE,6
FITEM,5,21
FITEM,5,24
FITEM,5,27
FITEM,5,30
FITEM,5,33
FITEM,5,36
CM,_Y,LINE
LSEL, , , ,P51X
!*
CM,_Y1,LINE
CMSEL,,_Y
LESIZE,_Y1, , ,4,1,
CMDEL,_Y
CMDEL,_Y1
!*
FLST,5,4,4,ORDE,4
FITEM,5,1
FITEM,5,6
FITEM,5,11
FITEM,5,16
CM,_Y1,LINE
LSEL, , , ,P51X
*GET,_z1,LINE,,COUNT
_z2=0
*DO,_z5,1,_z1
_z2=LSNEXT(_z2)
*GET,_z3,LINE,_z2,ATTR,NDIV
*GET,_z4,LINE,_z2,ATTR,SPAC
*IF,_z3,GT,0,THEN
*IF,_z4,NE,0,THEN
LESIZE,_z2,,,_z3,1/_z4
*ENDIF
*ENDIF
*ENDDO
CMSEL,S,_Y1
CMDELE,_Y1
!*
/UI,MESH,OFF
MSHAPE,0,2D
MSHKEY,1
!*
FLST,5,3,5,ORDE,2
FITEM,5,1
FITEM,5,-3
CM,_Y,AREA
ASEL, , , ,P51X
CM,_Y1,AREA
CHKMSH,'AREA'
CMSEL,S,_Y
!*
AMESH,_Y1
!*
```

```
CMDEL,_Y
CMDEL,_Y1
CMDEL,_Y2
!*
FLST,2,8,2,ORDE,2
FITEM,2,1
FITEM,2,-8
BFE,P51X,HGEN, ,1.00611e11,1.00611e11,1.00611e11,1.00611e11,

FLST,5,12,5,ORDE,2
FITEM,5,4
FITEM,5,-15
CM,_Y,AREA
ASEL, , , ,P51X
CM,_Y1,AREA
CHKMSH,'AREA'
CMSEL,S,_Y
!*
AMESH,_Y1
!*
CMDEL,_Y
CMDEL,_Y1
CMDEL,_Y2
!*
! elist,all,,,0,0

FLST,2,8,4,ORDE,4
FITEM,2,1
FITEM,2,-5
FITEM,2,36
FITEM,2,-38
SFL,P51X,HFLUX,0, ,
FLST,2,5,4,ORDE,2
FITEM,2,16
FITEM,2,-20
SFL,P51X,CONV,200, ,24.54, ,
FLST,2,3,4,ORDE,2
FITEM,2,21
FITEM,2,-23
SFL,P51X,CONV,10000, ,23.667, ,
! SFLLIS, ALL
! BFELIS, ALL

/UI,MESH,OFF
FINISH
/SOLU
!*
ANTYPE,0
! /STAT,SOLU
SOLVE
```

THIS PAGE WAS INTENTIONALLY LEFT BLANK

```
 AFTER YOU HAVE READ, UNDERSTOOD, AND AGREED TO THE PREVIOUS NOTICES,
 PRESS <CR> OR <ENTER> TO CONTINUE


          *****  ANSYS COMMAND LINE ARGUMENTS  *****
  INITIAL JOBNAME              = file
  MEMORY REQUESTED (MB)        = 64
  GRAPHICS DEVICE REQUESTED    = X11
  START-UP FILE MODE           = READ
  GRAPHICAL ENTRY              = YES
  LANGUAGE                     = C
  DATABASE SIZE REQUESTED (MB) = 16

 *** NOTE ***                            CP=     10.940   TIME=
09:45:43
 There are no parameters and no abbreviations defined.

 00022263          VERSION=SOLARIS         RELEASE= 5.4     UP19970828
 CURRENT JOBNAME=file  09:45:43  OCT 29, 2004 CP=     10.954

 /SHOW SET WITH DRIVER NAME= X11     ,  RASTER MODE,  GRAPHIC PLANES =
8

 RUN SETUP PROCEDURE FROM FILE= /ansys54/docu/start.ans

 /INPUT FILE= menust.tmp  LINE=       0

 /INPUT FILE= /ansys54/docu/start.ans  LINE=       0

 ACTIVATING THE GRAPHICAL USER INTERFACE (GUI).  PLEASE WAIT...

 RESUME ANSYS DATA FROM FILE NAME=StStateGlassModel.db

 *** ANSYS GLOBAL STATUS ***

 TITLE =
 NUMBER OF ELEMENT TYPES =      0
       0 ELEMENTS CURRENTLY SELECTED.  MAX ELEMENT NUMBER =        0
       0 NODES CURRENTLY SELECTED.     MAX NODE NUMBER =           0
 ACTIVE COORDINATE SYSTEM              =       0  (CARTESIAN)

 INITIAL JOBNAME = file
 CURRENT JOBNAME = file

 CLEAR ANSYS DATABASE AND RESTART

 ANSYS/Mechanical/Emag 3D

 CURRENT JOBNAME REDEFINED AS StStateGlassModel

 *** NOTE ***                            CP=     33.094   TIME=
09:48:42
 NEW BACKUP FILE NAME= StStateGlassModel.dbb.

 ALL CURRENT ANSYS DATA WRITTEN TO FILE NAME= StStateGlassModel.db
  FOR POSSIBLE RESUME FROM THIS POINT
```

```
 Preferences for GUI filtering have been set to display:
   Thermal

          ***** ANSYS ANALYSIS DEFINITION (PREP7) *****

 ENTER  /SHOW,DEVICE-NAME  TO ENABLE GRAPHIC DISPLAY
 ENTER  FINISH             TO LEAVE PREP7
 PRINTOUT KEY SET TO /GOPR (USE /NOPR TO SUPPRESS)

 ELEMENT TYPE      1 IS PLANE77      2-D 8-NODE THERMAL SOLID
  KEYOPT(1-12)=    0  0  0    0  0  0    0  0  0    0  0  0

 CURRENT NODAL DOF SET IS  TEMP
  TWO-DIMENSIONAL MODEL

 ELEMENT TYPE  1 IS PLANE77      2-D 8-NODE THERMAL SOLID
  KEYOPT(1-12)=    0  0  0    0  0  0    0  0  0    0  0  0

 CURRENT NODAL DOF SET IS  TEMP
  TWO-DIMENSIONAL MODEL

 ELEMENT TYPE  1 IS PLANE77      AXI. 8-NODE THERMAL SOLID
  KEYOPT(1-12)=    0  0  1    0  0  0    0  0  0    0  0  0

 CURRENT NODAL DOF SET IS  TEMP
  AXISYMMETRIC MODEL

 MATERIAL      1     KXX  =   1.040000

 KEYPOINT      1   X,Y,Z=        0.            0.            0.      IN
CSYS=  0

 PLOT KEY POINTS FROM       1 TO       1 BY      1

 KEYPOINT      2   X,Y,Z=        0.      0.980000E-01        0.      IN
CSYS=  0

 PLOT KEY POINTS FROM       1 TO       2 BY      1

 KEYPOINT      3   X,Y,Z=        0.      0.990000E-01        0.      IN
CSYS=  0

 PLOT KEY POINTS FROM       1 TO       3 BY      1

 KEYPOINT      4   X,Y,Z=        0.      0.100000            0.      IN
CSYS=  0

 PLOT KEY POINTS FROM       1 TO       4 BY      1

 KEYPOINT      5   X,Y,Z=        0.      0.100500            0.      IN
CSYS=  0

 PLOT KEY POINTS FROM       1 TO       5 BY      1

 KEYPOINT      6   X,Y,Z=        0.      0.100501            0.      IN
CSYS=  0
```

```
 PLOT KEY POINTS FROM       1 TO       6 BY      1

 KEYPOINT      7   X,Y,Z=  0.470000E-02  0.100501            0.      IN
CSYS=  0

 PLOT KEY POINTS FROM       1 TO       7 BY      1

 KEYPOINT      8   X,Y,Z=  0.470000E-02  0.100500            0.      IN
CSYS=  0

 KEYPOINT      9   X,Y,Z=  0.470000E-02  0.100000            0.      IN
CSYS=  0

 KEYPOINT     10   X,Y,Z=  0.470000E-02  0.990000E-01        0.      IN
CSYS=  0

 KEYPOINT     11   X,Y,Z=  0.470000E-02  0.980000E-01        0.      IN
CSYS=  0

 KEYPOINT     12   X,Y,Z=  0.470000E-02        0.            0.      IN
CSYS=  0

 KEYPOINT     13   X,Y,Z=  0.700000E-02        0.            0.      IN
CSYS=  0

 PLOT KEY POINTS FROM       1 TO      13 BY      1

 KEYPOINT     14   X,Y,Z=  0.700000E-02  0.980000E-01        0.      IN
CSYS=  0

 KEYPOINT     15   X,Y,Z=  0.700000E-02  0.990000E-01        0.      IN
CSYS=  0

 KEYPOINT     16   X,Y,Z=  0.700000E-02  0.100000            0.      IN
CSYS=  0

 KEYPOINT     17   X,Y,Z=  0.700000E-02  0.100500            0.      IN
CSYS=  0

 KEYPOINT     18   X,Y,Z=  0.700000E-02  0.100501            0.      IN
CSYS=  0

 KEYPOINT     19   X,Y,Z=  0.800000E-02  0.100501            0.      IN
CSYS=  0

 PLOT KEY POINTS FROM       1 TO      19 BY      1

 KEYPOINT     20   X,Y,Z=  0.800000E-02  0.100500            0.      IN
CSYS=  0

 KEYPOINT     21   X,Y,Z=  0.800000E-02  0.100000            0.      IN
CSYS=  0

 KEYPOINT     22   X,Y,Z=  0.800000E-02  0.990000E-01        0.      IN
CSYS=  0
```

```
 KEYPOINT     23   X,Y,Z=  0.800000E-02  0.980000E-01        0.       IN
CSYS=  0

 KEYPOINT     24   X,Y,Z=  0.800000E-02        0.            0.       IN
CSYS=  0

 LINE CONNECTS KEYPOINTS      1     2
  LINE NO.=     1  KP1=      1  TAN1=    0.0000  -1.0000   0.0000
                   KP2=      2  TAN2=    0.0000   1.0000   0.0000

 LINE CONNECTS KEYPOINTS      2     3
  LINE NO.=     2  KP1=      2  TAN1=    0.0000  -1.0000   0.0000
                   KP2=      3  TAN2=    0.0000   1.0000   0.0000

 LINE CONNECTS KEYPOINTS      3     4
  LINE NO.=     3  KP1=      3  TAN1=    0.0000  -1.0000   0.0000
                   KP2=      4  TAN2=    0.0000   1.0000   0.0000

 LINE CONNECTS KEYPOINTS      4     5
  LINE NO.=     4  KP1=      4  TAN1=    0.0000  -1.0000   0.0000
                   KP2=      5  TAN2=    0.0000   1.0000   0.0000

 LINE CONNECTS KEYPOINTS      5     6
  LINE NO.=     5  KP1=      5  TAN1=    0.0000  -1.0000   0.0000
                   KP2=      6  TAN2=    0.0000   1.0000   0.0000

 LINE CONNECTS KEYPOINTS     12    11
  LINE NO.=     6  KP1=     12  TAN1=    0.0000  -1.0000   0.0000
                   KP2=     11  TAN2=    0.0000   1.0000   0.0000

 LINE CONNECTS KEYPOINTS     11    10
  LINE NO.=     7  KP1=     11  TAN1=    0.0000  -1.0000   0.0000
                   KP2=     10  TAN2=    0.0000   1.0000   0.0000

 LINE CONNECTS KEYPOINTS     10     9
  LINE NO.=     8  KP1=     10  TAN1=    0.0000  -1.0000   0.0000
                   KP2=      9  TAN2=    0.0000   1.0000   0.0000

 LINE CONNECTS KEYPOINTS      9     8
  LINE NO.=     9  KP1=      9  TAN1=    0.0000  -1.0000   0.0000
                   KP2=      8  TAN2=    0.0000   1.0000   0.0000

 LINE CONNECTS KEYPOINTS      8     7
  LINE NO.=    10  KP1=      8  TAN1=    0.0000  -1.0000   0.0000
                   KP2=      7  TAN2=    0.0000   1.0000   0.0000

 LINE CONNECTS KEYPOINTS     13    14
  LINE NO.=    11  KP1=     13  TAN1=    0.0000  -1.0000   0.0000
                   KP2=     14  TAN2=    0.0000   1.0000   0.0000

 LINE CONNECTS KEYPOINTS     14    15
  LINE NO.=    12  KP1=     14  TAN1=    0.0000  -1.0000   0.0000
                   KP2=     15  TAN2=    0.0000   1.0000   0.0000

 LINE CONNECTS KEYPOINTS     15    16
  LINE NO.=    13  KP1=     15  TAN1=    0.0000  -1.0000   0.0000
                   KP2=     16  TAN2=    0.0000   1.0000   0.0000
```

```
LINE CONNECTS KEYPOINTS      16     17
 LINE NO.=    14  KP1=      16  TAN1=    0.0000  -1.0000   0.0000
                  KP2=      17  TAN2=    0.0000   1.0000   0.0000

LINE CONNECTS KEYPOINTS      17     18
 LINE NO.=    15  KP1=      17  TAN1=    0.0000  -1.0000   0.0000
                  KP2=      18  TAN2=    0.0000   1.0000   0.0000

LINE CONNECTS KEYPOINTS      24     23
 LINE NO.=    16  KP1=      24  TAN1=    0.0000  -1.0000   0.0000
                  KP2=      23  TAN2=    0.0000   1.0000   0.0000

LINE CONNECTS KEYPOINTS      23     22
 LINE NO.=    17  KP1=      23  TAN1=    0.0000  -1.0000   0.0000
                  KP2=      22  TAN2=    0.0000   1.0000   0.0000

LINE CONNECTS KEYPOINTS      22     21
 LINE NO.=    18  KP1=      22  TAN1=    0.0000  -1.0000   0.0000
                  KP2=      21  TAN2=    0.0000   1.0000   0.0000

LINE CONNECTS KEYPOINTS      21     20
 LINE NO.=    19  KP1=      21  TAN1=    0.0000  -1.0000   0.0000
                  KP2=      20  TAN2=    0.0000   1.0000   0.0000

LINE CONNECTS KEYPOINTS      20     19
 LINE NO.=    20  KP1=      20  TAN1=    0.0000  -1.0000   0.0000
                  KP2=      19  TAN2=    0.0000   1.0000   0.0000

LINE CONNECTS KEYPOINTS       6      7
 LINE NO.=    21  KP1=       6  TAN1=   -1.0000   0.0000   0.0000
                  KP2=       7  TAN2=    1.0000   0.0000   0.0000

LINE CONNECTS KEYPOINTS       7     18
 LINE NO.=    22  KP1=       7  TAN1=   -1.0000   0.0000   0.0000
                  KP2=      18  TAN2=    1.0000   0.0000   0.0000

LINE CONNECTS KEYPOINTS      18     19
 LINE NO.=    23  KP1=      18  TAN1=   -1.0000   0.0000   0.0000
                  KP2=      19  TAN2=    1.0000   0.0000   0.0000

LINE CONNECTS KEYPOINTS       5      8
 LINE NO.=    24  KP1=       5  TAN1=   -1.0000   0.0000   0.0000
                  KP2=       8  TAN2=    1.0000   0.0000   0.0000

LINE CONNECTS KEYPOINTS       8     17
 LINE NO.=    25  KP1=       8  TAN1=   -1.0000   0.0000   0.0000
                  KP2=      17  TAN2=    1.0000   0.0000   0.0000

LINE CONNECTS KEYPOINTS      17     20
 LINE NO.=    26  KP1=      17  TAN1=   -1.0000   0.0000   0.0000
                  KP2=      20  TAN2=    1.0000   0.0000   0.0000

LINE CONNECTS KEYPOINTS       4      9
 LINE NO.=    27  KP1=       4  TAN1=   -1.0000   0.0000   0.0000
                  KP2=       9  TAN2=    1.0000   0.0000   0.0000
```

```
LINE CONNECTS KEYPOINTS      9    16
 LINE NO.=    28  KP1=      9  TAN1=   -1.0000   0.0000   0.0000
                  KP2=     16  TAN2=    1.0000   0.0000   0.0000

LINE CONNECTS KEYPOINTS     16    21
 LINE NO.=    29  KP1=     16  TAN1=   -1.0000   0.0000   0.0000
                  KP2=     21  TAN2=    1.0000   0.0000   0.0000

LINE CONNECTS KEYPOINTS      3    10
 LINE NO.=    30  KP1=      3  TAN1=   -1.0000   0.0000   0.0000
                  KP2=     10  TAN2=    1.0000   0.0000   0.0000

LINE CONNECTS KEYPOINTS     10    15
 LINE NO.=    31  KP1=     10  TAN1=   -1.0000   0.0000   0.0000
                  KP2=     15  TAN2=    1.0000   0.0000   0.0000

LINE CONNECTS KEYPOINTS     15    22
 LINE NO.=    32  KP1=     15  TAN1=   -1.0000   0.0000   0.0000
                  KP2=     22  TAN2=    1.0000   0.0000   0.0000

LINE CONNECTS KEYPOINTS      2    11
 LINE NO.=    33  KP1=      2  TAN1=   -1.0000   0.0000   0.0000
                  KP2=     11  TAN2=    1.0000   0.0000   0.0000

LINE CONNECTS KEYPOINTS     11    14
 LINE NO.=    34  KP1=     11  TAN1=   -1.0000   0.0000   0.0000
                  KP2=     14  TAN2=    1.0000   0.0000   0.0000

LINE CONNECTS KEYPOINTS     14    23
 LINE NO.=    35  KP1=     14  TAN1=   -1.0000   0.0000   0.0000
                  KP2=     23  TAN2=    1.0000   0.0000   0.0000

LINE CONNECTS KEYPOINTS      1    12
 LINE NO.=    36  KP1=      1  TAN1=   -1.0000   0.0000   0.0000
                  KP2=     12  TAN2=    1.0000   0.0000   0.0000

LINE CONNECTS KEYPOINTS     12    13
 LINE NO.=    37  KP1=     12  TAN1=   -1.0000   0.0000   0.0000
                  KP2=     13  TAN2=    1.0000   0.0000   0.0000

LINE CONNECTS KEYPOINTS     13    24
 LINE NO.=    38  KP1=     13  TAN1=   -1.0000   0.0000   0.0000
                  KP2=     24  TAN2=    1.0000   0.0000   0.0000

DEFINE AREA BY LIST OF LINES
     (TRAVERSED IN SAME DIRECTION AS LINE     5)

    AREA NUMBER =      1

DEFINE AREA BY LIST OF LINES
     (TRAVERSED IN SAME DIRECTION AS LINE    10)

    AREA NUMBER =      2

DEFINE AREA BY LIST OF LINES
     (TRAVERSED IN SAME DIRECTION AS LINE    15)
```

```
    AREA NUMBER =      3

DEFINE AREA BY LIST OF LINES
     (TRAVERSED IN SAME DIRECTION AS LINE     4)

    AREA NUMBER =      4

DEFINE AREA BY LIST OF LINES
     (TRAVERSED IN SAME DIRECTION AS LINE     9)

    AREA NUMBER =      5

DEFINE AREA BY LIST OF LINES
     (TRAVERSED IN SAME DIRECTION AS LINE    14)

    AREA NUMBER =      6

DEFINE AREA BY LIST OF LINES
     (TRAVERSED IN SAME DIRECTION AS LINE     3)

    AREA NUMBER =      7

DEFINE AREA BY LIST OF LINES
     (TRAVERSED IN SAME DIRECTION AS LINE     8)

    AREA NUMBER =      8

DEFINE AREA BY LIST OF LINES
     (TRAVERSED IN SAME DIRECTION AS LINE    13)

    AREA NUMBER =      9

DEFINE AREA BY LIST OF LINES
     (TRAVERSED IN SAME DIRECTION AS LINE     2)

    AREA NUMBER =     10

DEFINE AREA BY LIST OF LINES
     (TRAVERSED IN SAME DIRECTION AS LINE     7)

    AREA NUMBER =     11

DEFINE AREA BY LIST OF LINES
     (TRAVERSED IN SAME DIRECTION AS LINE    12)

    AREA NUMBER =     12

DEFINE AREA BY LIST OF LINES
     (TRAVERSED IN SAME DIRECTION AS LINE     1)

    AREA NUMBER =     13

DEFINE AREA BY LIST OF LINES
     (TRAVERSED IN SAME DIRECTION AS LINE     6)

    AREA NUMBER =     14
```

```
 DEFINE AREA BY LIST OF LINES
      (TRAVERSED IN SAME DIRECTION AS LINE    11)

     AREA NUMBER =     15

 SET ATTRIBUTES FOR ALL SELECTED AREAS
      MAT =    1   REAL =       0   TYPE =    1   ESYS =    0
 ATTRIBUTES SET FOR     15 AREAS (OUT OF     15 SELECTED)

 SET DIVISIONS ON ALL PICKED UNMESHED LINES
      TO  NDIV =    1,  SPACING RATIO =   1.000

 SET DIVISIONS ON ALL PICKED UNMESHED LINES
      TO  NDIV =    2,  SPACING RATIO =   1.000

 SET DIVISIONS ON ALL PICKED UNMESHED LINES
      TO  NDIV =   10,  SPACING RATIO =  30.000

 SET DIVISIONS ON ALL PICKED UNMESHED LINES
      TO  NDIV =    2,  SPACING RATIO =   1.000

 SET DIVISIONS ON ALL PICKED UNMESHED LINES
      TO  NDIV =    4,  SPACING RATIO =   1.000
 PRODUCE ALL QUADRILATERAL ELEMENTS IN 2D.
 USE THE MAPPED MESHER.

 GENERATE NODES AND ELEMENTS   IN  ALL  PICKED   AREAS

 ** Meshing of area 1 in progress **
    ** AREA     1 MESHED WITH     4 QUADRILATERALS,      0 TRIANGLES **

 *** WARNING ***                         CP=     93.810   TIME=
10:03:17
 Quadrilateral element 1 has an aspect ratio of 1175, which exceeds the
  warning limit of 20.

 *** WARNING ***                         CP=     93.867   TIME=
10:03:17
 Quadrilateral element 2 has an aspect ratio of 1175, which exceeds the
  warning limit of 20.

 *** WARNING ***                         CP=     93.888   TIME=
10:03:17
 Quadrilateral element 3 has an aspect ratio of 1175, which exceeds the
  warning limit of 20.

 *** WARNING ***                         CP=     93.923   TIME=
10:03:17
 Quadrilateral element 4 has an aspect ratio of 1175, which exceeds the
  warning limit of 20.
 ** Meshing of area 1 completed ** 4 elements.

 ** Meshing of area 2 in progress **
    ** AREA     2 MESHED WITH     2 QUADRILATERALS,      0 TRIANGLES **

 *** WARNING ***                         CP=     94.164   TIME=
10:03:17
```

```
 Quadrilateral element 5 has an aspect ratio of 1150, which exceeds the
  warning limit of 20.

 *** WARNING ***                         CP=     94.214   TIME=
10:03:17
 Quadrilateral element 6 has an aspect ratio of 1150, which exceeds the
  warning limit of 20.
 ** Meshing of area 2 completed ** 2 elements.

 ** Meshing of area 3 in progress **
    ** AREA     3 MESHED WITH     2 QUADRILATERALS,      0 TRIANGLES **

 *** WARNING ***                         CP=     94.356   TIME=
10:03:18
 Quadrilateral element 7 has an aspect ratio of 500, which exceeds the
  warning limit of 20.

 *** WARNING ***                         CP=     94.400   TIME=
10:03:18
 Quadrilateral element 8 has an aspect ratio of 500, which exceeds the
  warning limit of 20.
 ** Meshing of area 3 completed ** 2 elements.

 NUMBER OF AREAS MESHED     =      3
 MAXIMUM NODE NUMBER        =     43
 MAXIMUM ELEMENT NUMBER     =      8

 PRODUCE ELEMENT PLOT IN DSYS =   0

 SPECIFIED BODY FORCE HGEN FOR ALL PICKED ELEMENTS AT STARTING LOCATION
1
   1.006110000E+11 1.006110000E+11 1.006110000E+11 1.006110000E+11

 *** NOTE ***                            CP=    100.908   TIME=
10:05:11
 DELETED BACKUP FILE NAME= StStateGlassModel.dbb.

 *** NOTE ***                            CP=    100.915   TIME=
10:05:11
 NEW BACKUP FILE NAME= StStateGlassModel.dbb.

 ALL CURRENT ANSYS DATA WRITTEN TO FILE NAME= StStateGlassModel.db
  FOR POSSIBLE RESUME FROM THIS POINT

 GENERATE NODES AND ELEMENTS   IN  ALL  PICKED   AREAS

 ** Meshing of area 4 in progress **
    ** AREA     4 MESHED WITH     8 QUADRILATERALS,      0 TRIANGLES **
 ** Meshing of area 4 completed ** 8 elements.

 ** Meshing of area 5 in progress **
    ** AREA     5 MESHED WITH     4 QUADRILATERALS,      0 TRIANGLES **
 ** Meshing of area 5 completed ** 4 elements.

 ** Meshing of area 6 in progress **
    ** AREA     6 MESHED WITH     4 QUADRILATERALS,      0 TRIANGLES **
 ** Meshing of area 6 completed ** 4 elements.
```

```
 ** Meshing of area 7 in progress **
    ** AREA     7 MESHED WITH     8 QUADRILATERALS,      0 TRIANGLES **
 ** Meshing of area 7 completed ** 8 elements.

 ** Meshing of area 8 in progress **
    ** AREA     8 MESHED WITH     4 QUADRILATERALS,      0 TRIANGLES **
 ** Meshing of area 8 completed ** 4 elements.

 ** Meshing of area 9 in progress **
    ** AREA     9 MESHED WITH     4 QUADRILATERALS,      0 TRIANGLES **
 ** Meshing of area 9 completed ** 4 elements.

 ** Meshing of area 10 in progress **
    ** AREA    10 MESHED WITH     8 QUADRILATERALS,      0 TRIANGLES **
 ** Meshing of area 10 completed ** 8 elements.

 ** Meshing of area 11 in progress **
    ** AREA    11 MESHED WITH     4 QUADRILATERALS,      0 TRIANGLES **
 ** Meshing of area 11 completed ** 4 elements.

 ** Meshing of area 12 in progress **
    ** AREA    12 MESHED WITH     4 QUADRILATERALS,      0 TRIANGLES **
 ** Meshing of area 12 completed ** 4 elements.

 ** Meshing of area 13 in progress **
    ** AREA    13 MESHED WITH    80 QUADRILATERALS,      0 TRIANGLES **
 ** Meshing of area 13 completed ** 80 elements.

 ** Meshing of area 14 in progress **
    ** AREA    14 MESHED WITH    40 QUADRILATERALS,      0 TRIANGLES **
 ** Meshing of area 14 completed ** 40 elements.

 ** Meshing of area 15 in progress **
    ** AREA    15 MESHED WITH    40 QUADRILATERALS,      0 TRIANGLES **

 *** WARNING ***                         CP=    105.484   TIME=
10:05:32
 Quadrilateral element 177 has an aspect ratio of 29.87, which exceeds
  the warning limit of 20.

 *** WARNING ***                         CP=    105.531   TIME=
10:05:32
 Quadrilateral element 178 has an aspect ratio of 29.87, which exceeds
  the warning limit of 20.

 *** WARNING ***                         CP=    105.555   TIME=
10:05:32
 Quadrilateral element 179 has an aspect ratio of 25.51, which exceeds
  the warning limit of 20.

 *** WARNING ***                         CP=    105.590   TIME=
10:05:33
 Quadrilateral element 180 has an aspect ratio of 25.51, which exceeds
  the warning limit of 20.
```

```
 *** WARNING ***                         CP=    105.630   TIME=
10:05:33
 Quadrilateral element 181 has an aspect ratio of 21.79, which exceeds
  the warning limit of 20.

***********************************************************************
*
 Error messages discontinued after 5 messages were displayed.
  More may exist.  See ( file.err ) for suppressed messages.
***********************************************************************
*
 ** Meshing of area 15 completed ** 40 elements.

 NUMBER OF AREAS MESHED     =     12
 MAXIMUM NODE NUMBER        =    719
 MAXIMUM ELEMENT NUMBER     =    216

 PRODUCE ELEMENT PLOT IN DSYS =   0

 SURFACE LOAD ON ALL PICKED LINES
     LOAD LABEL = HFLU
     VALI,  VALJ  =              0.                   0.

 SURFACE LOAD ON ALL PICKED LINES
     LOAD LABEL = CONV
     VALI,  VALJ  =          200.00              200.00
     VAL2I, VAL2J =          24.540              24.540

 CONV LOAD SURFACE DISPLAY KEY =  1

 SURFACE LOAD ON ALL PICKED LINES
     LOAD LABEL = CONV
     VALI,  VALJ  =          10000.              10000.
     VAL2I, VAL2J =          23.667              23.667

 *** NOTE ***                            CP=    122.061   TIME=
10:09:06
 DELETED BACKUP FILE NAME= StStateGlassModel.dbb.

 *** NOTE ***                            CP=    122.068   TIME=
10:09:06
 NEW BACKUP FILE NAME= StStateGlassModel.dbb.

 ALL CURRENT ANSYS DATA WRITTEN TO FILE NAME= StStateGlassModel.db
  FOR POSSIBLE RESUME FROM THIS POINT

 ***** ROUTINE COMPLETED *****  CP =       123.575

 *****  ANSYS SOLUTION ROUTINE  *****

 PERFORM A STATIC ANALYSIS
  THIS WILL BE A NEW ANALYSIS

 *****  ANSYS SOLVE    COMMAND  *****

 TRANSFER SOLID MODEL BOUNDARY CONDITIONS TO FINITE ELEMENT MODEL
      SURFACE LOADS  TRANSFERRED FROM LINES          =     70
```

```
 *** NOTE ***                            CP=    126.899   TIME=
10:09:31
 There is no title defined for this analysis.

 *** WARNING ***                         CP=    127.052   TIME=
10:09:32
 Previous testing revealed that 14 of the 216 selected elements violate
  shape warning limits.  To review warning messages, please see the
  output or error file, or issue the CHECK command.

 *** NOTE ***                            CP=    127.090   TIME=
10:09:32
 The model data was checked and warning messages were found.
  Please review output or errors file ( file.err ) for these warning
  messages.

                       S O L U T I O N   O P T I O N S

   PROBLEM DIMENSIONALITY. . . . . . . . . . . . .AXISYMMETRIC
   DEGREES OF FREEDOM. . . . . . TEMP
   ANALYSIS TYPE . . . . . . . . . . . . . . . . .STATIC (STEADY-STATE)

 *** NOTE ***                            CP=    127.325   TIME=
10:09:33
 Axisymmetric elements present.  Nodal loads input with the F commands
  and the reaction forces are on a full circle basis.  This differs
from
  pre-ANSYS 5.0 interpretation.

 *** NOTE ***                            CP=    127.332   TIME=
10:09:33
 Present time 0 is less than or equal to the previous time.
  Time will default to 1.

 *** WARNING ***                         CP=    127.353   TIME=
10:09:34
 Element 1 face 4 convection is on or near a zero radius face.

 *** WARNING ***                         CP=    127.401   TIME=
10:09:34
 Element 9 face 4 convection is on or near a zero radius face.

 *** WARNING ***                         CP=    127.474   TIME=
10:09:39
 Element 13 face 4 convection is on or near a zero radius face.

 *** WARNING ***                         CP=    127.500   TIME=
10:09:39
 Element 25 face 4 convection is on or near a zero radius face.

************************************************************************
*
 Error messages discontinued after 5 messages were displayed.
  More may exist.  See ( file.err ) for suppressed messages.
************************************************************************
*
```

```
 *** NOTE ***                            CP=    127.748   TIME=
10:09:39
 The step data was checked and warning messages were found.
  Please review output or errors file ( file.err ) for these warning
  messages.

 *** NOTE ***                            CP=    127.754   TIME=
10:09:39
 Results printout suppressed for interactive execute.

                      L O A D   S T E P   O P T I O N S

   LOAD STEP NUMBER. . . . . . . . . . . . . . . .     1
   TIME AT END OF THE LOAD STEP. . . . . . . . . .  1.0000
   NUMBER OF SUBSTEPS. . . . . . . . . . . . . . .     1
   STEP CHANGE BOUNDARY CONDITIONS . . . . . . . .    NO
   AXISYMMETRIC HARMONIC LOADING PARAMETERS
      MODE . . . . . . . . . . . . . . . . . . . .     0
      ISYM . . . . . . . . . . . . . . . . . . . .     1
   PRINT OUTPUT CONTROLS . . . . . . . . . . . . .NO PRINTOUT
   DATABASE OUTPUT CONTROLS. . . . . . . . . . . .ALL DATA WRITTEN
                                                  FOR THE LAST SUBSTEP

 Range of element maximum matrix coefficients in global coordinates
 Maximum= 89.6753157 at element 6.
 Minimum= 1.100479334E-02 at element 113.

   *** ELEMENT MATRIX FORMULATION TIMES
  TYPE  NUMBER   ENAME      TOTAL CP  AVE CP

     1     216  PLANE77       0.938    0.004
 Time at end of element matrix formulation CP= 129.610037.

 Estimated number of active DOF= 719.
 Maximum wavefront= 54.

 Time at end of matrix triangularization CP= 130.78724.
 Equation solver maximum pivot= 46.3889868 at node 31 TEMP.
 Equation solver minimum pivot= 7.0177546E-04 at node 3 TEMP.

   *** ELEMENT RESULT CALCULATION TIMES
  TYPE  NUMBER   ENAME      TOTAL CP  AVE CP

     1     216  PLANE77       0.784    0.004

   *** NODAL LOAD CALCULATION TIMES
  TYPE  NUMBER   ENAME      TOTAL CP  AVE CP

     1     216  PLANE77       0.183    0.001
 *** LOAD STEP     1   SUBSTEP     1  COMPLETED.    CUM ITER =      1
 *** TIME =   1.00000         TIME INC =   1.00000      NEW TRIANG
MATRIX

   *** PROBLEM STATISTICS
  ACTUAL NO. OF ACTIVE DEGREES OF FREEDOM =    719
  R.M.S. WAVEFRONT SIZE =    36.8
```

```
 *** ANSYS BINARY FILE STATISTICS
  BUFFER SIZE USED= 16384
        0.188 MB WRITTEN ON ELEMENT MATRIX FILE: StStateGlassModel.emat
        0.062 MB WRITTEN ON ELEMENT SAVED DATA FILE:
StStateGlassModel.esav
        0.250 MB WRITTEN ON TRIANGULARIZED MATRIX FILE:
StStateGlassModel.tri
        0.250 MB WRITTEN ON RESULTS FILE: StStateGlassModel.rth

 *** NOTE ***                            CP=    133.681   TIME=
10:10:03
 DELETED BACKUP FILE NAME= StStateGlassModel.dbb.

 *** NOTE ***                            CP=    133.687   TIME=
10:10:04
 NEW BACKUP FILE NAME= StStateGlassModel.dbb.

 ALL CURRENT ANSYS DATA WRITTEN TO FILE NAME= StStateGlassModel.db
  FOR POSSIBLE RESUME FROM THIS POINT

 COPY INPUT COMMANDS FROM DATABASE TO FILE StStKlog
  FILTER OPTION= COMMENT
```

References

Baysinger, K., Yerkes, K., Michalak, T., Harris, R., McQuillen, J., "Design of a Microgravity Spray Cooling Experiment," *42nd AIAA Aerospace Sciences Conference and Exhibit*, 2004.

Carslaw, H., Jaeger J., *Conduction of Heat In Solids,* 2nd ed., Oxford University Press, London, 1959. Appendix III.

Choi, K., Yao, S., "Mechanism of Film Boiling Heat Transfer of Normally Impacting Spray," *International Journal of Heat and Mass Transfer*, Vol. 30, No. 2, 1987, pp. 311-318.

Delil, A., "Microgravity two-phase flow and heat transfer," *Physics of Fluids in Microgravity* (Ed. Monti, R.), pp. 263-292, Taylor & Francis, London, 2001.

Faghri, A., *Heat Pipe Science and Technology*, Taylor & Francis, Washington, DC, 1995, Chapter 1.

Gu, J., Masahiro, K., Futamata, R., "Effects of Gravity on the Performance of Pulsating Heat Pipes," *Journal of Thermophysics and Heat Transfer*, Vol. 18, No. 3, July-September, 2004, pp. 370-378.

Incropera, F., DeWitt, D., *Fundamentals of Heat and Mass Transfer*, 5th ed., John Wiley & Sons, Inc., Hoboken, New Jersey, 2001. Table A.3.

Kato, M., Abe, Y., Mori, Y. H., Nagashima, A., "Spray Cooling Characteristics Under Reduced Gravity," *Journal of Thermophysics*, Vol. 9., No. 2, Technical Notes, 1994, pp. 378-381.

Kaya, T. and Ku, J. "Thermal Operational Characteristics of a Small-Loop Heat Pipe," *Journal of Thermophysics and Heat Transfer.*, Vol.17, No. 4, pp. 464-470, October-December, 2003.

Kim, J. "Review of Reduced Gravity Boiling Heat Transfer: US Research," *J. Jpn. Soc. Microgravity Appl.*, Vol. 20, No. 4, 2003, pp. 264-271.

Kim, J., Benton, J., Wisniewski, D., "Pool boiling heat transfer on small heaters: effect of gravity and subcooling," *International Journal of Heat and Mass Transfer* 45, 2002, pp. 3919-3932.

Lin, L., Ponnappan, R., "Heat Transfer Characteristics of Spray Cooling in a Closed Loop," *International Journal of Heat and Mass Transfer 46,* pp. 3737-3746, 2003.

Lin, L., Ponnappan, R., Yerkes, K., Hager, B., "Large Area Spray Cooling," *42nd AIAA Aerospace Sciences Conference and Exhibit,* 2004.

Mudawar, I., "Assessment of High-Heat-Flux Thermal Management Schemes," *ITHERM2000: International Conference on Thermal Mechanics and Thermomechanical Phenomena in Electronic Systems* (keynote address), 2000.

Ozisik, M., *Heat Conduction*, 2nd ed., Wiley, New York, 1993, Chapters 2-3 and Appendix IV.

Rohsenow, W., Hartnett, J., Ganic, E., *Handbook of Heat Transfer Fundamentals,* McGraw-Hill, New York, 1985, Chapter 1.

Selby, S., *Standard Mathematical Tables*, 21st ed., C.R.C. Press, Cleveland, Ohio, 44128, 1973. p. 454, eq. 533.

Straub, J. "Pool boiling and bubble dynamics in microgravity," *Physics of Fluids in Microgravity* (Ed. Monti, R.), pp. 322-370, Taylor & Francis, London, 2001.

Yoshida, K., Abe, Y., Oka, T., Mori, Y., Nagashima, A., "Spray Cooling Under Reduced Gravity Condition," *ASME Journal of Heat Transfer*, Vol.123, pp. 309-318, 2001.